Master Thesis

Modeling, Simulation and Optimization of a Microcoil for MRI-Cell Imaging

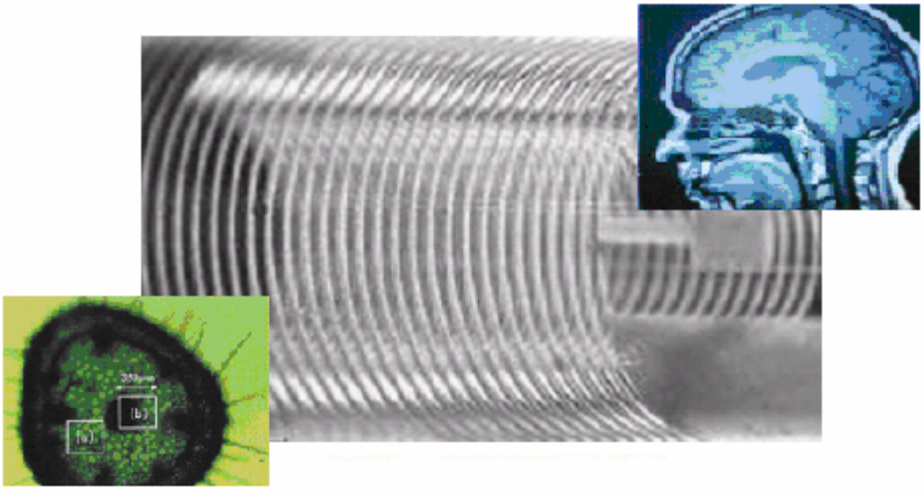

Behrooz Fateh

Master thesis submitted in partial fulfillment of the requirements for the Master degree in "Computational Engineering", University of Rostock, Germany

Institute for Microsystem Technology IMTEK,
Laboratory for Simulation,
Albert-Ludwigs-University of Freiburg, Germany

Author:
Behrooz Fateh (**Matr.-Nr.: 4299288**)

Supervisors:
Prof. Dr. Lienhard Pagel
Faculty of Electrical Engineering, University of Rostock

Prof. Dr. Jan G. Korvink
Laboratory for Simulation, IMTEK, University of Freiburg

November 2006

Frontpage A micro-solenoidal coil and two images taken by MRI

Dedicated to:

My beloved wife, Azin, and my cute son, Shayan, who have brought happiness to my life

And my Father for his patience

Table of Contents

Abstract

Nuclear Magnetic Resonance (NMR) and Magnetic Resonance Imaging (MRI) are most important tools in the fields of chemistry and biology. MRI enables non-invasive, three-dimensional imaging of soft tissues in biological specimens ranging from mice to human being. There is growing interest in performing high-resolution MRI studies at the scale of biological cells.

By miniaturizing the MRI detection coil, one achieves increased sensitivity for analysis of micro-sized samples. A micro-MR image requires a highly homogenous magnetic field within the region where the sample is. An inhomogenous magnetic field leads to image artifacts due to the localized variations in spin precession frequency.

In order to study field uniformity within a solenoidal microcoil, which is used for micro-MR cell imaging, we build a model and simulation using ANSYS® 8.1 and then simulate the magnetic filed within the coil turns. For this purpose, 2-dimensional axis-symmetric model has been created and the resulting magnetic filed properties which are returned from harmonic solution of low frequency electromagnetic analysis has been used as an objective function for a numerical optimization process.

The aim of the optimization is to optimize the microcoil geometry in order to achieve a homogenous magnetic field which is necessary for high resolution imaging in MRI. The DOT optimization software coupled to ANSYS allows us to implement an iterative method and increase the field uniformity within the coil by variation of the design parameters up to 50%.

Furthermore, predictive design and optimization of a microcoil system requires the ability to compact behavioral model for accurate and fast simulation. In this project, the use of model order reduction of such a model for harmonic analysis is demonstrated by means of *more4ansys* tool. The *mor4ansys* has been developed at the simulation group, University of Freiburg. The result shows good simulation accuracy and a considerable speed up the computational time.

Keywords: Nuclear Magnetic Resonance, Magnetic Resonance Imaging, field uniformity, solenoidal microcoil, micro-MR cell imaging, ANSYS, low frequency electromagnetic analysis, numerical optimization, DOT optimization software, *mor4ansys*, model order reduction, simulation

Zusammenfassung

Magnetische Kernresonanz (Nuclear magnetic Resonance: NMR) und Magnetresonanz-tomographie (Magnetic Resonnace Imaging: MRI) sind wichtige Werkzeuge in der Chemie und Biologie. MRI ermöglicht die nicht-invasive, dreidimensionale Abbildung weicher Gewebe im Inneren des Körpers, sei es der einer Maus oder eines Menschen. Ein zunehmendes Interesse besteht an der Durchführung hochauflösenden MRI-Studien an Objekten von der Größe biologischer Zellen.

Durch die Miniaturisierung der MRI-Detektionsspule kann eine erhöhte Empfindlichkeit für Analysen an mikroskopisch kleinen Proben erreicht werden. Ein Mikro-MR-Bild erfordert ein höchst homogenes Feld in der Region, in der sich die Probe befindet. Ein inhomogenes Feld führt zu Bildstörungen wegen der lokalen Variationen der Spin-Präzessionsfrequenz.

Um die Homogenität innerhalb einer Solenoidem Mikrospule zu erforschen, entwarfen wir ein Model mit Hilfe von ANSYS® Version 8.1 und simulierten das magnetische Feld innerhalb der Spulenwindungen. Dafür wurde ein 2-dimensionales, axisymmetrisches Modell erstellt. Die resultierenden Eigenschaften des magnetischen Feldes, die wir aus der harmonischen Lösung einer Niederfrequenzanalyse erhielten, wurden als Zielfunktion eines numerischen Optimierungsprozesses verwendet.

Das Ziel der Optimierung war, die Geometrie der Mikrospule auf ein möglichst homogenes magnetisches Feld abzustimmen. Die an ANSYS gekoppelte DOT-Optimierungssoftware ermöglichte uns, eine iterative Methode zu verwenden und damit die Homogenität des Feldes in der Spule durch Veränderung der Designparameter um bis zu 50% zu erhöhen.

Des weiteren erfordern die Prognose des Verhaltens das Design und die Optimierung des Mikrospulensystems ein kompaktes Verhaltensmodell für eine genaue und schnelle Simulation. In diesem Projekt wurde das Verfahren der Modellordnungsreduktion für die harmonische Analyse angewandt. Dabei wurde das Tool mor4ansys verwendet, das am Lehrstuhl für Simulation, Institut für Mikrosystemtechnik der Universität von Freiburg, entwickelt wurde. Das Ergebnis zeigt eine gute Simulations-Genauigkeit und eine beträchtliche Steigerung der Berechnungsgeschwindigkeit.

Stichwörter: Magnetische Kernresonanz**,** Magnetresonanz-tomographie, Miniaturisierung, homogenes Feld, Solenoidem Mikrospule, Niederfrequenzanalyse, ANSYS®**,** DOT-Optimierungssoftware, Modellordnungsreduktion, Modelbildung und Simulation, Optimierung

Introduction

A historical overview

The discovery and development of Magnetic Resonance Imaging (MRI), based on already discovered method Nuclear Magnetic Resonance (NMR), is one of the most spectacular and successful events in the history of medical imaging. Nuclear magnetic resonance has been discovered simultaneously and independently by Bloch and by Purcell in 1946 and first imaging experiments were done by Lauterbur and by Damadian in the 1970s [1].

Interest in the medical diagnostic possibilities of NMR began in 1971 with the study of the differences in relaxation times T_1 and T_2 between different tissues and between normal and cancerous tissue by Damadian. The first whole-body human chest scan was obtained in July 1977 in a 0.05 T home-made superconducting magnet with a scan time of 4.5 hours and resolution of the order of a centimeter. The technique was further developed to a scanning system with a permanent magnet of 0.3 T and became the first commercial MR scanner. An important improvement introduced by Garroway, Grannell and Mansfield in 1974 was the selective slice excitation technique that is generally used today, in which a field gradient perpendicular to the selected plane is applied during a tailored excitation pulse. Through a combination of excitation pulses and orthogonal gradient pulses a line scan technique was developed by the Mansfield group in Nottingham and used for the first human whole-body scan in 1978. In the mid-1980s there was a passionate debate on the subject of the optimum field strength of MR imagers between advocates of high field (1.5T) and low field (0.5 T) systems. The controversy faded away when the initial advantages of better signal to noise (S/N) ratio of 1.5 T imagers was later reduced by the development of improved signal detection techniques, which enabled low field system to produce images of excellent quality.

Improvement in signal detection, fast data handling and gradient technology, advanced understanding of spin systems, pulse sequences and artifact suppression have eventually eliminated the major problem of the scan time [3].

A quest for the highest possible resolution ensued, demanding the highest available magnetic and gradient field strengths. Now, we would like to mention how MRI is important through the review history of awarded Nobel Prizes on this field:

NMR has had a long and proud Nobel history, starting with the Physics prize awarded to Isaac Rabi in 1944 for his resonance method for recording the magnetic properties of atomic nuclei. Felix Bloch and Edward M. Purcell followed with the award in Physics in 1952. More recently, Chemistry Nobel Prizes were awarded to Richard Ernst in 1991 and Kurt Wüthrich in 2002. While Mansfield becomes the first physicist receiving a Nobel award in NMR-related work in more than 50 years, Lauterbur is the third chemist to receive the Nobel Prize for research in the area of NMR since 1991.The Nobel Prize in Medicine awarded in December 2003 to chemist Paul C. Lauterbur and physicist Peter Mansfield for the development of magnetic resonance imaging (MRI) constituted a long overdue recognition of the huge impact MRI has had in medical diagnostics and research [2]. The use of MRI for the diagnosis of brain and spinal ailments, for the pre- and post-operative studies of cancerous tumors and for the investigation of ligament damage four notable examples, there are many others has made MRI nearly ubiquitous in modern society. Both the 2003 Nobel Laureates were pursuing research in NMR that led them to their seminal studies in the development of MRI. Lauterbur had more than a decade's worth of research with multi-nuclear NMR ongoing whereas Mansfield was more than six years into his investigations of solid-state NMR by the time their primary work began in the early 1970s, leading to the creation of MRI

as we know it. Lauterbur was first to publish his initial discovery, a discovery that still strongly impacts chemical research today. He showed how variations in the strength of a magnetic field could be used to provide spatial information. Up until this discovery, variations, or gradients, in the strength of the magnetic field was the demon of NMR, an undesirable feature to be obliterated at all cost. Lauterbur managed to turn magnetic field gradients, one of the most problematic issues in NMR on their head, to the good fortune and better health of us all. In 2003, there were approximately 10,000 MRI units worldwide, and approximately 75 million MRI scans per year performed. As the field of MRI continues to grow, so do the opportunities in MRI [8].

Application in micro-world

With the development of mainly clinical MRI, the imaging of smaller biological or other samples became the preserve of only a few. Interest in the field was re-awakened by the publication in Nature of an image of a toad's egg [24]. This 'single cell' image demonstrated that high-resolution microscopy was possible and of interest to biological scientists. Clinical MRI had, by now, established itself, providing functional (flow, diffusion and perfusion) as well as just morphological information. The scientific community could now see that magnetic resonance microscopy (MRM) could provide dynamic information about the state of the sample which was not achievable with destructive imaging techniques. MRM expanded rapidly in fields such as plant biology, polymers and porous media, aided by the availability of wider bore high-field magnets suitable for imaging. Micro magnetic resonance imaging (Micro-MRI) technology is similar to clinical MRI and optimized for the study of small structures such as single cells. Micro-MRI refers to high resolution MRI.

In general, MRI suffers by low limits of detection. Over the past thirty years, the major advance in improving limits of detection (LODs) or sensitivity of NMR or MRI has been achieved in magnet technology, with steadily increasing static field strengths. Furthermore, probe miniaturization also may help to increase the sensitivity. But still the extraction of the Nuclear Magnetic Resonance (NMR) spectra of samples having smaller and smaller volumes is a real challenge and careful design of the radiofrequency coils as a NMR signal detector, ensuring an optimum reception of the NMR signal, are required. For this purpose, several probe design criteria such as producing a uniform magnetic field, increasing signal to noise ratio, susceptibility matching etc should be fulfilled.

Outline of this project

In chapter 1 we introduce the principle of magnetic imaging and in the last part of the first chapter, we declare that the detection limits of Micro-MRI or MRM can be pushed further by taking advantage of microsystem fabrication techniques, on the other hand, by miniaturization of the probes. Another important thing in MRI and its receiver coil, to which attention should be paid, is magnetic field homogeneity. Homogeneity may increase an image's resolution. In chapter 1 we describe why magnetic field uniformity is so important.

Chapter 2 is dedicated to probe miniaturization in MRI and the rationale for using microcoils. The coil design criteria are the important part of the second chapter, too. Finally, the conventional microcoil types which are widely used in imaging or NMR spectroscopy will be introduced and compared with respect to their field homogeneity, sensitivity and intrinsic signal to noise ratio.

In order to design an appropriate microcoil, one should simulate its electromagnetic behavior. Thus, one needs to deal with a set of governing equations named after Maxwell

and to solve them in an appropriate way. In chapter 3 we introduce the basics of electromagnetism in the frame of Maxwell's equations and then the numerical solution of these equations by means of Finite Element Method (FEM) will be discussed. Chapter 4 deals with implementation a FEM technique to build a model and simulate it by means of the multi-physics software ANSYS.

In chapter 5, with focus on the best coil design, we try to implement the optimization theory to optimize the shape design parameters using the DOT software. And finally, in order to speed up the microcoil's ANSYS harmonic analysis, we try to introduce and implement a model order reduction technique coupled to ANSYS and compare the results with respect to computational time and accuracy, in chapter 6.

1 NMR Principles and Micro-MRI

This chapter is divided into two main parts. First, we introduce the physical basics of NMR and then elaborate some its applications in cellular imaging. Furthermore, we try to give answer to this question: Why the uniformity of magnetic field is important?

1.1 Basic concepts of NMR

The elementary particle spin is a value that can be observed by placing electrons or nuclei in a magnetic field. They behave like small magnetic dipoles. In many cases, it is convenient to treat the spin as an angular momentum caused by rotating charges, but without the radiation of electromagnetic energy.

1.1.1 Spin and its quasi-classical treatment

In the quantum mechanical treatment, the behavior of spin may be analyzed using expectancy values. For all practical purposes, such as MRI, a quasi-classical treatment which takes into account quantized properties but uses classical mechanics to describe spin behavior is more convenient and yields the same results. More information can be found in [6, 7].

For the quasi-classical treatment of spin in an external magnetic field, we consider the concept of "spin" as a body rotating around its internal axis. See Figure 1.1:

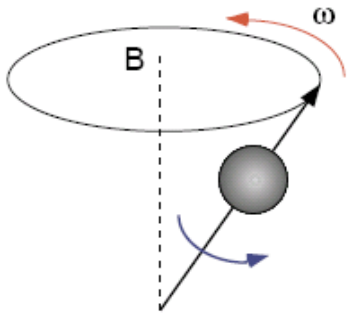

Figure 1.1: Rotation of the nuclear momentum about its own axis and about the magnetic field axis [6].

Then, every nuclei with non-zero nuclear spin I posses a non-zero magnetic dipole moment μ_i^m which is related to its angular momentum J_i by

$$\mu_i^m = \gamma J_i \qquad (1.1)$$

The ratio γ is called the gyromagnetic ratio and has a different value for each type of nucleus. Table 1.1 lists a few isotopes observed by Nuclear Magnetic Resonance (NMR) and their spin value, gyromagnetic ratio and abundance.

Nuclei with large γ are most easily detected by NMR technique. Almost every element in the periodic table has an isotope with a non-zero nuclear spin. NMR can only be performed on isotopes whose natural abundance is high enough to be detected. ^{1}H nuclei, due to its large γ and high natural abundance, are extensively used in a NMR spectroscopy.
In NMR, signals originating from the protons of tissue water are observed.

The angular momentum is a vector quantity $J = (J_x, J_y, J_z)$**.** The z component of J, in a magnetic field $H = (0, 0, H_z)$, will be quantized:

$$J_z = m_I \frac{h}{2\pi} \qquad (1.2)$$

where $m_I = -I, -I+1, ..., 0, ..., I-1, I$, I is the total spin number and h is a Planck's constant (ħ= h / 2л).

Isotope	Unpaired p^+	Unpaired n^o	Total spin I	$\frac{\gamma}{2\pi}$ [MHz/T]	Natural abundance[%]
^{1}H	1	0	1/2	42.58	99.985
^{2}H	1	1	1	6.54	0.015
^{13}C	0	1	1/2	10.71	1.110
^{19}F	1	0	1/2	40.08	100.000
^{23}Na	1	2	3/2	11.27	100.000
^{31}P	1	0	1/2	17.25	100.000

Table 1.1: Magnetic properties of selected particles which are used in NMR [8]

When placed in a static external magnetic field $H_0 = (0, 0, H_z)$, nuclei with nuclear spin I can adopt one of the spin states (1/2 or -1/2 for I=1/2 and 1, 0 or -1 for I=1) corresponding to possible orientations of the magnetic moment μ_i^m (parallel or anti-parallel to H_0, in the case of I=1/2). Figure 1.2 illustrates the resulting possible spin values for atoms having I=1/2 and I=1.

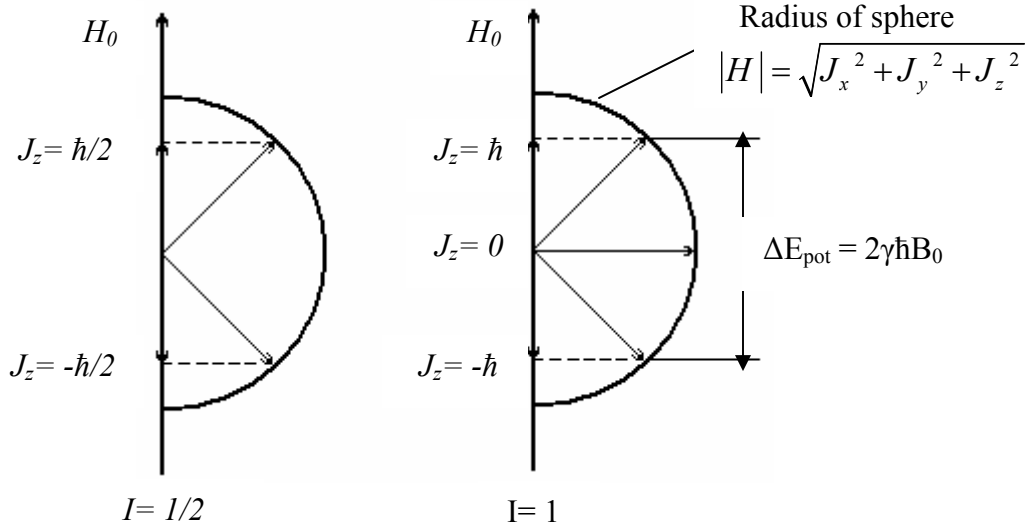

Figure 1.2: The quantized angular momentum and possible energy levels for particles with total spin I=1/2 and I=1 when placed into an external magnetic field $H_0 = (0, 0, H_z)$ [6].

The two states are separated by an energy amount ΔE_{pot}

$$\Delta E_{pot} = \frac{h\gamma\mu_0\mu_r H_0}{2\pi} \qquad (1.3)$$

Where, μ_0 and μ_r are respectively the intrinsic and relative magnetic permeability.

Since $\mu_0\,\mu_r H_0 = B_0$ and $\hbar = h/2\pi$ we can rewrite this equation as bellows:

$$\Delta E_{pot} = \hbar\gamma B_0 \qquad (1.4)$$

Where B_0 is the static magnetic flux density.

The nuclei can undergo a transition between two energy states by absorption or emission of a photon. Particles or nuclei in the lower energy state absorb a electromagnetic wave (a

photon) and ends up in the upper energy state. The energy of this photon ($E_{mag} = h\nu$, where ν is a frequency) must exactly match the energy difference between the two states. Therefore

$$E_{mag} = \Delta E_{pot} \Rightarrow h\nu_0 = \hbar\gamma B_0 \quad (1.5)$$

In NMR and MRI, the quantity $2\pi\nu$ is called the resonance frequency and the Larmor frequency, therefore we can write:

$$\omega_0 = 2\pi\nu_0 = \gamma B_0 \quad (1.6)$$

In the NMR experiment, the frequency of the photon is in the radio frequency (RF) range. In NMR spectroscopy, ν is between 60 and 800 MHz for hydrogen nuclei [8].

When a group of spins is placed in a magnetic field, each spin aligns in one of the two possible orientations. At room temperature, the number of spins in the lower energy level, N_α, slightly outnumbers the number in the upper level, N_β. Boltzmann statistics tells us that

$$\frac{N_\beta}{N_\alpha} = \exp(-\frac{\Delta E}{k_\beta T}) \quad (1.7)$$

Where ΔE is the energy difference between the spin states; k_β is Boltzmann constant, 1.3805x10^{-23} J/Kelvin; and T is the temperature in Kelvin. As the temperature decreases, so does the ratio N_β/N_α. As the temperature increases, the ratio approaches one. The signal in NMR spectroscopy results from the difference between the energy absorbed by the spins which make a transition from the lower energy state to the higher energy state, and the energy emitted by the spins which simultaneously make a transition from the higher energy state to the lower energy state. The signal is thus proportional to the population difference between the states. At thermal equilibrium, the lower energy state (parallel) is slightly more populated than the upper one (anti-parallel). For example at 7 T and room temperature, the population difference is on the order of 20 ppm. This small difference is responsible for the intrinsic low sensitivity of NMR compared to other spectroscopy methods [7]. But, NMR is a rather sensitive spectroscopy since it is capable of detecting these very small population differences. It is the resonance, or exchange of energy at a specific frequency between the spins and the spectrometer, which gives NMR its sensitivity.

1.1.2 The macroscopic behavior of spin

Till now, we have discussed about a single spin and its behavior, but The NMR experiment measures a large ensemble of spins derived from a huge number of molecules. Therefore, we now look at the macroscopic behavior.

The sum of the dipole moments of all nuclei is called magnetization (M):

$$M(M_x, M_y, M_z) = \sum \mu_i^m = \sum \gamma J_i \quad (1.8)$$

In equilibrium the spins of I=1/2 nuclei are either in the α- or β-state and rotate about the axis of the static magnetic field. However, their phases are *not correlated*. For each vector pointing in one direction of the transverse plane a corresponding vector can be found which points into the *opposite* direction. Therefore, the projection of all vectors onto the x-y plane (the vector sum of the transverse components) is vanishing provided that the phases of the spins are uncorrelated. Figure 1.3 shows the equilibrium state with similarly populated states and the phases.

However, application of a radiofrequency (RF) field, the so-called B_1 field, *perpendicular* to the magnetic field (e.g. along the x- or y-axis) creates a state in which the phases of the spins are *partially* correlated. This state is called coherence. When projecting the vectors onto the x-y plane the resulting transverse magnetization is non-vanishing giving rise to a

signal in the detection coil. Figure 1.4 shows the coherent state when the orthogonal B_1 field applied by means of the radiofrequency coil.

The experiment setup of the NMR includes a radiofrequency coil, which delivers the orthogonal B_1 field. Simultaneously this coil serves to pick up the NMR signal.

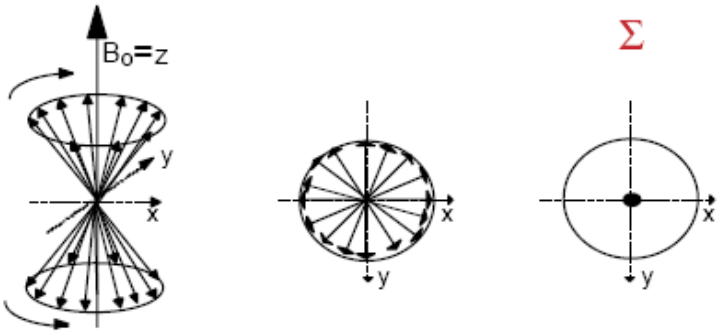

Figure 1.3: Equilibrium state with similarly populated α- and β-states (left), uncorrelated phases (middle) and no net phase coherence (right)[6].

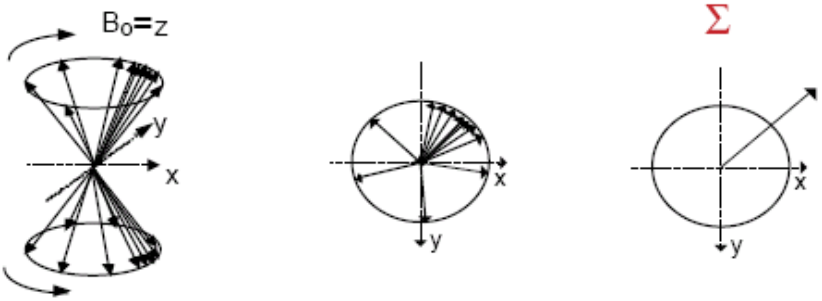

Figure 1.4: Coherent state of spins in α- or β (left) states and the projection onto the x-y plane (middle) and sum vector of the x-y component (right) [6].

To understand how the magnetization that rotates in the transverse (x, y) plane induces the NMR signal it is convenient to look at the vector sum of the transverse components which present a magnetic field that rotates in space. Figure 1.5 illustrates the spins precessing at different velocities (for different compounds in the sample).

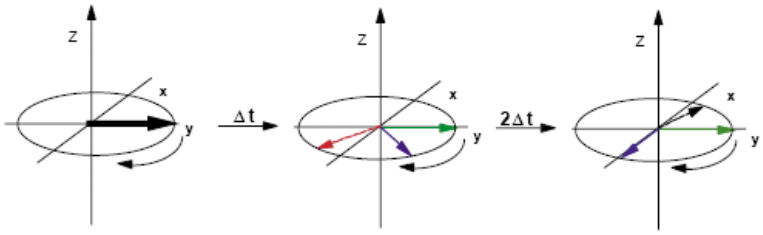

Figure 1.5: Spins precessing at different velocities (and hence have different chemical shifts) are color coded [6].

The magnitude of the current that is induced in the receiving coil depends on the orientation of the magnetization vector with respect to the coil. When the magnetization is pointing towards the coil the induced current is at maximum. Because the magnetization rotates the induced current follows a sine (or cosine) wave. Spins with different chemical shift, different Larmor frequencies, precess at different rates and hence the frequency of the current is the Larmor frequency, e.g. the frequency of the precessing spins. See figure 1.6.

Spins that belong to nuclei with different chemical environment precess with different frequencies. For more complex compounds that contain many different spins the signal in the receiver coil is a superposition of many different frequencies. The Fourier Transformation (FT) is a convenient mathematical tool for simultaneous extraction of all

frequency components. It allows transforming data from the time into the frequency domain. Figure 1.7 depicts how the Fourier Transformation extracts all the frequency components and pave the ways to make spectroscopy analysis in NMR.

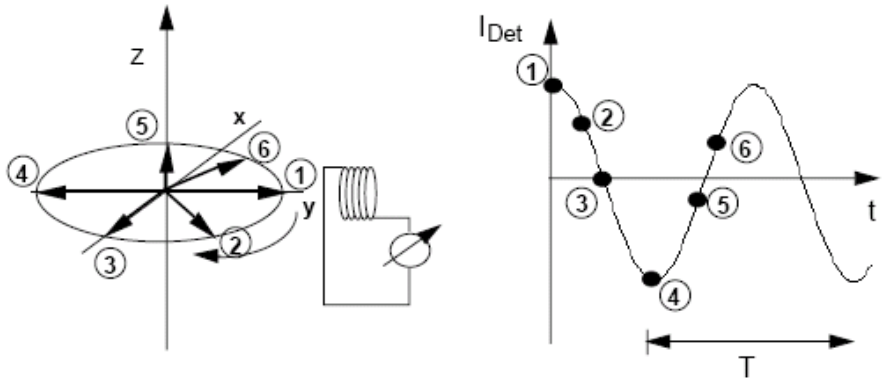

Figure 1.6: Left: Rotating spin with its position at certain time intervals 1-6 are marked. Right: Corresponding signal in the receiver coil [6].

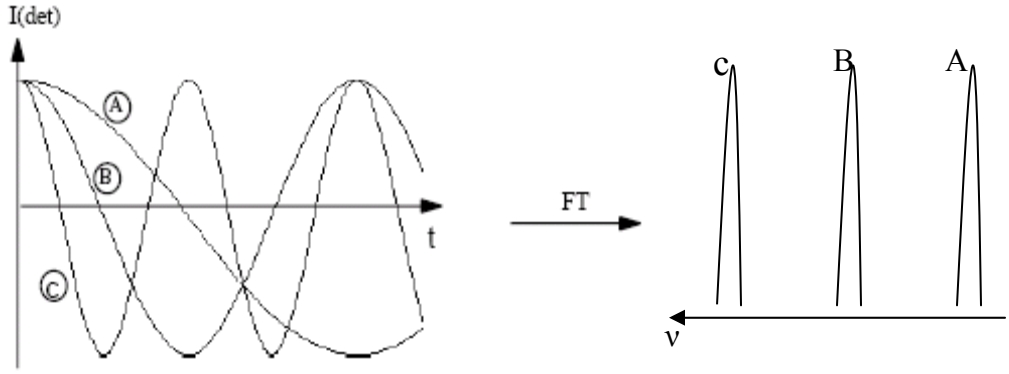

Figure 1.7: Signals from 3 spins with different precession frequencies (left) and their corresponding Fourier transforms (right)[6].

1.1.3 Relaxation Process

When only the static B_0 field is present the spins precess about the z-Axis (the axis of the B_0 field). To create spin-coherence an additional RF field is switched on, that is perpendicular to the axis of the static field (the so-called B_1 field). To emphasize that this field is turned on for only a very short period of time usually it is called a (RF) pulse. During the time where B_0 and B_1 field are both present the magnetization rotates about the axis of the resulting effective field. The effective field is calculated by taking the vector sum of the B_0 and B_1 field.

The magnetization does not precess infinitely in the transverse plane but turns back to the equilibrium state. This process is called relaxation. Two different time-constants describe this behavior:

a) The re-establishment of the equilibrium α-β state distribution ($\mathbf{T_1}$).
b) De-phasing of the transverse component (destruction of the coherent state) which is called $\mathbf{T_2}$. The T_2 constant characterizes the exponential decay of the signal in the receiver coil.

The precessing spins slowly return to the z-axis. Instead of moving circularly in the transverse plane they slowly follow a spiral trajectory until they have reached their initial position aligned with the z-axis (see figure 1.8):

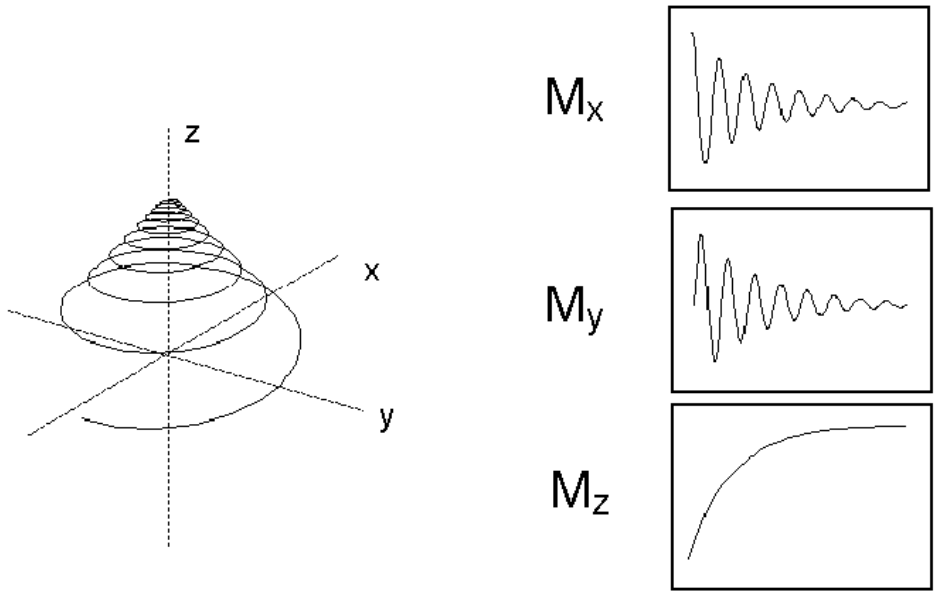

Figure 1.8: left: Trajectory of the magnetization, right: individual x, y and z component

1.1.4 Bloch Equations

The effect of the B_1 field on transverse and longitudinal magnetization is described by Bloch equations. When a dipole moment placed inside a magnetic field, a force (a torque) acts on it such that the dipole moment will be aligned with the direction of the static magnetic field. Mathematically this is described by forming the vector product between dipole moment and magnetic field.

$$T = M \times B \tag{1.9}$$

Since T (a torque) is equal to $\partial J/\partial t$ and considering the equation 1.8, we can find that

$$\frac{\partial M}{\partial t} = \gamma \frac{\partial}{\partial t} J = \gamma T = \gamma (M \times B) \tag{1.10}$$

This equation describes the time evolution of the magnetization. In the presence of an additional B_1 field, the components of the field along the Cartesian axes are:

$$B_x = B_1 \cos \omega_0 t$$
$$B_y = B_1 \sin \omega_0 t$$
$$B_z = B_0$$

Thus, leads to the following set of coupled differential equations which describe the time evolution of the magnetization along the Cartesian axes [9]:

$$\begin{aligned}
\frac{\partial}{\partial t} M_x(t) &= \gamma (M_y B_0 + M_z B_1 \sin \omega_0 t) - (\frac{M_x}{T_2}) \\
\frac{\partial}{\partial t} M_y(t) &= -\gamma (M_x B_0 + M_z B_1 \cos \omega_0 t) - (\frac{M_y}{T_2}) \\
\frac{\partial}{\partial t} M_z(t) &= -\gamma (M_x B_1 \sin \omega_0 t + M_y B_1 \cos \omega_0 t) - (\frac{M_z - M_0}{T_1})
\end{aligned} \tag{1.11a}$$

Or:

$$\frac{\partial}{\partial t}M = \gamma \frac{\partial}{\partial t}J = \gamma T = \gamma(M \times B) - \begin{bmatrix} \frac{M_x}{T_2} \\ \frac{M_y}{T_2} \\ \frac{(M_z - M_0)}{T_1} \end{bmatrix} \quad (1.11b)$$

1.1.5 Relaxation process and signal detection

Both excitation and detection can be done using a solenoidal coil enclosing the sample with its axis perpendicular to B_0. Here, we restrict ourselves to find a solution for equation 1.11b under ideal pulse conditions, considering that an alternating magnetic field $B_{1x}(t)$ at frequency ω_0 applied as an excitation pulse for a duration $\boldsymbol{\tau}$. After a pulse duration $\boldsymbol{\tau}$, the magnetization in the laboratory frame of reference is governed by the following set of equations [9]:

$$\begin{aligned} M_x(t) &= M_0 \sin(\theta) e^{-t/T_2} \sin(\omega_0 t) \\ M_y(t) &= M_0 \sin(\theta) e^{-t/T_2} \cos(\omega_0 t) \\ M_z(t) &= M_0(1 - e^{-t/T_1}) + M_0 \cos(\theta) e^{-t/T_1} \end{aligned} \quad (1.12)$$

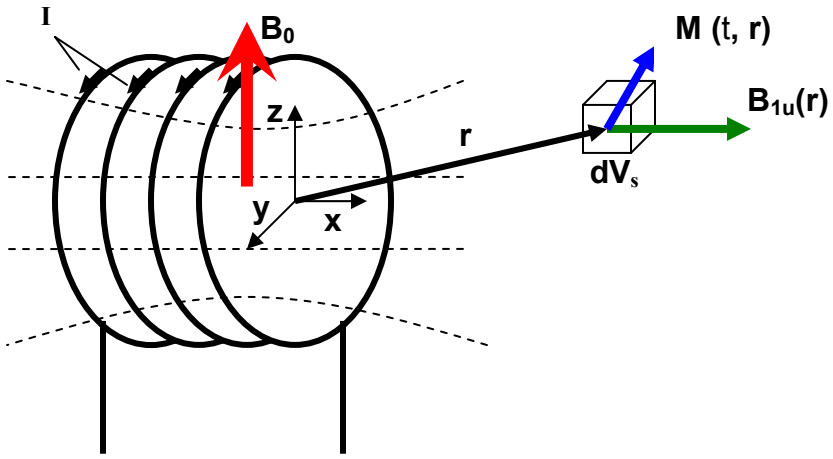

Figure 1.9 Schematic coil configurations for detecting an NMR signal.

Where, M_0 is a bulk magnetization aligned along B_0 and the θ the excitation flip angle given by:

$$\theta = \gamma B_1 \boldsymbol{\tau} \quad (1.13)$$

After the excitation pulse, the NMR signal is obtained by measuring the voltage induced in the detection coil by the rotating magnetization, while it returns to its equilibrium position along the z-axis. For the purpose of quantifying the signal detected by a particular coil, it is useful to introduce the unitary magnetic field $B_{1u}(r)$, corresponding to the field that would be produce by a DC current of 1 Ampere flowing through the coil. The voltage induced for an elementary sample volume dV_S at position r is given by the principle of reciprocity [5]. This

principle states that the induced electromotive force ζ is directly related to the strength of the magnetic field $B_{1u}(r)$ (see figure 1.9).

$$\zeta(t,r) = -\frac{\delta}{\delta t}((B_{1u}(r).M(t,r)))dV_s \qquad (1.14)$$

In most of the NMR systems the excitation coil is also used as detection coil [4]. Thus, we consider the same coil as a detection coil sensitive to variation of the magnetization along the x-axis and assume a uniform magnetic field distribution $B_{1u}(r)=B_{1u}x$ and magnetization $M(r)=M_0z$ in the whole sample volume V_S. The induced voltage after a 90º excitation pulse may be expressed as (by combining equation (1.12) and (1.14), with an appropriate phase delay):

$$S(t) = \int_{V_s} \zeta(t) = \omega_0 M_0 B_{1u} V_s \cos(\omega_0 t) e^{-t/T_2} \qquad (1.15)$$

And has the maximum initial amplitude**:**

$$S_0 = s(t)_{t=0} = \omega_0 M_0 B_{1u} V_s \qquad (1.16)$$

Therefore, the NMR signal is measured in the time domain as an oscillating decaying voltage induced in the receiver coil by the magnetization in free precession. This signal is known as the Free Induction Decay (FID) (see figure 1.10 left).

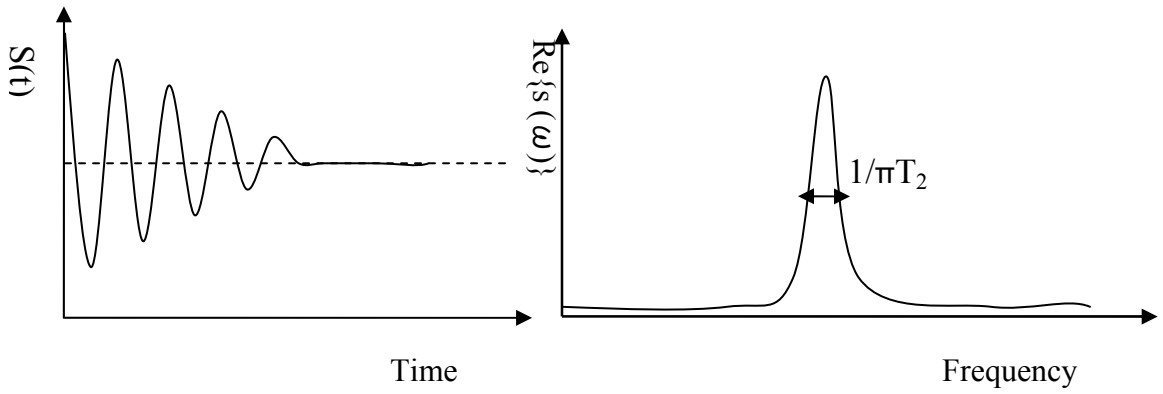

Figure 1.10 Left: Time-domain NMR signal (FID) and right: Fourier transform (frequency domain)

In many NMR experiments, the time-domain FID of equation (1.15) is transformed in the frequency-domain by a Fourier Transform [7]. The real part of the resulting Fourier transform is a Lorentzian and the Full Width at the Half Maximum (FWHM) of the real part is given by $1/\pi T_2$, while the maximum amplitude at the resonance is:

$$A_0 = \frac{1}{2} S_0 T_2 \qquad (1.17)$$

It means that the line-width (resolution) and the amplitude of the NMR signal, in the frequency-domain, clearly depend on the relaxation time ($\mathbf{T_2}$).

1.1.6 The importance of magnetic field uniformity

The definition of RF homogeneity requirements, and their incorporation into receiver coil design, generally requires a basic understanding of NMR signal detection, which has been already discussed in the previous pages. In addition to the distortions of magnetic field homogeneity which are caused by the sample at the high magnetic fields, additional distortions will be caused by the RF coil at the small size scales used in NMR. These

distortions are very difficult to correct with shim coils *, since most standard shim coils will not be effective over the small dimensions of the sample [12].In the presence, within the sample, of a perturbation field $\Delta B(r)$ superposed to the polarizing field B_0, the resonance frequency ω_0 becomes position-dependant (consider equation 1.6):

$$\omega_0(r) = \gamma\left|B_0 + \Delta B(r)\right| = \gamma\left|B(r)\right| \tag{1.18}$$

Combined with equation 1.12, equation 1.18 implies that the magnetization corresponding to spin packets at various locations will rotate at different frequencies in the xy-plane. As a function of time, this results in a loss of coherence of the transverse magnetization and thus a more rapid decay of the FID than that due to T_2 relaxation only. (Assuming the perturbation of the field-strength distribution to be Lorentzian, the spin-spin relaxation T_2 may be replaced by an effective relaxation time T_2^*) [7]. In the frequency-domain, this corresponds to an additional broadening of the resonance line. From equation 1.17, we observe that an inhomogeneous static magnetic field not only increase linewidth, but also decreases the signal amplitude in the frequency-domain. As mentioned, using the principle of reciprocity (equation 1.14), we can write the signal detected per unit volume as:

$$\xi_{puv}(r) = \omega_0 B_{xy}(r) M_{xy}(r) \tag{1.19}$$

If we illustrate M_{xy} *(r)* and B_{xy} *(r)* at each point r in terms of variations ΔM_{xy} *(r)* and ΔB_{xy} *(r)* from values M_{xy} *(0) and* B_{xy} *(0)* defined at the coil center [10]:

$$\xi_{puv}(r) = \omega_0(B_{xy}(0) - \Delta B_{xy}(r)) \times (M_{xy}(0) - \Delta M_{xy}(r)) \tag{1.20}$$

The fractional deviation of a NMR response at any point r relative to the response at the center of a coil $\xi_{puv}(0)$ is then given by

$$\frac{\xi_{puv}(0) - \xi_{puv}(r)}{\xi_{puv}(0)} = \frac{\Delta B_{xy}(r)}{B_{xy}(0)} + \frac{\Delta M_{xy}(r)}{M_{xy}(0)} - \left(\frac{\Delta B_{xy}(r)}{B_{xy}(0)}\right)\left(\frac{\Delta M_{xy}(r)}{M_{xy}(0)}\right) \tag{1.21}$$

This equation shows how the NMR signal depends on local value of the transverse magnetization M_{xy} *(r)* and the field strength B_{xy} *(r)*.

Now, it is easy to understand why a MR image, with high spatial resolution in three dimensions, requires a highly homogenous magnetic field within the region of interest and an inhomogenous magnetic field will lead to image artifacts due to the localized variations in spin precession frequency [10].

1.1.7 How to treat uniformity

There exist several ways in which the acquired FID may be treated in order to improve the resulting NMR spectrum. One of the methods is known as apodization [7]. If the signal decays rapidly as a result of magnetic field inhomogeneity (i.e. short T_2*), the lines, as already discussed, are intrinsically broad and there is no point in collection data for a long time. Additionally, mostly noise will be acquired in the later part of the acquisition time, degrading Signal to Noise Ratio (SNR).

The acquisition time should therefore be chosen according to the experimental conditions. Assuming an exponential decay with a time constant T_2*, the signal-to-noise ratio can be maximized by multiplying the original time-domain signal by a function called the matched weighting function:

$$h_m(t) = e^{-t/T_2^*} \tag{1.22}$$

By this process, the later part of the FID containing a higher proportion noise is suppressed, resulting in a higher apparent signal-to-noise. The trade-off is a resonance line

---

* Shim coil: The shim system is a device that corrects for locally slightly different magnetic fields.

broadened by a factor of 2. If such broadening is unacceptable, the time constant of the weighting function can be increased to a value when line broadening becomes insignificant. In this case, the spectral line can be sharpened, but at the cost of SNR [7].

Another way to treat the inhomogeneity, before doing any experimental setting improvements, is to optimize the coil shape in order to decrease magnetic field non-uniformity within the coil, which is the final goal of this project.

1.2 NMR application in cellular imaging(Limits and Advantages)

In this section we introduce a very special application of the nuclear magnetic resonance in biology and medical sciences and leave the other applications which are not correspondent to our goals undiscussed.

As already discussed, clinical MRI could provide functional (flow, diffusion and perfusion) and morphological information. Magnetic resonance microscopy (MRM) provides dynamic information about the state of the sample which was not achievable with destructive imaging techniques. (Micro-MRI) technology is similar to clinical MRI and optimized for the study of small structures such as single cells. Micro-MRI refers to high resolution MRI. It is based on the physical phenomenon of Nuclear Magnetic Resonance (NMR). “High-resolution” here means a resolved voxel volume in the range of 10 × 10 × 10 μm³ = 1 pl. (For standard clinical applications, the resolution is about 1 × 1 × 1 mm³ = 1 μl). A request for the highest possible resolution demands the highest available magnetic and gradient field strengths. In general, for the very high resolution a combination of high magnetic field strength (>10 T), high gradient field strength (in region of 1 Tm^{-1}*)* and a highly sensitive RF coil having a high filling factor (90% if coil encloses whole sample, or a surface coil which is optimal for a region of interest) is required [15]. But, there are practical limits imposed by magnetic field strength and imaging time which currently limit practical resolution to about 1.0μm. Ostensibly this limit has been reached [15]. Some limits of solid, liquid and gas states have been already discussed in details by P. Glover and P. Mansfield [15]. For Further studies on limits, one can refer to this article.

The highest resolution reported for Micro-MRI to date has been achieved by Lee et al. with a resolved voxel volume of 75 μm³ (1 × 1 × 75 μm³) [16]. Thus, MR microscopy of cells has advanced to voxel resolutions of just a few microns in all three spatial dimensions, and to as little as one micron ‘in-plane’ resolution.

Here, we would like to show some images obtained by Micro-MRI technique and to introduce the currently resolution limits of this method. The image shown in figure 1.11 has 2 μm in-plane resolution, with 200 μm^3 voxel volume. While the images obtained by Lee et al. have excellent in-plane resolution, the relatively large slice thickness is not adequate for imaging objects lacking 2D symmetry. By employing magnetic field gradients as large as 5.8 T/m, micro-receiver coils with diameters smaller than 100 μm and a ‘constant-time-imaging’ pulse sequence [20, 21] Ciobanu et al. report fully three dimensional images obtained on both phantoms and real biological samples. Figure 1.12 shows the 3D image from Ref. [22]. Figure 1.13 shows the Ciobanu et al. image of a spirogyra alga. [13] The spirogyra (see microscope photo in figure 1.13a) is cigar-shaped, with diameter 40 μm. The micro-pipette containing the spirogyra cell, immersed in water, as shown in figure 1.13a, has inner diameter 55 μm. The micro-coil 250 μm long, covers 5–6 chloroplast spiral windings. The MR image is shown in figure 1.13b.

Despite of having resolution limits, the strength of Micro-MRI is to reveal information that cannot be obtained by non-invasive way. For example, it becomes possible to analyze *in vivo* distribution of metabolites in the cell matrix, local mapping of water diffusion constant or

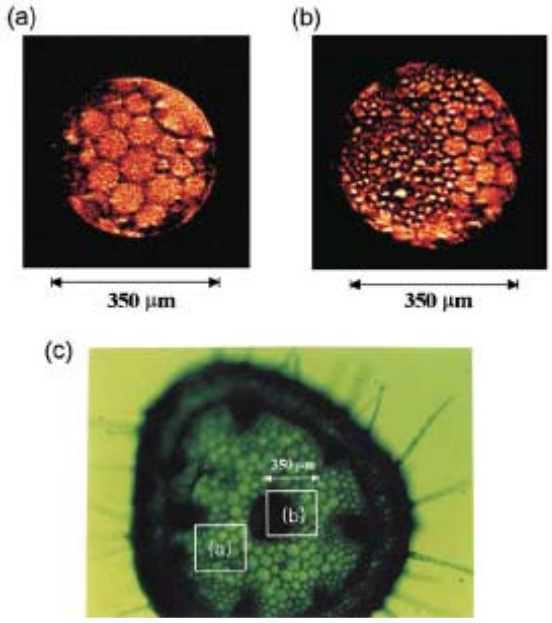

Figure 1.11 The ^{1}H images [16] at 14.1 T of geranium leaf stems in the large (a) and small (b) cell regions with voxel size of 2 x 2 x 50 μm^3. (c) An optical microscope image of the geranium leaf stem Reprinted from Ref. [16]

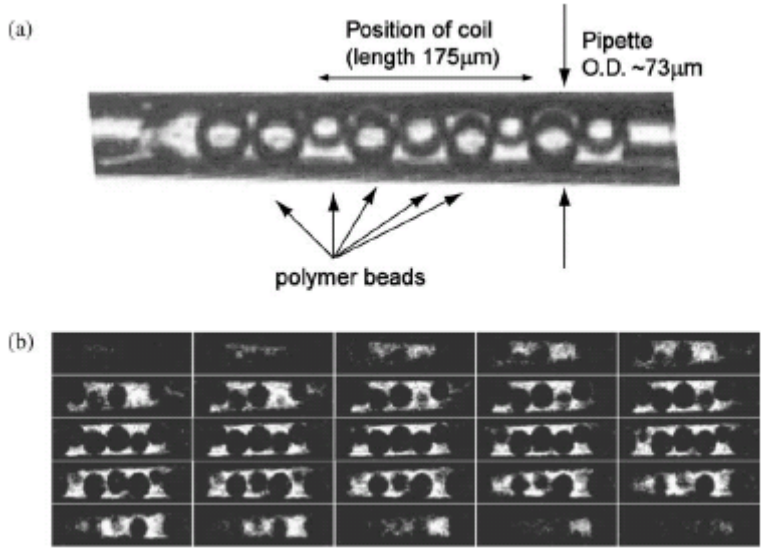

Figure 1.12. (a) Microscope photograph [22] of sample imaged in (b). The sample consists of a quartz micro-capillary, initially 1 mm outer diameter, pulled to an outer diameter of 73 μm and inner diameter 53 μm, filled with water and 39 μm diameter fluorescent polymer beads. (b) 3D MRI microscopy ^{1}H image of the sample shown in (a) (at 9 T). Reprinted from Ref. [22].

spatially resolved microspectroscopic analysis. Thus, it can provide a unique view of a variety of physiological processes. Furthermore, the applied magnetic fields have no known influence upon the living organism. That makes it possible to observe the undisturbed

object. In a way, this is like overcoming the “biological uncertainty principle”, because other single-cell microbiology techniques, such as e.g. fluorescence microspectroscopy or flow

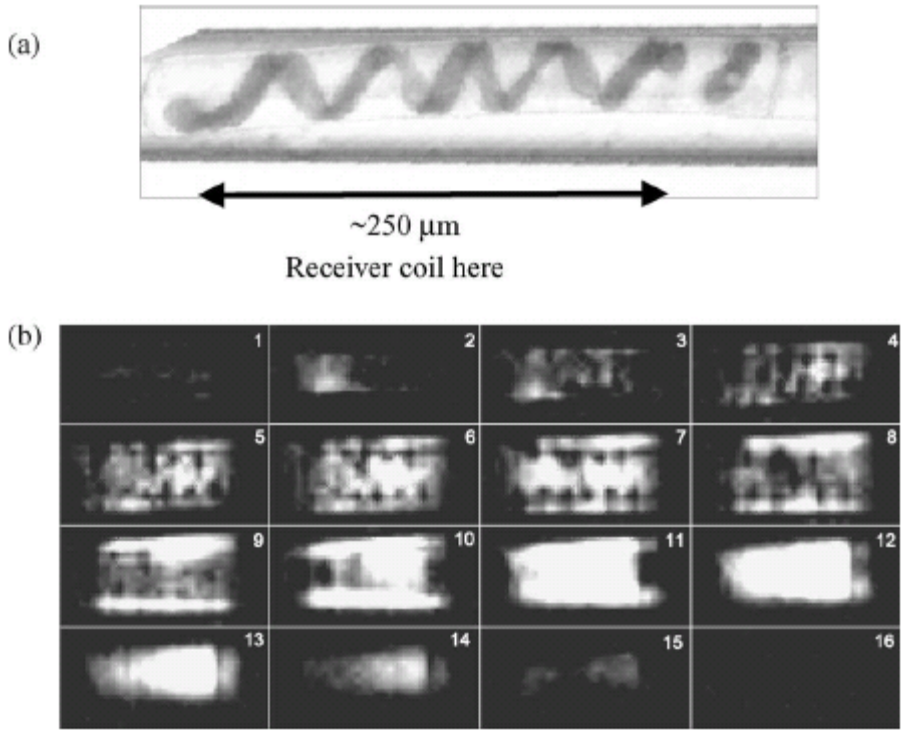

Figure 1. 13 (a) Microscope photograph [13] of the sample imaged in (b). The sample consists of a single cell spirogyra alga of cylindrical shape with diameter 40 µm and length of several hundred microns. The NMR receiver coil is wound over a span of 250 µm located in the figure. (b) 3D MRI microscopy ^{1}H image of the sample shown in (a) (at 9 T). Reproduced from Ref. [13].

cytometry, manipulate the object of interest in some or the other way [14]. Another very important advantage is that the non-invasive, non-destructive nature of Micro-MRI allows for long-term studies of one and the same object, and thus simultaneously reduces the number of test objects needed [17, 18, 19].

NMR spectroscopy can be also used to determine the full tertiary structure of small organic compounds or proteins, which is of particular interest in the area of chemistry in therapeutic drug research. In the medical field, Micro-coils can be integrated with catheter tools, too. They are used for NMR spectroscopy or Micro-MRI of the intravascular walls, and they also can be used for catheter tracking [23].

For the future, Micro-MRI is an extremely promising technique to supplement existing single cell microbiology tools and techniques. The limits of detection and the resolvable voxel size have not yet reached its ultimate limits and can be pushed further by taking advantage of microsystem fabrication techniques. The full range of applications still remains to be developed.

2 Microcoil

Over the past thirty years, the major advance in improving limits of detection (LODs) or sensitivity of NMR or MRI has been in magnet technology, with steadily increasing static field strengths. Operating frequencies of 900 MHz has already been achieved. In the last part of the first chapter, we declare that the detection limits of Micro-MRI or MRM can be pushed further by taking advantage of microsystem fabrication techniques, on the other word, by miniaturization of the probes. In general, the radio frequency (RF) receiver coil should closely conform to the sample to ensure good detection sensitivity. A properly designed NMR probe will maximize both the observe factor, which is the ratio of the sample volume being observed by the RF coil to the total sample volume required for analysis, and the filling factor, the ratio of the sample volume being observed by the RF coil to the coil volume [32].

The miniaturization of NMR probes thus involves two advantages:

1) Increased sensitivity which without it the analysis of such low concentration compounds would be impossible, and

2) Increase of filling factor by matching the probe to the sample volume [14].

But still the extraction of the Nuclear Magnetic Resonance (NMR) spectra of samples having smaller and smaller volumes is a real challenge. Either these reductions of volume are dictated by the difficulties of production of sufficiently large samples or by the necessities of miniaturization of the analysing system, in both cases a careful design of the radiofrequency coils, ensuring an optimum reception of the NMR signal, are required.

2.1 Coil design and rationale for miniaturization

In this chapter, we will discuss the coil design theory and the rationale for the coil miniaturization, in details.

2.1.1 Sensitivity analysis

Thus, the second approach to improving NMR LODs is the use of extremely small coils (microcoil) as magnetic resonance detectors. It has long been recognized that reducing the diameter of the coil increases its sensitivity [25, 26].

The exact definition of a size range for defining a "microcoil" is somewhat arbitrary, and indeed has never explicitly been defined in the literature. For the purpose of this project, we limit the term microcoil to any coil having a size in micron (μ) range from 1 to 100s μ. Now, we try to derive equations which describe the intrinsic sensitivity of RF coils, showing why this sensitivity increases as the diameter of coil is reduced. The solenoidal geometry is highlighted, since it comprises the majority of NMR or MRI microcoils constructed so far.

The signal-to-noise ratio (SNR) is a well accepted standard to measure the quality of an NMR experiment, both for spectroscopy and imaging studies. The signal-to-noise ratio of a NMR experiment is defined as the peak signal divided by the root mean square (rms) of noise [25, 26]:

$$SNR = \frac{k_0 \frac{B_1}{i} V_s N \gamma \frac{h^2}{4\pi^2} I(I+1) \frac{{\omega_0}^2}{kT\, 3\sqrt{2}}}{V_{noise}} \qquad (2.1)$$

Where k_0 is a constant which accounts for spatial inhomogeneities B_1 field, k is the Boltzmann's constant, I is the spin angular momentum quantum number, γ is the gyromagnetic ratio, N is the spin density (no. of spin per unit volume), h is Plank's constant, T is the absolute temperature measured in Kelvin, ω_0 is the Larmor frequency and finally the

factor B_1/i, the magnetic field per unit current, represents the coil sensitivity as can be understood by the principle of reciprocity.

The noise V_{noise} in an NMR experiment is primarily thermal noise which is generated in the receiver coil and sample and measured over the receiver's frequency bandwidth Δf:

$$V_{noise} = \sqrt{4kTR_t \Delta f} \tag{2.2}$$

Where T assumed to be a common sample and coil temperature [K] and R_t represents ohmic losses (will be discussed later in section 2.1.2).

If we express the SNR in terms of quantities that we may influence by coil design or changing the MRI experiment's setup the equation 2.1 can be rewritten as:

$$SNR \propto \frac{\omega_0^2 . \frac{B_1}{i}}{\sqrt{R_t}} \tag{2.3}$$

Which, as already discussed, $\omega_0 = \gamma B_0$ is Larmor frequency. Therefore, it makes sense to perform the MRI experiment with the highest field strength (B_0) available in order to get higher SNR.

Now, the question may arise what is directly related to the size of the receiver coil? The answer is the coil sensitivity (B_1/i). For a highly efficient RF coil it is the function $B_1/i\sqrt{R_t}$ which will reflect the overall SNR. It is obvious that this may be achieved by maximizing B_1/i, minimizing $\sqrt{R_t}$ or a combination of both.

For a solenoid of n turns (where n>>1), length h, radius r and carrying a current I, the spatial distribution of the magnetic field within the coil can be calculated from the Biot-Savart law. The implicit assumption is that the spacing between the coil turns is small compared to the radius of the coil, so that the current density can be approximated by a single-turn conducting sheet. The magnetic flux density (B) at the center of the coil is then given by [26]

$$B = \frac{\mu n i}{\sqrt{4r^2 + h^2}} \tag{2.4}$$

Where, μ is the permeability of free space. In the case of h>>r, this simplifies to

$$B = \frac{\mu n i}{h} \tag{2.5}$$

The on-axis magnetic flux density at either end of the coil (B_{end}) is given by

$$B_{end} = \frac{\mu n i}{2\sqrt{r^2 + h^2}} \tag{2.6}$$

Again, using the simplification that h>>r

$$B_{end} = \frac{\mu n i}{2h} \tag{2.7}$$

Therefore, the magnetic field at the ends of a solenoid is one half that at the center. In chapter 5 we will introduce a variable pitch in the coil to get optimum RF homogeneity in the center half of the sample space. In principle this is similar to the classical trick of so-called “end compensated” RF coils in which the outermost windings were squeezed to a slightly smaller pitch.

If equation (2.4) is re-expressed, then the sensitivity (B_1 /i) can be directly related to the diameter of the coil:

$$\frac{B_1}{i} = \frac{\mu n}{d\sqrt{1 + (\frac{h}{d})^2}} \tag{2.8}$$

Therefore, assuming that the length to diameter ratio (h/d) is kept constant, the coil sensitivity will increase at the inverse of the diameter of the coil (See figure 2.1). The graph in figure 2.1 (after Morris [27]) shows the SNR/volume variation with coil diameter (d). Down to a certain size, the graph has a d^{-1} characteristic as would be expected from above simple calculation. However, below this, the skin depth (will be discussed in section 2.1.3) of the conductor dominates and the gradient is $d^{-1/2}$. Morris estimates that the transition diameter is d = 300 μm at 300 MHz. At diameters less than 2 mm the coil's self-resistance dominates, biological samples of normal conductivity having little effect. This latter regime may be exploited further by reducing the self-resistance using high-temperature superconductive (HTS) films to build the coils.

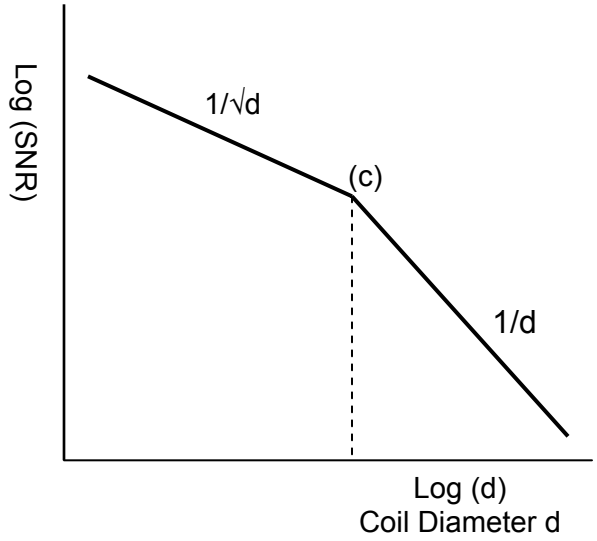

Figure 2.1 *Relationship between SNR per unit volume and solenoid coil diameter in the microscopic regime where sample loading may be neglected. The graph shows how the skin depth effect in the coil wires dominates for small diameters. The intercept at (c) depends on wire type and diameter, geometry and frequency. At 300MHz this would correspond to a coil of about 300µm diameter [15].*

So, solenoidal receiver coils that closely conform to the size and shape of small samples are effective for improving NMR sensitivity. But in practice, there are some limits to fabricate or using of small enough coils. Microcoils with diameters as small as 50 microns can be wound using conventional winding techniques [27]. The fabrication methods and comparisons have been discussed in ref. [14] in details. Three other factors can however limit a coil's minimum size, and therefore its SNR performance. These include the sample's overall dimensions, as well as the degree of spatial uniformity required in both static and RF magnetic fields [27].

2.1.2 Noise analysis

As already mentioned, the noise V_{noise} in an NMR experiment is primarily thermal noise which is generated in the receiver coil and sample and measured over the receiver's frequency bandwidth Δf (See equation 2.2). In this equation, T assumed to be a common sample and coil temperature [K] and R_t represents ohmic losses in the coil, connecting wires, tuning device as well as magnetic and dielectric losses in the sample and surrounding structures. The major sources of ohmic loss are the resistance of the coil itself, R_{coil}, and the wires connecting to the matching/tuning and amplification circuitry R_{lead}, and losses due to

eddy currents in the surrounding substrate, R_{AC} (will be discussed in section 2.1.3). Also, dielectric losses, $R_{diel,}$are not negligible in case of biological, conducting samples and can only be minimized by integration of distributed capacitance [11].

2.1.3 Skin and proximity effects

Now, we consider skin and proximity effects taking place in a coil's wire. When an alternating current is passed through a conducting wire, an alternating magnetic field is created with flux lines concentric with the axis of the wire. This field induces eddy currents within nearby wires and also within the wire itself [7]. The skin effect is the tendency of an alternating electric current (AC) to distribute itself within a conductor so that the current density near the surface of the conductor is greater than that at its core. That is, the electric current tends to flow at the "skin" of the conductor. The skin effect causes the effective resistance of the conductor to increase with the frequency of the current. The effect was first described in a paper by Horace Lamb in 1883 for the case of spherical conductors, and was generalized to conductors of any shape by Oliver Heaviside in 1885. The skin effect has practical consequences in the design of radio-frequency and microwave circuits [28, 29]. Figure 2.2 shows the skin effect and the skin depth (δ) within a conductor.

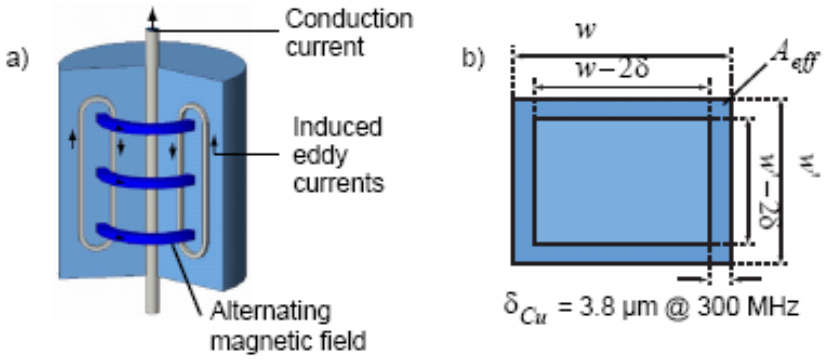

Figure 2.2 *Skin effect (left) and effective area A_{eff} (right) [14].*

Skin depth is defined as the depth below the surface of the conductor at which the current density decays to 1/e (about 0.37) of the current density at the surface. It can be calculated as follows [28]:

$$\delta = \sqrt{\frac{2\rho}{\omega\mu}} \tag{2.10}$$

Where ρ is resistivity of conductor, ω angular frequency of current = 2π x frequency and μ absolute magnetic permeability of conductor. For copper, the skin depth is around 3.8 μm at 300 MHz.

In physics, proximity effects are group of effects where substances behave differently when near, or proximate, to one another. If an AC current flows through one or more other nearby conductors, such as within a closely wound coil of wire, the distribution of current within the conductor will be constrained to smaller regions. The resulting current crowding is termed proximity effect [28, 29]. As a result, the current density becomes asymmetric. The

combination of skin and proximity effects significantly increase the AC resistance of the conductor when compared to its resistance to a DC current. At higher frequencies, the AC resistance of a conductor can easily exceed ten times its DC resistance. The additional resistance increases electrical losses which, in turn, generate undesireable heating. The coil AC resistance has often been axpressed as $\mathbf{R_{AC} = R_{DC}.(1+F+G)}$ which F is the skin effect and G the proximity effect factor [7, 33].

2.1.4 Equivalent circuit of a coil

An inductor coil has a complex impedance *Z*, which its real and imaginary parts vary as a function of frequency. It is convenient to replace the inductor by an equivalent circuit consisting of ideal circuit elements. The simplest equivalent is an inductance L in series with a resistance R. One can define the quality factor for a LR circuit as:

$$Q = \frac{|\mathrm{Im}\{Z\}|}{\mathrm{Re}\{Z\}} = \omega L/R \qquad (2.11)$$

(The Q-factor or quality factor is a measure of the rate at which a vibrating system dissipates its energy. A higher Q indicates a lower rate of energy dissipation. For example, a pendulum suspended from a high-quality bearing, oscillating in air, would have a low one. For very strong damping, Q<1, the system is so strongly damped that it never completes a single oscillation and in the limit of Q = 0, it simply decays exponentially toward equilibrium. When the system is driven, its resonant behavior depends strongly on Q. Resonant systems respond to frequencies close to their natural frequency much more strongly than they respond to other frequencies. A system with a high Q resonates with greater amplitude (at the resonant frequency) than one with a low Q factor [28].)

A more realistic is that figure 2.3, where an additional capacitor C shunted across the terminal is added to account for the coil's self capacitance.

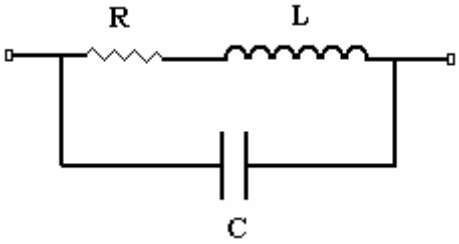

Figure 2.3 *High frequency equivalent circuit of an inductance coil*

The circuit of figure 2.3 belongs to the family of LCR resonance networks. For a simplified model of our coil as shown in figure 2.3, the coil self-resonance frequency, ω_{coil}, is [7, 14]:

$$\omega_{coil} = \sqrt{\frac{1}{LC} - (\frac{R}{L})^2} \qquad (2.12)$$

The coil self-resonance frequency should be slightly larger than the Larmor frequency of the MRI experiment so that the coil can be tuned (for example 400 MHz would be a desirable value for 300 MHz). If $(R^2C)/L<<1$, the corresponding quality factor is:

$$Q_{coil} = \omega_{coil}\frac{L}{R} = \frac{1}{R}\sqrt{\frac{L}{C}} \qquad (2.13)$$

As already discussed, to maximize SNR, the series resistance should be minimized (see equation 2.3). According to equation 2.13, this is equivalent to maximizing the Q-factor for a given inductance value. Therefore, the self-resonance frequency and the Q-factor of a coil are also a good indication of its potential performance as an NMR detector.

2.1.5 Susceptibility

In electrical engineering, the magnetic susceptibility is the degree of magnetization of a material in response to an applied magnetic field. The dimensionless volume magnetic susceptibility, represented by the symbol χ_v is defined by the $\mathrm{M}= \chi_v \mathrm{H}$, where M is the magnetization of the material (the magnetic dipole moment per unit volume), measured in amperes per meter, and H is the applied field, also measured in amperes per meter (From Wikipedia, the free encyclopedia).

For most materials, the magnetic susceptibility is in the ppm range. However, for large magnetic fields, the effect of local variations in χ_v cannot be ignored and results in undesired image artifacts in MRI experiments. The close proximity of the coil wires to most of the sample will adversely affect the spectral resolution. As was described by Webb [26], possible workarounds are the immersion of the coil in a material with susceptibility similar to that of the coil. In this way one mimics an infinite cylinder of given susceptibility in which the static field will be homogeneous. Alternatively the coil can be designed of multiple layers of different metals (*e.g.* aluminum and copper) with compensating susceptibilities.

2.2 Microcoil types

In this section we introduce 3 microcoil types which are commonly used in NMR experiments and then we compare their specifications.

2.2.1 Solenoid microcoils

The classical geometry to create a magnetic field with an electrical current is the solenoid coil or helix. Even for a limited number of windings this geometry provides a reasonable homogeneous B_1 field and a good filling factor is possible by winding the coil directly onto a holder containing the sample. Figure 2.4 shows an integrated solenoidal microcoil. Miniaturization to a scale of several hundred microns is not very difficult although the wire diameter (typically 20 to 50 micron) becomes very small and a freestanding coil is a very delicate object [30].
A reduction to below 100 micron diameter is possible but the machining and handling of such coils will be rather tedious. For this reason other microsystem fabrication technology such as bulk micromachining, LIGA and micro-injection molding should be applied [14].
For solenoid coils adding more turns to the coil will enhance the B_1/i ratio and thus both the inductance and the signal response. At the same time the coil resistance will increase linearly, so the improvement in sensitivity will be proportional to the square root of the number of turns (n). At the same time we will have a larger ohmic heating at the center of the coil and an enhanced danger for arcing, so the optimum is generally found for only a limited number of turns. Besides RF performance, static field distortions due to susceptibility effects are an important factor in the design of microcoil probeheads.

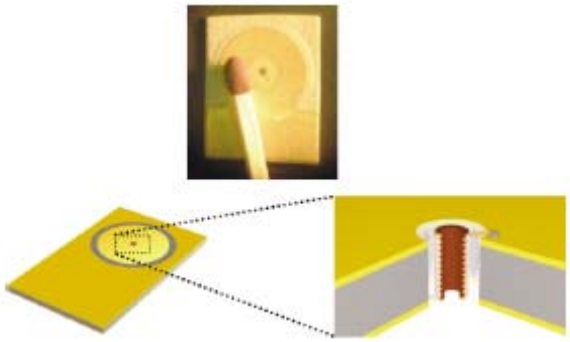

Figure 2.4 *Integrated solenoid microcoil and capacitor circuit. Top: actual photograph to indicate the size. The microcoil has a free inner diameter of 300 µm, located in the centre of the image. Bottom: schematic representation to illustrate the integrated design with the solenoid embedded in the centre of a tuned capacitor to provide an LC circuit with minimized losses [30].*

2.2.2 Planar microcoils

The most common geometry used in planar microcoils is based on a spiral design with the center winding contacted to the outside using a connection to another layer which is electrically isolated with a thin oxide layer. Figure 2.5 depicts a planar coil with the B_1 field intensity which is represented in a color map. The most commonly used sample position is indicated in the red rectangle with the RF field pointing in the axial direction. In this configuration the axis of the RF coil will be oriented perpendicular to the external static field B_0. An alternative orientation is indicated in yellow for a thin layer sample.

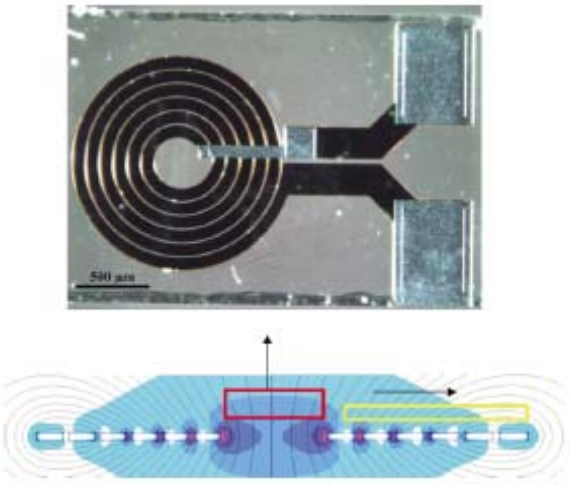

Figure 2.5 *Planar microcoil with 6 windings, inner diameter 300 µm, outer diameter 1.4 mm [31]*

Nevertheless, a detailed analysis shows that such a surface spiral has some serious drawbacks, compared to a helical coil. First, the outermost windings are much less efficient in the sense that they contribute less to the centre axial field while they largely dominate the resistive losses. Second, the fields produced by the outer windings cause considerable eddy currents in the centre windings adding additional losses and lowering the field homogeneity in the centre region. For this reason the optimum is found for only a few windings, and thus a rather low inductance [30, 32]. Figure 2.6 shows a micro-fabricated planar coil with a very tiny sample inside the coil.

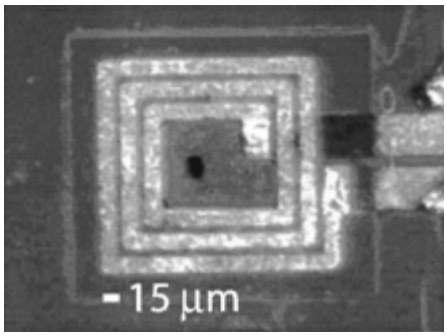

Figure 2.6 *Microscope photograph of the 100 mm microcoil. The black spot near the center of the microcoil is the sample used for the experiment [30]*

2.2.3 Saddle microcoils

The saddle coil (Figure 2.7) shows the most complex geometry of these three coil types. The B_1 field is generated primarily by the four vertical wire segments. Due to this coil geometry, the B_1 field of a saddle coil is more homogeneous in z direction than that of a planar coil. The saddle coil can be formed from wire, but it is also often etched from thin copper foil, which is then adhered to glass or PTFE tubing. The latter procedure leads to a high geometric precision, resulting in better B_1 homogeneity. The saddle coil is easily accessible and provides a good 'filling factor' of the usable area in the magnet bore. For these reasons it is widely used in NMR microscopy. However, these advantages are achieved at the price of decreased sensitivity. Compared to a saddle coil, the sensitivity performance of a solenoidal coil of the same dimensions is approximately three times better [12].

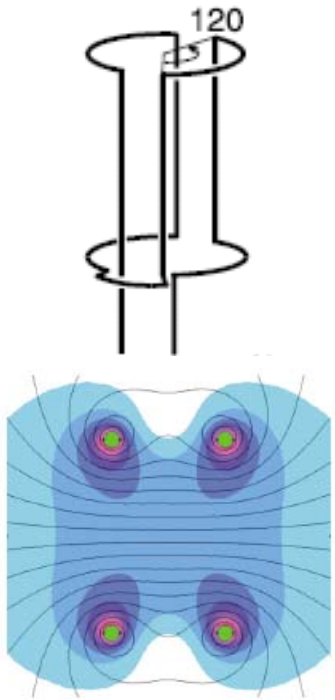

Figure 2.7 *Field profile for a typical saddle-coil [30]*

2.2.4 Comparison

Table 2.1 shows the specification of different coil types which have already been discussed. The micro solenoid and surface coil are actual probes that are experimentally verified, in this comparison. The other geometry is analyzed using finite element methods. Actual values for the sensitivity correspond to coil sizes that are not fully optimized and should be treated as typical values. The RF field B_1 is normalized to the number of turns to make the comparison more relevant. As expected, the solenoid gives reasonable field homogeneity, coupled with a good sensitivity if the windings are placed on a helix with optimized variable pitch. However, it lacks the possibility of sample heating [30].

Specifications	***Solenoid***	***Saddle coil***	***Planar coil***
No. of turns [n]	12	1	6
B_1/i.n [mT]	1.35	1.15	1.6
Relative sensitivity	1	0.35	0.57
B_1 homogeneity	+	0	–
Sample heating	–	0	–

Table 2.1 *Comparison of different coil geometries that contain the same amount of sample, in this case 50 nL.*

In this project, consequently, solenoidal coil geometry has been chosen for its superior magnetic field homogeneity.

2.3 Summary of coil design specifications

1) A micro-MR image requires a highly homogenous magnetic field within the region of interest. An inhomogenous magnetic field will lead to image artifacts due to the localized variations in spin precession frequency. Consequently, a solenoidal coil geometry should be chosen for its superior magnetic field homogeneity.
2) It is desirable that the chosen technology allows for compensation of susceptibility mismatches of the surrounding material. One way to achieve this is to combine different materials with positive and negative χ_v values to match the susceptibility of the sample or the surrounding material.
3) To achieve a high *SNR*, the signal from the sample has to be maximized by increasing the "filling factor". The coil dimensions therefore should be matched to the sample dimensions as closely possible. The coil volume is thus determined by the size of typical cell cultures of more than 10^3 individual cells, where a single cell has a typical diameter of 10 ~ 20 µm. Thus, the coil diameter should be in the range of at least ~100 µm.
4) Furthermore, noise has to be minimized. The major sources of ohmic loss are the resistance of the coil itself, and the wires connecting to the matching/tuning and amplification circuitry and losses due to eddy currents in the surrounding substrate. Also, dielectric losses are not negligible in case of biological, conducting samples and can only be minimized by integration of distributed capacitance. The ohmic losses minimization also leads to higher Q-factor of a coil.

Our efforts in this project, mostly concentrated on uniformity of magnetic field within the coil. Since, we focus on micro solenoidal coil the other objectives of the coil design, such as filling factor and high SNR, are fulfilled.

3 Electromagnetic simulation

For building a microcoil model and simulate its electromagnetic behavior as a RF receiver in MRI, we need to deal with a set of equations named after Maxwell and to solve them in an appropriate way. It should be mentioned that most practical problems in electromagnetics cannot be solved purely by means of analytical methods, e.g. radiation caused by a mobile phone near a human head, shielding of an electronic circuit by a slotted metallic box, etc. In many of such cases, numerical methods in electromagnetics can be applied in an efficient way to come to a satisfactory solution. In this chapter, we try to introduce the basics of electromagnetism in the frame of Maxwell's equation and then the numerical solution of these equations by means of Finite Element Method (FEM) will be discussed.

3.1 Maxwell's equations

In electromagnetics, Maxwell's equations are a set of four equations, developed by James Clerk Maxwell, that describe the behavior of both the elecrtic and magnetic fields, as well as their interactions with matter. Maxwell's four equations express respectively, how electric charges produce electric fields (Gauss' law), the experimental absence of magnetic monopoles, how currents and changing electric fields produce magnetic fields (the Ampere-Maxwell law), and how changing electric fields produce electric fields (Faraday's law of conduction). Table 3.1 describes these equations in both differential and integral forms.

Name	Differential form	Integral form
Gauss's law for electricity	$div\,.\vec{D} = \rho$	$\oiint_{\partial v} \vec{D}\,.d\,\vec{A} = \iiint_{v} \rho . d\vec{V}$
Gauss's law for magnetism	$div\,.\vec{B} = 0$	$\oiint_{\partial v} \vec{B}\,.d\,\vec{A} = 0$
Faraday's law of induction	$curl\ \vec{E} = -\frac{\partial}{\partial t}\vec{B}$	$\oint_{\partial A} \vec{E}\,.d\,\vec{s} = -\frac{\partial}{\partial t}\iint_{A} \vec{B}\,.d\,\vec{A}$
Ampère's law (with Maxwell's extension)	$curl\ \vec{H} = \vec{J} + \frac{\partial}{\partial t}\vec{D}$	$\oint_{\partial A} \vec{H}\,.d\,\vec{s} = \iint_{A} (\vec{J} + \frac{\partial}{\partial t}\vec{D}).d\,\vec{A}$

Table 3.1 *Maxwell's equations in differential and integtal forms, derived from ref. [34].*

Where $\vec{D}$ [C/m^2] denotes the electric displacement also called the electric flux density, $\vec{E}$ [v/m] is the electric field, $\vec{B}$[T or W/m^2] is the magnetic flux, the magnetic field is $\vec{H}$[A/m], $\vec{J}$ [A/m^2] is the current density and finally ρ[C/m^3] is free electric charge density.

Together with the material equations:

$$\vec{D} = \varepsilon . \vec{E} \qquad \vec{B} = \mu . \vec{H} \qquad \text{and} \quad \vec{J} = \kappa . \vec{E} \tag{3.1}$$

Maxwell's equations describe the behavior of the electromagnetic fields. ε, μ and κ hold the material properties. Usually, they are scalars which depend of course on the location and maybe on the field strength and the time.

Gauss' law for electricity is displayed (table 3.1) in integral form and in differential form. In integral form, it states that the electric flux out of any closed surface is proportional to the total charge enclosed within the surface. In differential form, the divergence of the electric flux density gives a measure of the source density. Gauss‘s law for magnetism is displayed (table 3.1) in integral form and in differential form. In integral form, it states that the net magnetic flux out of any closed surface is always equal to zero. As the divergence of a vector field is proportional to the source density, Gauss’s law for magnetism in differential form states that no free magnetic charges exist. Faraday's law of induction states (same table) that the line integral of the electric field around a closed loop is equal to the negative of the rate of change of the magnetic flux through the area enclosed by the loop. This line integral is equal to the generated voltage or electro-motive-force (emf) in the loop, so Faraday's law is the basis for electric generators. It also forms the basis for inductors and transformers. Finally, Ampère's law states (same table) that the line integral of the magnetic field around a closed loop is equal to the sum of a) the rate of change of the electric flux and b) the conduction and impressed current density through the area enclosed by the loop. More information about Maxwell's equations can be found in any course books of electromagnetic e.g. [36, 37].

3.2 Classes of electromagnetic problems

Electromagnetic fields can be classified into the following classes:

1) Static fields: Can be also classified into electrostatics and magnetostatics. In electrostatics the electric field is not time dependent, so $\frac{\partial}{\partial t}\vec{E} = 0$ (or curl $\vec{E}$ =0). From Faraday's law, this assumption implies the absence or near-absence of time-varying magnetic fields: $\frac{\partial}{\partial t}\vec{B} = 0$. In other words, electrostatics does not require the absence of magnetic fields or electric currents. Rather, if magnetic fields or electric currents *do* exist, they must not change with time, or in the worst-case, they must change with time only very slowly. In magnetostatics the magnetic fields are static. Magnetostatics is the study of static magnetic fields. In electrostatics, the charges are stationary, whereas here, the currents are stationary. As it turns out magnetostatics is a good approximation even when the currents are not static as long as the currents do not alternate rapidly. In this case, starting from Maxwell's equations, the following simplifications can be made: Ignore any electrostatic charge, ignore the electric field and presume the magnetic field is constant with respect to time. So this means that $\vec{E}$ = $\vec{D}$ =0, div $\vec{B}$=0 and finally, curl $\vec{H}$ = $\vec{J}$. The quality of this approximation may be guessed by comparing the above equations with the full version of Maxwell's equations (table 3.1) and considering the importance of the terms that have been removed. Of particular significance is the comparison of the $\vec{J}$ term against the $\partial \vec{D} / \partial t$ term. If the $\vec{J}$ term is substantially larger, then the smaller term may be ignored without significant loss of accuracy.

2) Time varying fields: The most general problem to investigate is an arbitrary dependency of the fields in time. Charges do not only produce electric fields. As charges

move, they generate magnetic fields (Ampère's law, see table 3.1) and if the magnetic field changes, it generates electric fields. This "secondary" electric field can be computed using Faraday's law of induction (See table 3.1). This means that a magnetic field changing in time produces a curled electric field, possibly also changing in time. The situation is no longer electrostatics, but rather electrodynamics.

In order to analyze the electromagnetic fields, there are two general approaches [34]:

a) High-frequency electromagnetic analysis: This type of analysis calculates the propagation properties of electromagnetic fields and waves in a given structure. High-frequency electromagnetic field analysis simulates the electromagnetic phenomena in a structure when the wavelength of the signal is of the same order of magnitude or smaller than the dimensions of the model. The high-frequency band ranges from hundreds of MHz to hundreds of GHz. In this case, the analysis can also classified into two following catagories: time-harmonic analysis and modal high-frequency analysis .

b) Low frequency electromagnetic analysis as a result of an electric current, a permanent magnet, or an applied external field. For low-frequency problems, or one can say quasi-static problems, the displacement current in Maxwell's equations is ignored ($\partial \vec{D} / \partial t$ =0). Therfore, charge accumulation and capacitance effects are excluded. This approach is valid when the working wavelength is much larger than the geometric dimensions of structure or the electromagnetic interactions are not obvious in the system. Otherwise, the full set of Maxwell's equations must be solved (high frequency analysis). In this category the different types of analysis can be followed: static magnetic analysis for analyzing magnetic fields caused by direct current (DC) or permanent magnets, harmonic magnetic analysis for analyzing magnetic fields caused by low frequency alternating current (AC) or voltage and finally transient magnetic analysis which analyze magnetic fields caused by arbitrary electric current or external field that varies over time. Some applications of low frequency electromagnetic analysis are in transformers, electric motors, magnetic imaging systems etc.

3. 3 Numerical solutions of Maxwell's equations

Maxwell's equations can be formulated as a hyperbolic system of partial differential equations. This gives access to powerful mathematical theories for the numerial solutions of hyperbolic PDE's. (It should be mentioned that the analytical solution of the Maxwell's equations can be applied only for a geometrically simple problem.) Computational electromagnetics, computational electrodynamics or electromagnetic modeling refers to the process of modeling the interaction of electromagnetic fields with physical objects and the environment, numerically. It typically involves using computationally efficient approximations to Maxwell's Equations and is used to calculate things such as antenna performance, electromagnetic compatibility, radar cross section and electromagnetic wave propagation when not in free space. There are several numerical methods for solving the electromagnetic problems such as Finite Element Method (FEM), Finite Integration Technique (FIT), etc. More information can be found in [34, 35].

However, here we only describe the principles of the Finite Element Method (FEM), which is the underlying procedure of ANSYS® (the software we used for simulation in this project).

3. 3. 1 Finite Element Method (FEM)

The FEM is generally used for finding approximate solution of partial differential equations (PDE) and also integral equations. The solution approach is based on rendering the PDE into an equivalent ordinary differential equation, which is then can be also solved using other standard techniques such as finite difference, etc. In solving partial PDE, the primary challenge is to create an equation which approximates the equation to be studied, but which is numerically stable, meaning that errors in the output data and intermediate calculations do not accumulate and cause the resulting output to be meaningless. The finite element method is a good choice for solving PDE over complex domains or when the desired precision varies over the entire domain. FEM is a mathematical method for solving PDE via a piecewise polynomial interpolation scheme. Put simply, FEM evaluates a differential equation curve by using a number of polynomial curves. Each polynomial in the solution can be represented by a number of points and so FEM evaluates the solution at the points only. A linear polynomial requires 2 points, while a quadratic requires 3. The points are known as node points or nodes.

To understand how FEM reduced the PDE to ordinary differential equation, let's start with a one dimensional case which all parameters in Maxwell's equations (Table 3.1) such as, $\vec{H}$, $\vec{B}$, $\vec{E}$ etc are the function of x and time (t). Substituting equation (3.1) into Faraday's law and Ampère's law, both in differential form (table 3.1), gives the determinate form of Maxwell's partial differential equations:

$$-\mu \frac{\partial}{\partial t} H = curl\,.E \qquad \text{or} \qquad -\mu \dot{H} = \nabla \times E \tag{3.2}$$

and $$\varepsilon \frac{\partial}{\partial t} E + \kappa E = curl\,.H \quad \text{or} \qquad \varepsilon \dot{E} + \kappa E = \nabla \times H \tag{3.3}$$

These assume that ε and μ vary with time slowly, if at all, in comparison to the fields themselves. For nonmagnetic materials permeability μ is essentially equal to its vacuum value, μ_0, everywhere.

H may be eliminated between the two curl equations in (3.2) and (3.3) and treated as a secondary or derived quantity. Taking the time derivative of equation (3.3), the curl of the (3.2), and eliminating the term with H gives the second order partial differential equation:

$$\varepsilon \ddot{E} + \kappa \dot{E} = \frac{1}{\mu} \nabla \times \nabla \times E \tag{3.4}$$

where the constant magnetic permeability is brought outside the curl operator. It should be noted for completeness that the vector fields in Faraday's and Ampère's law are ultimately caused by some distribution of electric charge, *ρ*, and current, *J*. This has been already shown from divergence conditions of Maxwell's equations (table 3.1):

$$\nabla .D = \rho \qquad \text{and} \qquad \nabla .B = 0$$

(These equations also can be derived from the principle of charge conservation.) The finite element formulation of initial-boundary value problems governed by time-dependent partial differential equations (PDEs), Maxwell's equations in particular, consists of the following formal steps:

1. Partition the problem's interior domain into a number of logically regular, contiguous sub-domains, i.e., the "model";
2. Represent the field over each sub-domain by a simplified basis function that interpolates between discrete field points or nodes;
3. Convert the point-wise partial differential operator to an equivalent but "weaker" scalar integral operator admitting lower order derivatives;
4. Evaluate the integral operator for the simplified field basis, giving an algebraic system of equations on the nodal field vector and its time derivatives;
5. Apply a radiation condition on the interior domain's boundary in order to simulate scattering into the infinite exterior domain.
6. Solve the system of ordinary differential equations (ODEs) in time using finite differences, modal analysis, etc.

The finite element part, from steps 1 to 4, yields an approximate integration of the PDE's spatial differential operator. Formal reduction of the point-wise partial differential equation to a finite element form may be accomplished in at least two ways, the method of weighted residuals (Galerkin's method) and a variation principle. They are fundamentally equivalent for symmetric differential operators provided that consistent assumptions are made, although the method of weighted residuals is more general.

The most difficult part of the finite element formulation of propagation-type problems is deriving an effective radiation or absorbing boundary condition. This is an approximate condition on the exterior boundary of the finite element model that discriminates between incident (illumination) and scattered radiation and selectively absorbs the scattered part, mimicking radiation into an infinite, nonreflecting exterior domain. An effective condition that is sufficient for simultaneous plane wave illumination and scattering is described in [41].

To apply the conventional finite element formalism to Maxwell's equations, it is convenient to start with the second order PDE on electric field, equation (3.4), rather than the original system of first order equations, (3.2) and (3.3). Strict solutions of this equation must possess at least second derivatives, however, it is impractical to require such from numerical approximations. A better approach is to rewrite the equation in an integral form admitting lower order derivatives. This is the so-called weak formulation.

To derive the weak form of equation (3.4) it is necessary to define another field over the wave domain, the so-called test function, $\boldsymbol{G}(\boldsymbol{x},t)$. This is a completely arbitrary function within wave domain Ω. Taking the inner (dot) product of (3.4) with $\boldsymbol{G}$ and integrating over Ω gives

$$\int_{\Omega} G.(\varepsilon \overset{\circ\circ}{E} + \kappa E)d\Omega = -\int_{\Omega} G.\frac{1}{\mu}\nabla\times\nabla\times E d\Omega \qquad (3.5)$$

Multiplication by a test function and integration reduces the point-wise vector equation to a volumetric scalar equation, named the weak form. It is easy to prove the assertion that if this integral equation is satisfied for any $\boldsymbol{G}$ then the PDE is necessarily satisfied at all points in the domain. The converse is certainly true, but if the PDE is not satisfied in some sub-

domain then a test function can be chosen that makes the integral nonzero, hence the assertion is true.

Consider the right-hand integrand in (3.5), after factoring μ. From the vector identity, $\nabla.(A \times B) = B.(\nabla \times A) - A.(\nabla \times B)$, this integrand can be written as

$$G.\nabla \times \nabla \times E = \nabla \times E.\nabla \times G - \nabla G \times \nabla \times E \tag{3.6}$$

Integrating and applying the divergence theorem to the second term gives

$$\int_{\Omega} G.\nabla \times \nabla \times E \, d\Omega = \int_{\Omega} \nabla \times E.\nabla \times G \, d\Omega + \int_{\Sigma} G.n \times \nabla \times E \, d\Sigma \tag{3.7}$$

In the surface integral, ***n*** is the outward unit normal to Σ and the integrand has been rearranged according to the rule for scalar triple products. This identity is the vector analog of Green's identity and is simply the result of multi-dimensional integration by parts. Substituting (3.7) into (3.5), the volume-averaged scalar equation becomes

$$\int_{\Omega} G.(\varepsilon \overset{\circ\circ}{E} + \kappa \overset{\circ}{E}) d\Omega = -\frac{1}{\mu}\int_{\Omega} \nabla \times E.\nabla \times G \, d\Omega - \frac{1}{\mu}\int_{\Sigma} G.n \times \nabla \times E \, d\Sigma \tag{3.8}$$

The critical result expressed in (3.8) is that the volume integral of the second order spatial operator has been replaced by "weaker" volume and surface integrals of first order operators.

Next step is the reduction to ordinary differential equation (ODE). The basis for transforming the volumetric partial differential equation to an ordinary differential equation is an assumption on the mathematical form of wave fields in domain Ω. In particular, fields are assumed to be separable in space and time, namely,

$$E(\mathbf{x},t)=S(\mathbf{x}).\boldsymbol{f}(t), \qquad G(\mathbf{x},t)=S(\mathbf{x}).\boldsymbol{g}(t) \tag{3.9}$$

Where ***x*** is the position vector, matrix *S*(***x***) represents the field's spatial variation, and vector ***f***(*t*) or ***g***(*t*) represents the time variation. Note, that the same spatial variation is assumed for E and G in (3.9). This assumption, associated with the name of Galerkin in the finite element literature, is particularly convenient because it yields a symmetric system of equations. Substituting separable solutions (3.9) into the integrands in (3.8) finally leads to an ordinary differential equation.

$$M \overset{\circ\circ}{\xi} + C \overset{\circ}{\xi} = (K + B)\xi \tag{3.10}$$

This is the global ordinary differential equation equivalent to Maxwell's partial differential equations in Ω. Of course, the utility of (3.10) depends on the choice of separable field representation, i.e., *S*(***x***) and ***f***(*t*). Where

$$M = \int_{\Omega} S^T \varepsilon S \, d\Omega \quad , \quad C = \int_{\Omega} S^T \kappa S \, d\Omega \quad , \; K = \frac{1}{\mu}\int_{\Omega} (\nabla \times S)^T (\nabla \times S) \, d\Omega$$

are symmetric coefficient matrices defined by the volume integrals and

$$B = \frac{1}{\mu}\int_{\Sigma} S^T n \times \nabla \times S \, d\Sigma$$

More information can be found in [39, 41]. Given the above mathematical preamble, the finite element procedure consists of partitioning or discretizing interior domain Ω into a number of sub-domains or finite elements. The field is approximated over each element by an interpolating or shape function depending on values at discrete nodes on or in the element. This yields a convenient local basis (in contrast to a global basis) for evaluating the model's matrix coefficients in equation (3.10) using an element-by-element summation.

3.3.2 ANSYS®

ANSYS® is the original (and commonly used) name for a Multiphysics, general-purpose finite element analysis software. ANSYS® Multiphysics are self contained analysis tools incorporating pre-processing (geometry creation, meshing), solver and post processing modules in a unified graphical user interface. Figure 3.1 shows the flowchart for finite element analysis using this software. ANSYS® is a general purpose finite element modeling package for numerically solving a wide variety of problems. These problems include: static and dynamic structural analysis (both linear and non-linear), heat transfer and fluid problems, as well as acoustic and electro-magnetic problems. The ANSYS Multiphysics software is a general-purpose analysis tool allowing a user to combine the effects of two or more different yet interrelated physics, within one unified simulation environment.

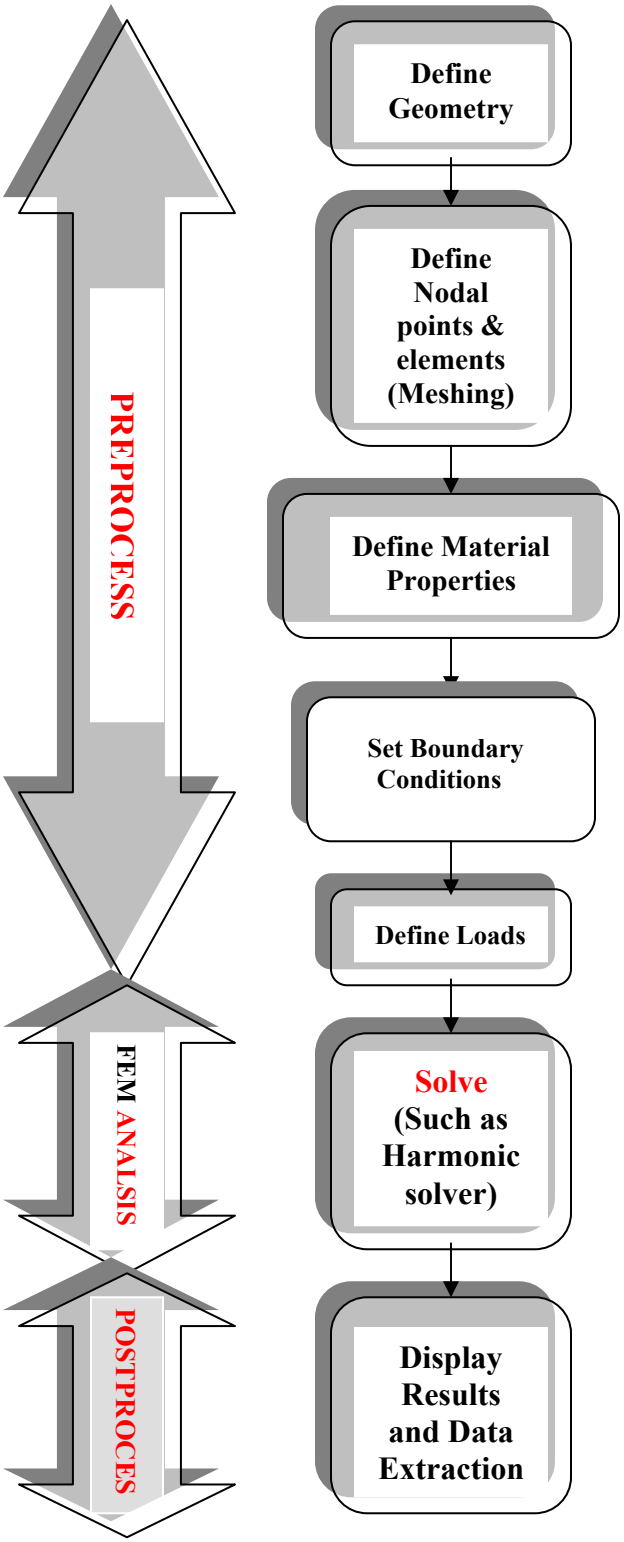

Figure 3. 1 *Flowchart for FEM analysis using ANSYS®*

4 Modeling and simulation

Now, we come to the coil simulation using Finite Element Method with the simulation tool ANSYS. As shown in figure 3.1, the task sequence in an ANSYS simulation has some main parts which are essentially the same no matter how your simulation project looks like:

1. Geometry modeling
2. Setting up material properties (such as permeability, …..)
3. Meshing
    - Selecting finite elements that suit the needs (from a predefined library)
    - Defining the element density (May change significantly in regions, some regions high some regions probably low)

4. Application of loads and degrees of freedom. Deciding what forces act on which nodes and what boundary conditions have to be fullfiled.
5. Numerical solving: This gives us the solution for every nodes or elements (discrete!)
6. Postprocessing: Visualization of element solution and data export.

In this chapter, we try to follow this guidelines and demostrate the results of microcoil simulation for a given geometry**.**

4.1 The coil geometry and the matrerial properties

A new microcoil for micro-MRI cell imaging has been recently designed (at IMTEK, Freiburg) and fabricated (in Japan) by Mona Klein [14] (See Figure 4.1). Simulation geometries in ANSYS was created based on the Mona Klein's fabricated coil geometry. Figure 4.2 shows the sketch of simulation microcoil geometry with 8 turns, which was created for the ANSYS simulation. Parameters S_1, S_2, S_3, S_4 are the turn's inner radios. P_1, P_2, P_3 and P_4 are the turn's spacing. R_1, R_2, R_3, R_4 stand for length of the coil's cross sections and H_1, H_2, H_3 and H_4 are the width of the coil cross sections. In simulation, the following dimensions were considered for the parameters:

$$P_1 = 20\ \mu m,\ P_2 = 40\ \mu m,\ P_3 = 40\ \mu m,\ P_4 = 40\ \mu m$$
$$S_1 = 80\ \mu m,\ S_2 = 80\ \mu m,\ S_3 = 80\ \mu m,\ S_4 = 80\ \mu m$$
$$R_1 = 20\ \mu m,\ R_2 = 20\ \mu m,\ R_3 = 20\ \mu m,\ R_4 = 20\ \mu m$$
$$H_1 = 20\ \mu m,\ H_2 = 20\ \mu m,\ H_3 = 20\ \mu m,\ H_4 = 20\ \mu m$$

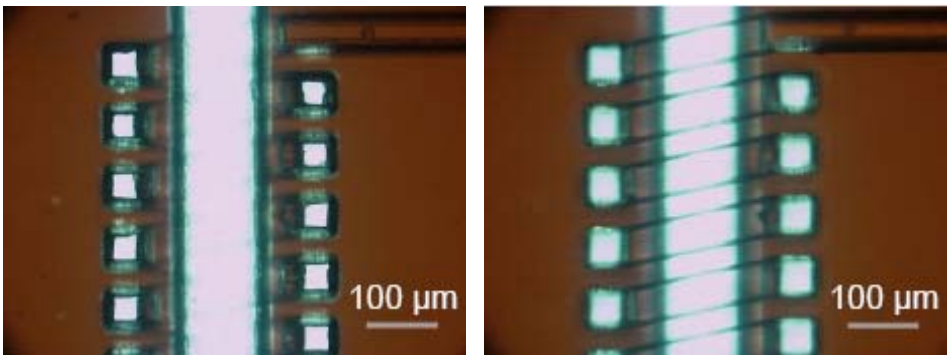

Figure 4.1 *Fabricated Coil pattern [14]*

It is comon practice in FEM simulation to look for any kind of symmetry which could be used to subdivide the simulation domain without any loss of accuracy.

Since, the coil is symmetric in both x and y axis (see figure 4.2), the overall shape can be reduced to one quarter, in simulation. This approach save simulation time and also the memory. Therefore, The following 2-dimensional axis-symmetrical model was created (Figure 4.2).

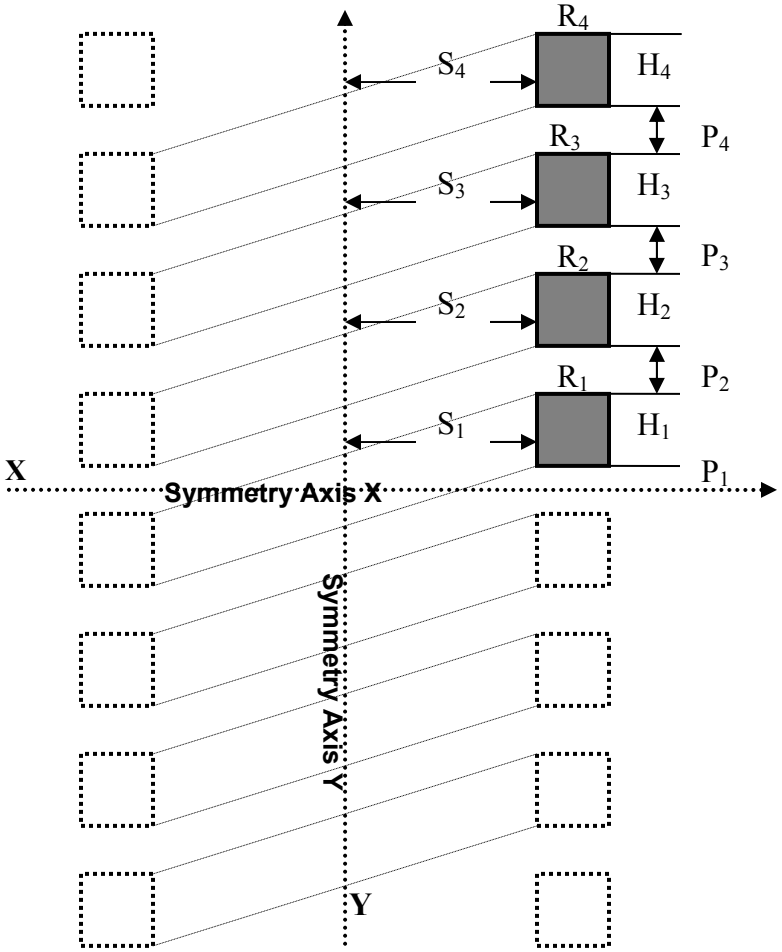

Figure 4.2 *Sketch of Simulation microcoil geometry*

The coil, as a conductor, was considered to be made from Copper with relative permeability (μ_r =1) and resistivity, ρ, equal to 16.78 nΩ.m. The linear material properties will be an acceptable approach if the temperature considered to be almost constant (in the range of room temperature). The medium around the coductor was cosidered as air with μ_r equal to 1.

4.2 Meshing and element types

The ANSYS program has a large library of element types. PLANE53 models 2-D (planar and axis-symmetric) magnetic fields. This element is defined by 8 nodes and has up to 4 degrees of freedom per node: z component of the magnetic vector potential (AZ), time-integrated electric scalar potential (VOLT), electric current (CURR), and electromotive force (EMF). PLANE53 is based on the magnetic vector potential formulation and is applicable to the low-frequency magnetic field analysis such as eddy currents (AC time harmonic and transient analyses), voltage forced magnetic fields (static, AC time harmonic and transient

analysis) etc [38]. PLANE53 element type was chosen for the conductor and its surrounding air medium, in this project.

Because it is not possible to discretize an infinite space, we must think about, hoe to deal with the boundaries of our calculation domain. The behavior of the interesting field has to be treated as if it could penetrate the space outside the calculation domain without recognizing the boundary plane. This is called "open boundary" and can be handled by the solvers.

In ANSYS, INFIN110 element type is used to model an open boundary of a 2-D unbounded field problem. A single layer of elements is used to represent an exterior sub-domain of semi-infinite extent. This element has 2-D (planar and axis-symmetric) magnetic potential capability. The element is defined by either 4 or 8 nodes with a single degree of freedom (in our case AZ) at each node [38]. In this project, INFIN110 was chosen for far field in order to model an open boundary condition.

The boundary conditions can also be used to model symmetries: if the geometry shows symmetry to a certain plane or axis, the fields will either be tangential or normal to this particular plane or axis. In this case, it is enough to discretize only one half of the geometry and the boundary condition at this plane or axis can be used to force the fields to behave like the whole geometry. As an example, In order to fulfill this fact in our model, magnetic vector potential (AZ) equal to zero was applied (at X=0).

.

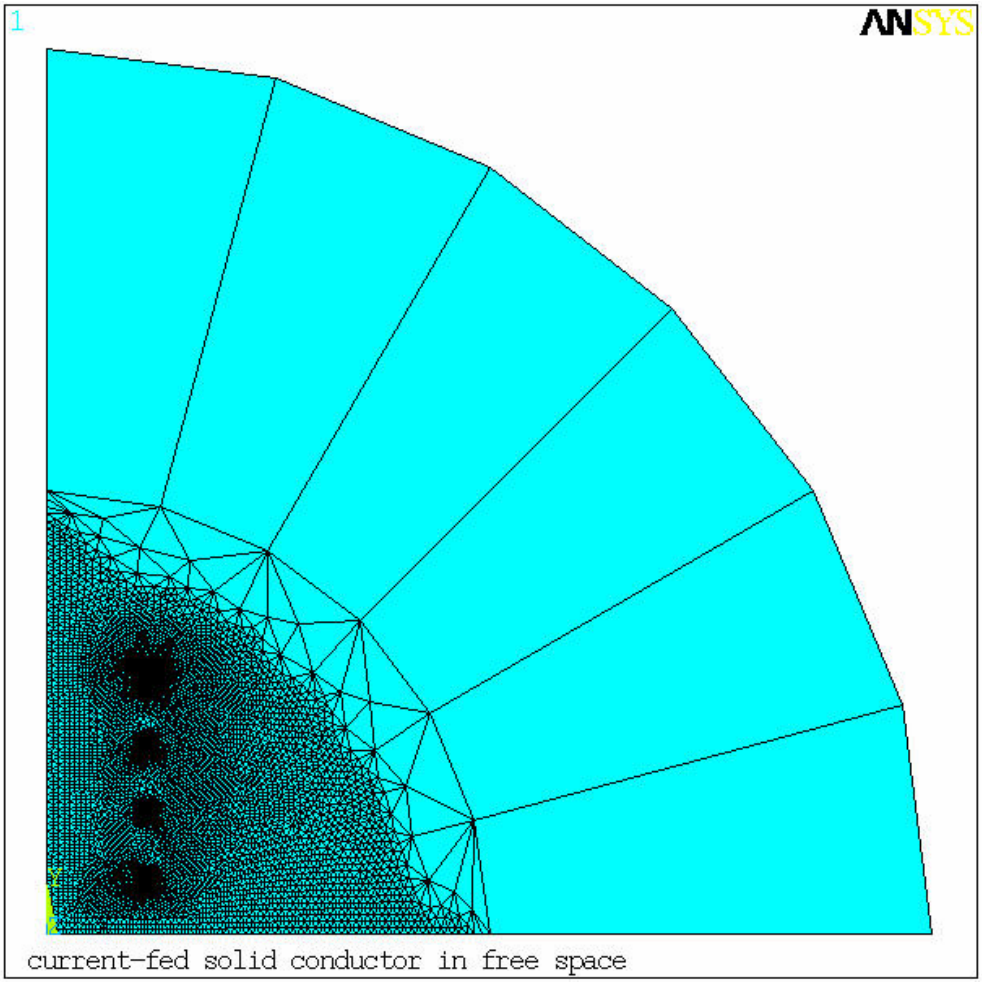

Figure 4.3 *shows the meshing of different areas of the geometry*

Sometimes it is normal to make non-uniform meshing in whole computational domain. Since some domains probably are regions of interest (ROI), fine meshing in ROI would be necessary. Therefore, Fine meshing in and also around the conductor were applied in order to visualize skin and proximity effect inside the coil and also to minimize the discretization error within the coil. Figure 4.3 shows the area-meshed FE model.

4.3 The load

After having defined the simulation geometry along with the material properties and having defined the finite element mesh along with the boundary conditions, we have to define the loads.

An alternative current (υ= 300 MHz) was applied in a solid conductor (total current = 1e-12). Furthermore, a coupled time-integrated electric scalar potential (VOLT) were applied into each set of coil turns. Coupling degrees of freedom into a set causes the results calculated for one member of the set to be the same for all members of the set.

4. 4 Solving

It has been already discussed in section 3.2 that low frequency analysis is valid when the working wavelength is much larger than the geometric dimensions of structure. Since, for an MR experiment conducted at 7 T, υ= 300 MHz, the corresponding wavelength is 1 m and our coil size is in the micrometer range, so one can easily say that the low frequency analysis can be applied for microcoil simulation. But it should be noted that for low-frequency problems, or quasi-static problems, the displacement current in Maxwell's equations is ignored ($\partial \vec{D} / \partial t$ =0). Therfore, charge accumulation and capacitance effects are not included. In this category harmonic magnetic analysis is applied for analyzing magnetic fields caused by alternating current (AC) or voltage. For a 2-D harmonic problem, solution is found by solving the Maxwell equation through the magnetic vector potential formalism.

(In harmonic analyses, the excitation and DOF response are assumed to be sinusoidal at a given constant frequency $f=\Omega/2\pi$ although each location may have different displacement amplitude u_o and phase angle φ. Using complex notation, the displacements can be expanded as follows:

$$u = u_0 e^{i(\Omega t+\varphi)} = u_0 e^{i\varphi} e^{i\Omega t} = (u_1 + iu_2) e^{i\Omega t} \qquad (4.1)$$

Substitution of the above into the linear equations of motion yields the following:

$$M \overset{\circ\circ}{u} + C \overset{\circ}{u} + Ku = F$$

Where M, C and K are system matrices, u is the degree of freedom and F is load [42]).

So, ANSYS harmonic response analysis was performed and sparse direct solver was chosen**.** The sparse direct solver is based on a direct elimination of equations as opposed to iterative solvers, where the solution is obtained through indirect means (that is, through iterative solution). Since the sparse direct solver is based on direct elimination, poorly conditioned matrices do not pose any difficulty in producing a solution. This method is recommended when robustness and solution speed are required (nonlinear analysis); for linear analysis where iterative solvers are slow to converge (especially for ill-conditioned matrices, such as poorly shaped elements).

4.5 Post processing

After building the model and obtaining the solution, we want to answer this question: How does the magnetic field flow within the coil's turns? To answer, we should perform post processing. Post processing means reviewing the results of an analysis. It is probably the most important step in the analysis, because one is trying to understand how the applied loads affect the design, how good the finite element mesh is, and so on. In ANSYS, two postprocessors are available to review the results: POST1, the general postprocessor, and POST26, the time-history postprocessor. Via the post processor of ANSYS, it is possible to plot or visualize the results. Figure 4.4 shows the current density distribution in the conductors (coil's turns) at 300 MHz. As figure shows, the current has been accumulated on the external surface of the conductor (skin effect) and also the distribution of current within the conductor is asymmetric (proximity effect).

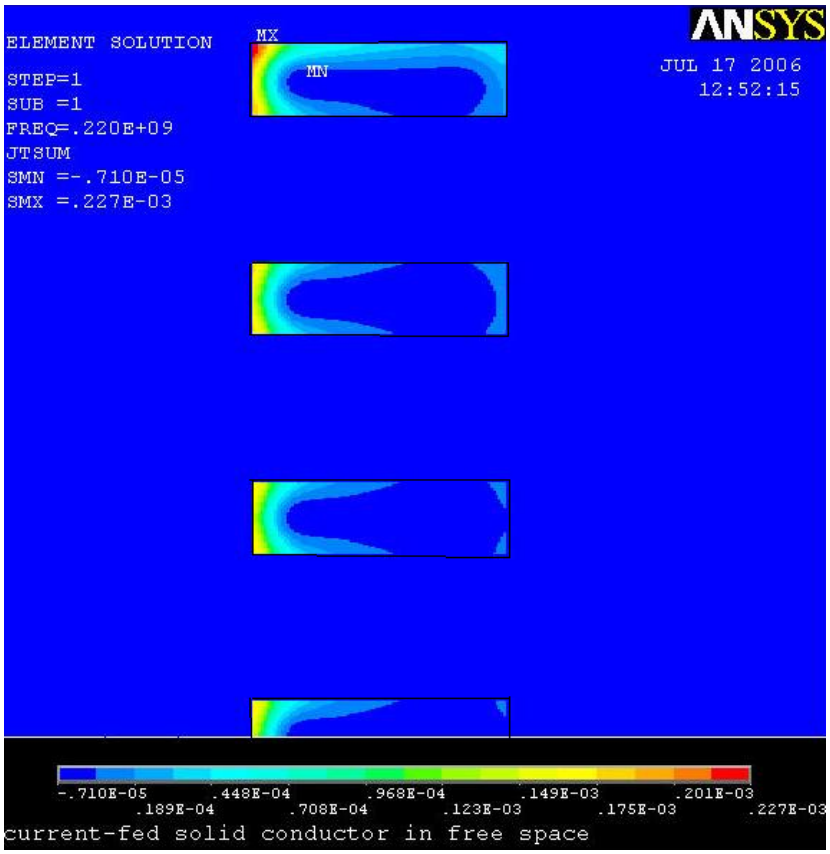

Figure 4.4 *the current density distribution in the conductors (coil's turns with dimentions width=20 μm and length= 60 μm)*

As already mentioned, our goal is to define the magnetic field distribution. Furthermore, in this project, we focus on magnetic field homogeneity within the coil. But, the question arises: which parameter can be considered as criteria for the field homogeneity?

To answer this question, now we try to derive and introduce an objective function as a field homogeneity criterion.

We know from statistics that standard deviation, σ, is the most common measure of statistical dispersion, measuring how spread out the values in a data set. If the data points

are all close to the mean, then the standard deviation is close to zero. If many data points are far from the mean, then the σ is far from zero and finally if all the data values are equal, then the standard deviation is zero. The standard deviation is the root mean square (RMS) deviation of the values from their arithmetic mean. Thus, we consider the following value as an objective function for measuring field homogeneity within the coil:

$$obj = \frac{\sigma}{\bar{H}} \times 100 \qquad (4.\ 2)$$

which *σ is the standard deviation of the magnetic field and $\bar{H}$ is the magnetic field mean value within the coil.* This function shows that, in our ROI, how the fields are spread out around the field mean value in percent.

First of all, we should define our region of interest to measure the field and its dispersion. The aim of this project is to design a receiver coil for MR-cell imaging. The cell is located inside the tube which is surrounded by the coil turns in order to increase filling factor. Figure 4.5 depicts the place where the cell should be located in. One can consider this area as 80 % of the whole area inside the coil. We call this area as our ROI.

Therefore, in post processing we should be able to collect the field distribution data in the ROI. Then, we should add the commands to ANSYA program how to calculate the field-mean value and the standard deviation and finally return the objective function (equation 4.2) in this area. In next section, we derive a formula for calculation of σ and $\bar{H}$.

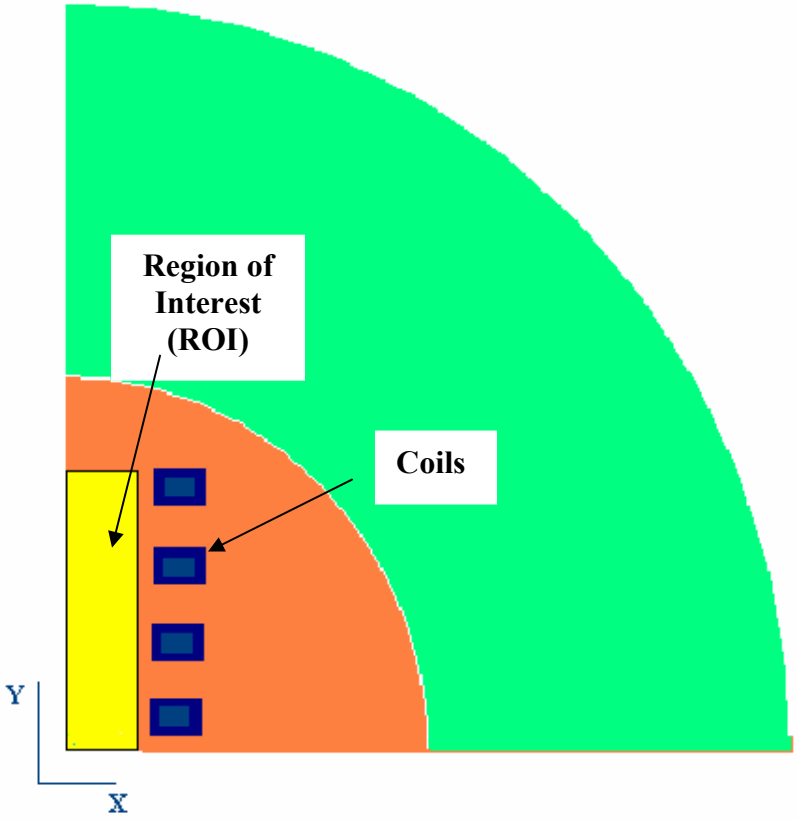

***Figure 4.5** depicts the our region of interest within the coil*

Figure 4.6 and 4.7 show the magnetic field in our ROI. Since the magnetic field, which is calculated by harmonic analysis, is a complex value, we try to figure out the real part (figure 4.6) and the imaginary part (figure 4.7) in our ROI separately. In comparison, the

magnitudes of real part are 2 orders of magnitude higher than the imaginary part. Furthermore, the imaginary response contains much higher magnetic field inhomogeneity, or one can say dispersion, in comparison to real response. Even, some imaginary values are negative and thus the vectors have negative directions, too (figure 4.7). This means that a big phase shift can be observable in ROI.

Finally, we try to depict the amplitude of magnetic field (calculated by the square root of the sum of the squared values of both real and imaginary part) in figure 4.8. The magnetic field intensity distribution with different colors shows dispersion from maximum value (1.6x 10^{-8} A/m) to minimum value (9.0x10^{-9} A/m).

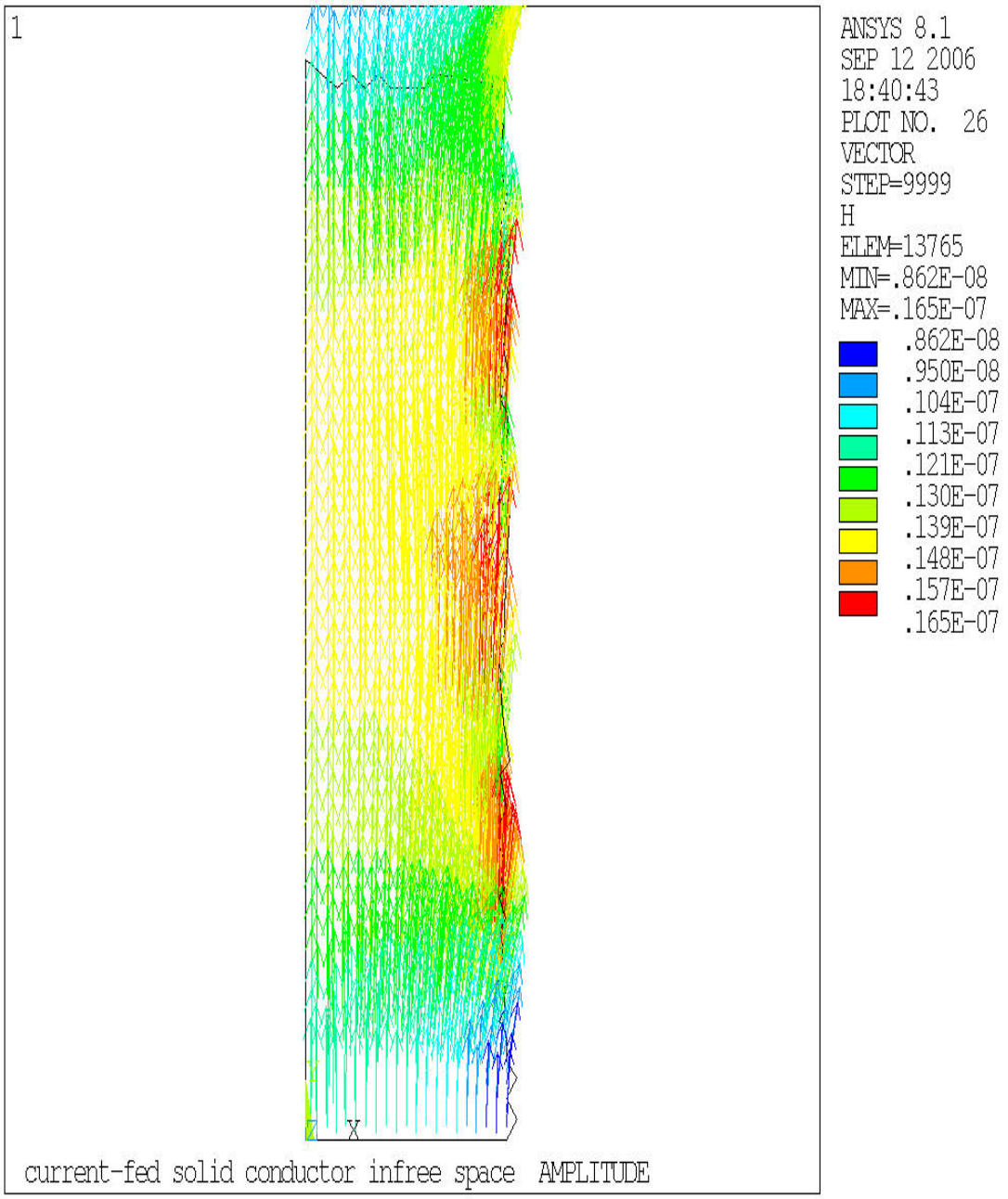

Figure 4.6 *Magnetic field distribution in ROI (real part)*

4.5.1 Calculation of magnetic field mean value

Since the size of the elements inside the ROI are not constant and their values vary in respect to different mesh size in different locations, the magnetic field intensity should be normalized over the element sizes. Thus, the magnetic field mean value can be calculated as:

$$\overline{H} = \frac{\sum_i H_i * A_i}{\sum_i A_i} \tag{4.3}$$

Where H_i is the magnetic field in element i. A_i is the area of element i and symbol Σ shows the summation over all the elements.

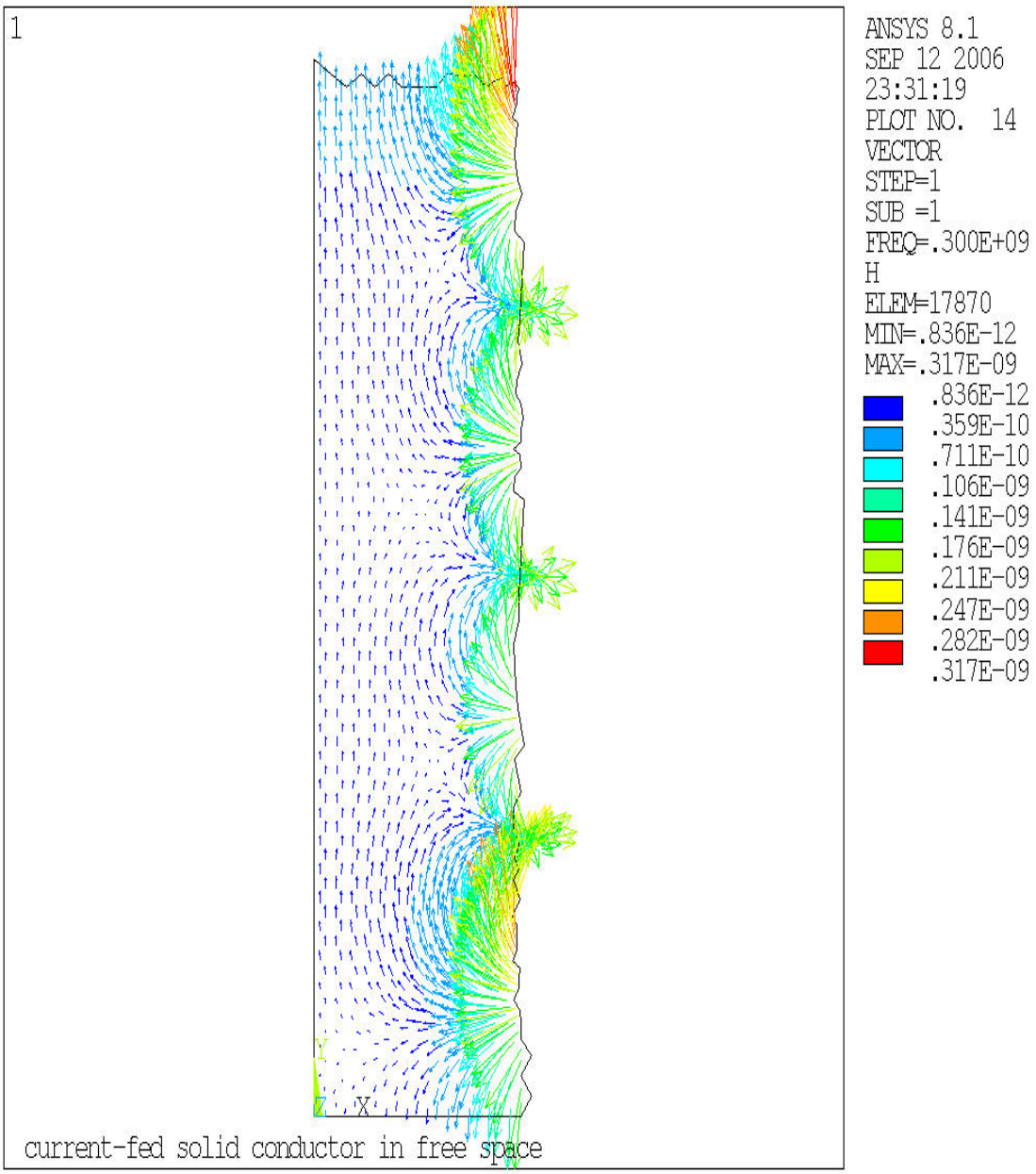

Figure 4.7 *Magnetic field distribution in ROI (imaginary part)*

4.5.2 Calculation of magnetic field standard deviation in ROI

The variance of magnetic field can be defined as:

$$\sigma^2 = \frac{\sum_i (H_i - \bar{H}_i)^2 A_i}{\sum_i A_i} = \frac{\sum_i \left\{ H_i^{\,2} * A_i - 2H_i * \bar{H}_i * A_i + \bar{H}_i^{\,2} * A_i \right\}}{\sum_i A_i} \qquad (4.4)$$

by rearranging the equation 4.4 and subsituation of equation 4.3 in 4.4, one can easily derive the following equaition:

$$\sigma^2 = \frac{\sum_i H_i^{\,2} * A_i - \bar{H}_i^{\,2} \sum_i A_i}{\sum_i A_i} \qquad (4.5)$$

and finally standard devaition is the root of variance:

$$\sigma = \sqrt{\frac{\sum_i H_i^{\,2} * A_i - \bar{H}_i^{\,2} \sum_i A_i}{\sum_i A_i}} \qquad (4.6)$$

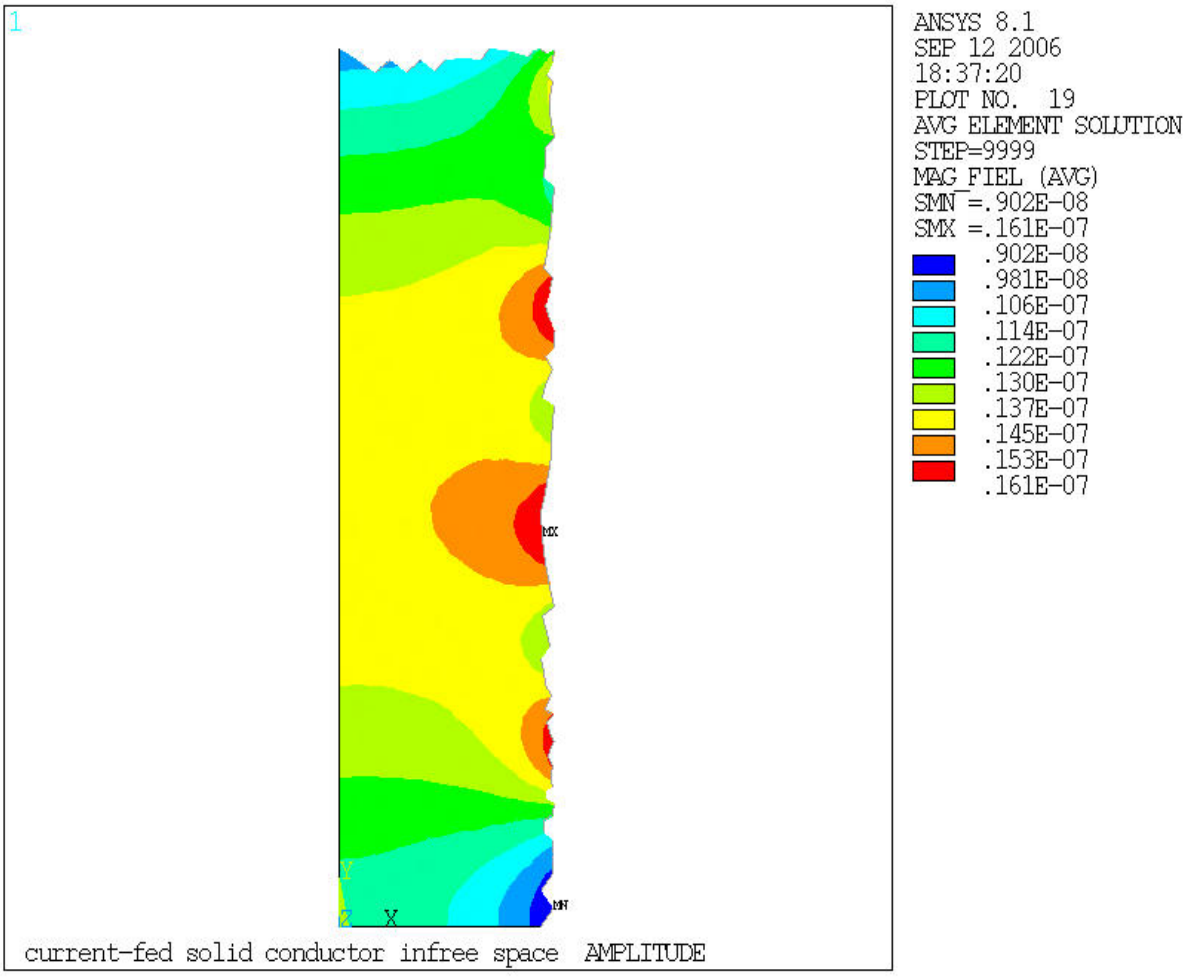

Figure 4.8 *Magnetic field distribution in ROI (Amplitude)*

4.5.3 Objective function in ROI

We consider following value as an objective function for measuring field homogeneity within the coil (as already discussed in section 4.5):

$$obj = \frac{\sigma}{\overline{H}} \times 100$$

which *σ is the standard deviation of the magnetic field and* $\overline{H}$ *is the magnetic field mean value within the coil.* Now is the time to calculate the objective function in our region of interest. This value is a criterion for field homogeneity in this region. Table 4.1 shows the final results:

	Imaginary part (%)	**Real part (%)**	**Amplitude (%)**
Obj. function	**304.8**	**9.6**	**9.6**

Table 4.1 *the final results for a field homogeneity criterion*

Since imaginary part of magnetic field response is 2-3 order of magnitude smaller than the real one (already discussed), the objective function for amplitude returns the same value of the real part. The final result shows that this geometry probably is not the optimum design and we should try to decrease inhomogeneity by means of shape optimization.

For shape optimization we can change the dimentions of all the parameters in coil, for instanse, coil spacing (P_1 to P_4), inner radios of coil turns (S_1 to S_4), coil width (H_1 to H_4) and finally the coil length (R_1 to R_4). See figure 4.2.

Figure 4.8 a) to e) depicts the standard shape and the possible shape optimization approaches to optimize the coil design, in respect to field uniformity within the coil.

In the next chapter we introduce optimization theory and try to implement this theory to design an optimum-shaped microcoil.

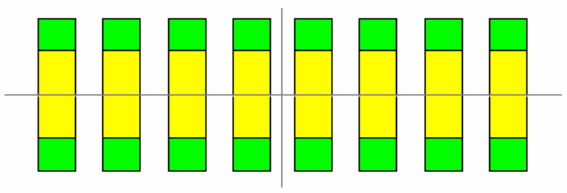

a) Standard design

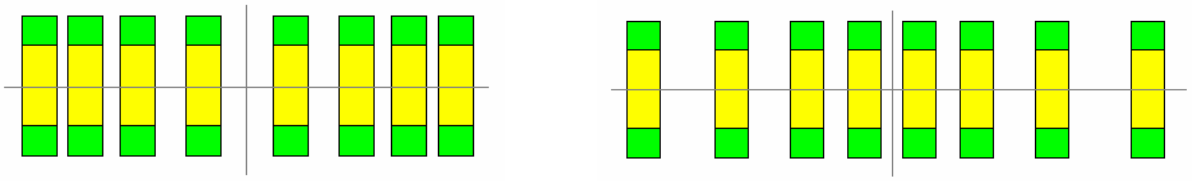

b) Different spacing between turns of the coil from high to low (left) or low to high (right)

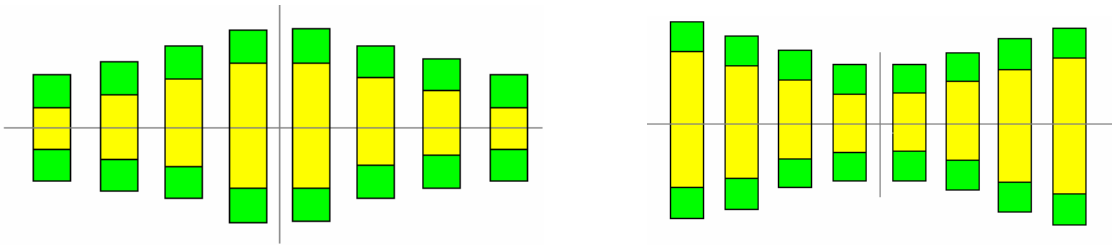

c) Different coil inner radios form high to low (left) or low to high (right)

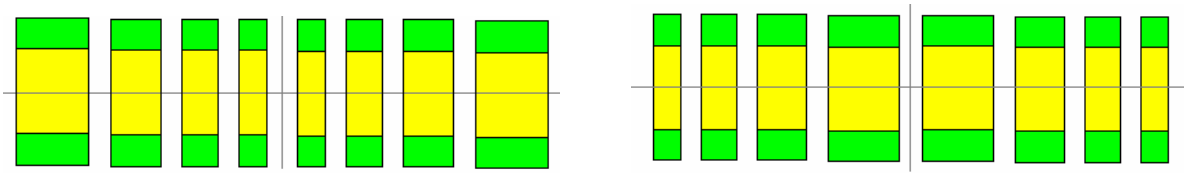

d) Different coil turns length form low to high (left) or high to low (right)

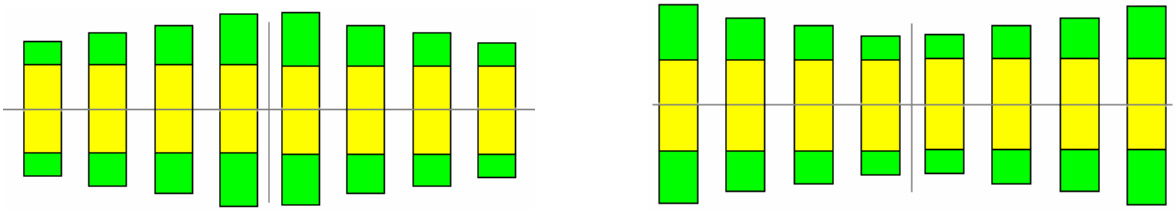

e) Different coil turns width form high to low (left) or low to high (right)

Figure 4.8 a) to e) The standard shape and the possible redesigned shape of microcoil in order to overcome field inhomogeneity (green: conductor, yellow: ROI for magnetic field studies)

5 Optimization

The concept of optimization is basic to what we do in our daily life: a desire to do better or be the best in one field or another. In engineering we wish to produce the best possible result with the available resources. In a highly competitive modern world it is no longer sufficient to design a system whose performance of the required task is just satisfactory. It is essential to design the best system. Thus in "designing" new products in any field: aerospace, automotive, chemical, electrical, biomedical, agricultural, etc, we must use design tools which provide the desired results in a timely and economical fashion. Numerical optimization is one of the tools at our disposal. In general, there are two fundamentally different types of optimization. The first is referred to as design optimization. The second is known as topological optimization. The goal of topological optimization is to find the best use of material for a body such that an objective criterion takes out a maximum (or minimum) value subject to given constraints [38]. In this chapter, we introduce the optimization theory and then try to implement this theory to optimize the microcoil geometry using the DOT software.

5.1 Basic concepts of optimization

Most of the design task in engineering is quantifiable, and so we are able to use computers to analyze alternative designs efficiently. The purpose of numerical optimization is to aid us in rationally searching among alternative designs for the best design to meet our needs.

The alternative designs of the same system differ from each other because some parameters of the system are not the same. The parameters that could be changed in the system while searching for the best design are called design variables. Although we may not always think of it this way, design process may be defined as the process of finding the minimum or maximum of some characteristic, which may be called the objective function. For the design to be acceptable it must also satisfy certain requirements. These requirements are called design constraints. Optimization automatically changes the design variables to help us find the minimum or maximum of the objective function, while satisfying all the required design constraints.

In the most general sense, numerical optimization solves the nonlinear, constrained problem; find the set of design variables, X_i, i=1, N, contained in vector X, that will

$$\textbf{Minimize (or Maximize) } F(X) \tag{5.1}$$

Subject to:

$$g_j(X) \leq 0 \qquad j = 1, M \tag{5.2}$$

$$h_k(X) = 0 \qquad k = 1, L \tag{5.3}$$

$$X_i^L \leq X_i \leq X_i^U \qquad i = 1, N \tag{5.4}$$

Equation 5.1 defines the objective function which depends on the values of the design variables, X. Equations 5.2 and 5.3 are inequality and equality constraints respectively, and equation 5.4 defines the region of search for the minimum. The bounds defined by equation 5.4 are referred to as side constraints [44]. In general, there are two kinds of optimization

problems, unconstrained and constrained. The above equations show a constrained problem with the set of constrained 5.2 and 5.3. Here a problem is defined as unconstrained if the set of constraints does not exist. In this case, lower and upper bounds (equation 5.4) can be imposed on the design variables, and these bounds will be respected. To understand how the optimization theory works out, let us start with a simple physical problem.

Figure 5.1 *A simple physical problem [43]*

Consider the example in figure 5.1**.** One boy bets that he can locate the top of the hill while blindfolded. The other boy agrees but asks the first boy to also stay inside the fences. Translating this situation into optimization problem formulation, we see that the objective is to find the highest point on the hill. Therefore, objective function is the height achieved by the first boy with respect to his original position. The design variables are longitude and latitude – the coordinates, defining position of the boy. The constraints are that the boy has to stay inside the fences. Note here, that in general, the boy may start the search from outside the fences. It is possible to define this physical problem mathematically, thus converting it to the engineering problem. Optimization is a very simple extension of the engineering problem:

Maximize: $Y = f(x_1, x_2)$ (objective)

Subject to: $F_1 = f_1(x_1, x_2) \le 0$, $F_2 = f_2(x_1, x_2) \le 0$ (constraints)

$x = \begin{Bmatrix} x_1 \\ x_2 \end{Bmatrix}$ (design variables)

Recall, that optimization automatically changes the design variables to helps us find the minimum or maximum of the objective function, while satisfying all the required constraints. The optimization process is illustrated in Figure 5.2.

Since the boy is blindfolded so he can't see the highest point on the hill that is inside the fences. He must somehow search for this point. One approach would be to take a small step in the north-south direction and another in the east-west direction and from that estimate the slope of the hill (assuming he is well inside of the fences). What he has done is to calculate the gradient of the objective function. This is a vector direction. The slope is the direction he

might chose to search since this will move he up the hill at the fastest rate. This we call the search direction.

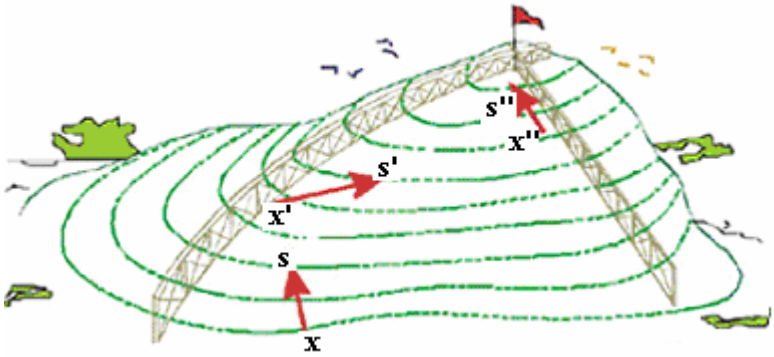

Figure 5.2 *The optimization process [43]*

Note that the number of steps he takes in this direction is a scalar parameter. We will call the number of steps in a given search direction α. Now we define the point at which he started as X. In this case, X contains two entries, being the longitude and latitude of his starting point. Suppose that he choose to move straight up hill. He moved in a vector search direction we will call S (See figure 5.2). Also, this is the first iteration in the process of maximizing his elevation so it is iteration no. 1. Since this is the first iteration, the direction he moves is designated as S^1. Upon encountering a fence or the crest of the hill in direction S^1, we can update the description of his location on the hill by the simple mathematical expression:

$$X^q = X^{q-1} + \alpha S^{q-1} \qquad (5.5)$$

Which, q is the iteration number. If he is not at the crest of the hill, he could just repeat the process of finding a new direction and moving again.

So, the process may be broken down into the following steps:

- Find a search direction that will improve the objective while staying inside the fences;
- Search in this direction until no more improvement can be made by going in this direction;
- Repeat the process, until no search direction can be found that improves the objective.

The optimization problem formulation and the optimization process presented above are very general and can be applied to any design problem.

No doubt that optimization is useful. It has been successfully working for many years. Optimization is the most powerful design improvement tool that is available today.

The overall optimization process now proceeds in the following steps:

1. Start q=0, X=X^0
2. q= q+1
3. Evaluate $F(X^{q-1})$
4. Calculate gradient of $F(X^{q-1})$
5. Determine a search direction, S^q
6. Perform a one-dimensional search to find $\boldsymbol{\alpha}$

7. Set equation 5.5
8. Check for convergence to the optimum. If satisfied, exit. Otherwise go to step 2.

The critical parts of optimization task is to find a usable search direction S^q, choose the scalar parameter α *that will minimize* $F(X^{q-1} + \alpha S^q)$ and finally test for convergence to the optimum.

5.2 Design Optimization Tools (DOT)

DOT is a general purpose numerical optimization software package which can be used to solve a wide variety of nonlinear optimization problems. The user provides a main program for calling DOT, and an analysis program to evaluate the necessary functions. DOT is linked with the user's codes to create the design optimization program. DOT will change the input parameters to the analysis in order to minimize or maximize the user defined objective, subject to constraints (limits) on other user defined responses. To achieve this, DOT calls the analysis program repeatedly while searching for the optimum [45]. Figure 5.3 shows the flowchart of optimization process coupled to ANSYS. In loop, ANSYS is called to rebuild the FE model with changed design variables).

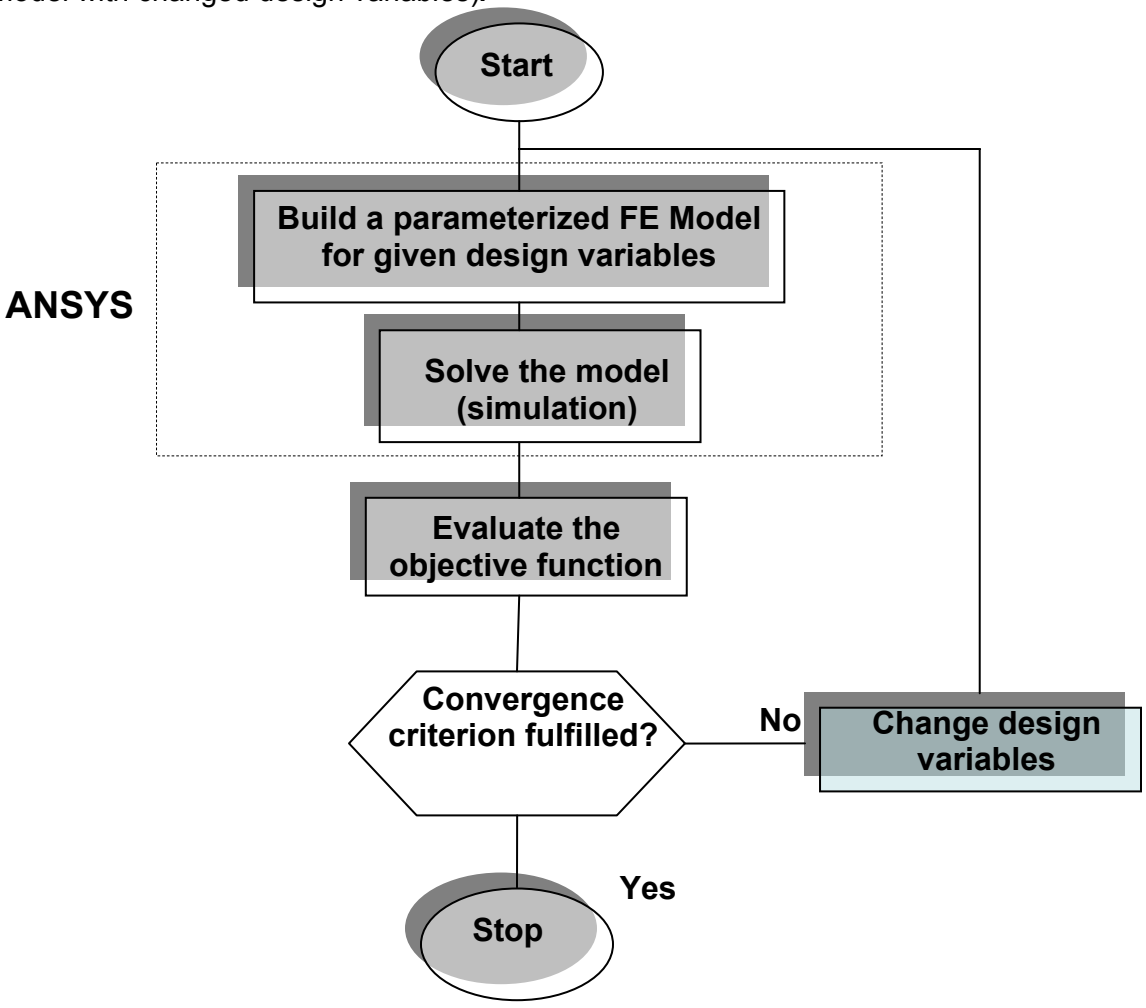

Figure 5.3 *Flowchart of optimization process coupled to ANSYS*

DOT is written in FORTRAN 77.

5.2.1 Finding the Search Direction

The first step in finding the search direction is to calculate the gradient of the objective function, $F(X)$. This may be provided by the user or (by default) will be calculated by DOT using finite difference methods. On the first iteration, we use the steepest descent direction. Therefore, the search direction is simply

$$S^q = -\nabla F(X^{q-1}) \tag{5.6}$$

If we always use the negative gradient of the objective function for our search direction, it would be what is called the steepest descent method. In the steepest descent method, the search direction is always perpendicular to the previous direction. However, this method is notoriously inefficient and should never be used as a general algorithm.

We only use the steepest descent direction if this is the beginning of the optimization (q=1), or of the optimization progress indicates that our search direction is poor due to nonlinearity or numerical reasons. On subsequent iterations, we will use the Broydon-Fletcher-Goldfarb-Shanno (BFGS) method, to determine the search direction [45]. The BFGS method is called also a quasi-Newton method because it creates an approximation to the inverse of the H matrix. H is matrix of second derivatives of the objective function. Initially, H is set to the identity matrix and the search direction is defined as: $S^q = -H\nabla F(X^{q-1})$. After the first iteration, H is updated using the following formula;

$$H^{q+1} = H^q + D^q \tag{5.7}$$

where

$$D^q = \left(\frac{\sigma+\tau}{\sigma^2}\right)pp^T - \frac{1}{\sigma}\left[H^q y p^T + p(H^q y)^T\right] \tag{5.8}$$

$$\sigma = p^T y \tag{5.9}$$

$$\tau = y^T H^q y \tag{5.10}$$

and

$$p = X^q - X^{q-1} \tag{5.11}$$

$$y = \nabla F(X^q) - \nabla F(X^{q-1}) \tag{5.12}$$

This method is considered to be theoretically best, but requires significant memory to store the H matrix (actually just the upper half, since H is symmetric). This method is considered to be less sensitive to the accuracy of the one-dimensional search [44]. This method can be proven to converge in N or fewer iteration for strictly quadratic functions. Once we have chosen the search direction, S^q, we search in this vector direction to find the value of that will minimize $F(X^{q-1} + \alpha S^q)$.

When no improvement can be found, a steepest descent direction will be attempted to see if this will improve the objective. If still no improvement can be found, the optimization is complete.

5.2.2 Convergence to the Optimum

Because optimization is an iterative process, stop criteria are the most important things. The DOT software uses several criteria to decide when to end the iterative search process, and these are described here:

- **Maximum Iterations**
  The default for this is 100 iterations (search directions). Usually, an optimum is found much sooner than this, so the maximum is mainly intended to avoid excessive computations

- **No Feasible Solution**

  If the initial design is infeasible (constraints are violated) our first priority is to overcome this and find a feasible solution. However, if there are conflicting constraints, this may not be possible. Therefore, if a feasible design has not been achieved in 20 iterations, the optimization process is terminated.

- **Point of Diminishing Returns**

  Probably the most common situation is where the optimum is approached asymptotically. Therefore, while some progress is still being made, continued iterations are not justified. Here, two criteria are used. The first is that the relative change in the objective between iterations is less than a specified tolerance, ε. Thus, the criteria is satisfied if

$$\frac{\left|F(X^{q})-F(X^{q-1})\right|}{\left|F(X^{q-1})\right|}\le\varepsilon \qquad (5.13)$$

  The default value for ε is 0.001.

  The second criterion is that the absolute change in the objective between iterations is less than a specified tolerance, ε. This criteria is satisfied if

$$\left|F(X^{q})-F(X^{q-1})\right|\le\varepsilon \qquad (5.14)$$

  The default value for ε is 0.0001.

  The reason for the two criteria is that if the objective function is large, the relative change between two successive iterations is an indication of convergence. However if F(X) is a very small number, a relative change will not be meaningful and so the absolute change will control convergence.

5.3 Implementation of DOT

Figure 5.4 shows a flexible optimization environment coupled to ANSYS process. Mathematica software is used as a driver. Its function *eval* takes the design variables (P, S, R and H) as arguments then, calls the external program ANSYS (for rebuilding the FE model) and finally evaluate objective function. Objective function value is transferred back to DOT optimizer. DOT communicates with Mathematica via Mathlink. More information on implementation can be found at http://evgenii.rudnyi.ru/soft/dot/.

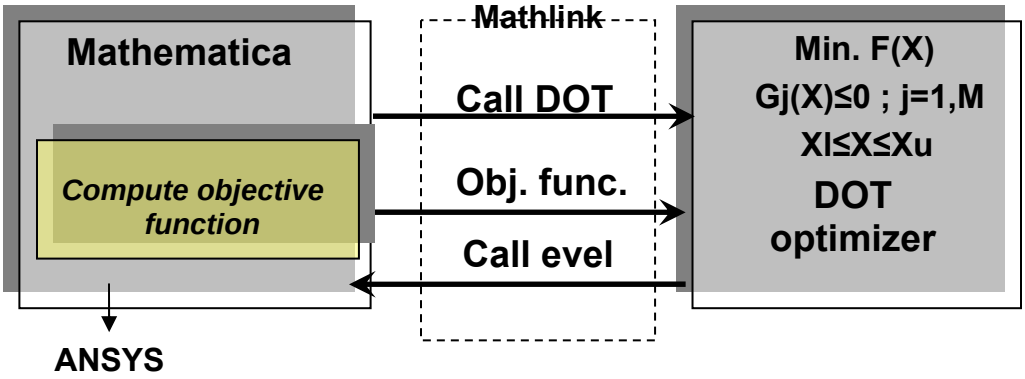

Figure 5.4 *DOT Implementation*

5.4 Optimization Results

In order to minimize our objective function, the following sets of equations are solved. As illustrated in figure 4.2, there are 16 design variables in our model. The flexible lower and upper bounds were set to $2.5X_i$ and $4.00\ X_i$ respectively. Here, a problem was defined as an unconstrained. The lower and upper bounds were imposed on the design variables.

Minimize $obj = \frac{\sigma}{\bar{H}} \times 100 = F(X_i) = F(P_1, P_2, P_3, P_4, S_1, S_2, S_3, S_4, R_1, R_2, R_3, R_4, H_1, H_2, H_3, H_4)$

Where $i = 1, 2, 3, \ldots\ldots,, 16$

And the bounds $0.25\ X_i \leq X_i \leq 4.00\ X_i$

Since, the initial guess is a very important starting point for an iteration process. First, we tried to carry out optimization process step by step, in order to find the best initial guess. BFGS method was selected for optimization.

5.4.1 Optimization of turns spacing (P)

P_1 to P_4, which stand for coil turns spacing or pitches (See figure 4.2), were considered as our design variables. Other parameters were considered as constant values equal to the values previously shown at the top of figure 4.1. Table 5.1 shows the initial values and the results of optimized pitches after running optimization process. In this step, the objective function (field inhomogeneity) decreases to 6.82% which is almost 30% improvement in comparison to the initial objective function which we have got for standard design in table 4.1 (9.6%).

In chapter 2, we tried to derive a simple formula for calculation of magnetic field at the center and at the end of a solenoidal coil by Biot-Savart law. After some assumptions, finally, equations 2.5 and 2.7 were derived and comparison showed that the magnetic field at the ends of a solenoid is one half that at the center.
To compensate this effect, one should apply the classical trick of so-called “end compensated” RF coils in which the outermost windings should be squeezed to a slightly smaller pitch. The optimization result shows that the outer winding should be closer, in the other word, the P_4 is smaller than P_2 and P_3. These results support the idea of end compensating. Furthermore, P_2 and P_3 have almost similar values (around 26 μm) and the pitch of innermost winding (=2 P_1) is equal to 29 μm, which is a little bit bigger than P_2 and P_3. These also refer to end compensating and thus are quite acceptable results.

	P_1(μm)	**P_2(μm)**	**P_3(μm)**	**P_4(μm)**	**Objective Function (%)**
Initial values	**20**	**30**	**40**	**50**	**14.20**
Optimized	**14.57**	**26.11**	**26.79**	**12.5**	**6.82**

Table 5.1 *The initial, optimized values of spacing (P) and objective function before and after optimization (as an example the initial values of P_1 to P_4 were set to 20, 30, 40 and 50 μm respectively)*

5.4.2 Optimization of coil's cross section length (R)

In this part, the optimized values of P_1 to P_4 from table 5.1 were considered and R_1 to R_4 defined as design variables. The optimization process was carried out to optimize the thickness of the coil (the coil's cross section length in figure 4.2). Table 5.2 shows the results of optimization. It seems that the thickness of the coil has no big influence in field homogeneity within the coil. As an example, the initial values equal to 20 has been shown in following table. For other initial values, the optimization program returned almost the same values too and initial and final objective functions were almost equal and have no big difference.

	R_1(μm)	R_2(μm)	R_3(μm)	R_4(μm)	Objective Function (%)
Initial values	**20**	**20**	**20**	**20**	**6.82**
Optimized	**20.58**	**21.15**	**17.00**	**18.36**	**6.72**

Table 5.2 *The initial, optimized values of length (R) and objective function before and after optimization (for S_1 =80, S_2 =80, S_3 =80, S_4 =80 μm and H_1 =20, H_2 =20, H_3 =20, H_4 =20 μm)*

5.4.3 Optimization of coil's cross section width (H)

For the third step, width of the coil turns was optimized. By keeping the previous optimized values defined in section 5.4.1 and 5.4.2, and considering H_1 to H_4 as our design variables, the following results were obtained (See table 5.3). The results showed that in order to minimize the field dispersion, the dimensions of coil windings should not be the same. The outer windings should be kept thinner and the inner one thicker in respect to dimensions. These refer to make higher current density in outermost to compensate the decreasing field along the coil.

	H_1(μm)	H_2(μm)	H_3(μm)	H_4(μm)	Objective Function (%)
Initial values	**20**	**20**	**20**	**20**	**6.72**
Optimized	**15.51**	**13.18**	**5.64**	**5.00**	**4.91**

Table 5.3 *The initial, optimized values of width (H) and objective function before and after optimization (for S_1 =80, S_2 =80, S_3 =80, S_4 =80 μm)*

5.4.4 Optimization of coils inner radios (S)

For optimization of coil diameter, the next step was started with the considering the previously obtained optimized values for P, R and H.

In this step, S_1 to S_4 were the design variables with the initial values of 80 μm. Table 5.4 shows the results of optimization process. Based on the optimized results, the radios of inner windings are the same and 73 μm was the optimized value, approximately. The outer windings should have different diameters, in order to minimize field non-uniformity far from the center. The last windings should be closer to the sample (considering that sample was placed within the coil) and the windings which are close to the end (S_3 in our model) should be pulled to a slightly bigger radios. These refer to balancing the slightly big field changes at the area close to the coil ends. The final objective function (4.21%) was 56% lower than the initial objective function which we have got for standard design in table 4.1 (9.6%) and resulted in more homogenous magnetic field.

	S_1(μm)	**S_2(μm)**	**S_3(μm)**	**S_4(μm)**	**Objective Function (%)**
Initial values	**80**	**80**	**80**	**80**	**4.91**
Optimized	**73.58**	**73.39**	**77.90**	**58.12**	**4.21**

Table 5.4 *The initial, optimized values of radios (S) and objective function before and after optimization*

5.4.5 Optimization of all the parameters

In the previous sections, the optimization processes were carried out through restriction of design variables to 4 (instead of 16) in each step. This approach led to better understanding of the influence of each design values on the field uniformity, separately and also to find the best initial guess's domain. By better understanding of initial guesses, one can reduce the number of iterations and function calls and consequently faster convergence to the solution.

So, the optimization procedure is implemented for the whole design variables (including all the 16 parameters) and the results are shown in table 5.5. These results were obtained after 63 function calls which takes 2.5 hours cpu. (around 2.5 minute per iteration). The objective function reduced to 4.18%.

5.5 Discussion

As already discussed in chapter 4, in harmonic analysis the DOF response (such as magnetic field) are assumed to be sinusoidal at a given constant frequency and using complex notation has amplitude and phase angle. Till now, we try to optimize the shape in order to homogenize the amplitude of H-field. Since the magnetic field, which is calculated by harmonic analysis is a complex value, the question arises that by optimization has the imaginary part of the magnetic field's dispersion been minimized, too? The imaginary part represents the phase shift and it is quite important to be minimized for MRI-imaging. For standard design, we have already mentioned that the objective function in respect to imaginary part is 304.8% (refer to table 4.1). This value represents a big dispersion in phase shift. To answer this question, we try to implement the optimization process for imaginary part separately. The results are shown in table 5.6. 82% Improvement in phase shift dispersion (from 304.8% to 55.28%), by optimization, is a quite considerable value.

	Initial design (μm)	Optimized design (μm)
P_1	20	14.57
P_2	40	26.11
P_3	40	26.79
P_4	40	12.50
S_1	80	75.35
S_2	80	76.28
S_3	80	78.89
S_4	80	59.88
R_1	20	19.99
R_2	20	19.99
R_3	20	20.00
R_4	20	20.00
H_1	20	15.51
H_2	20	13.18
H_3	20	5.64
H_4	20	4.99
Objective Function	9.6%	4.18%

Table 5.5 *The initial and optimized design values* ***(real or amplitude)***

	Initial design (μm)	Optimized design (μm)
P_1	20	14.58
P_2	40	26.11
P_3	40	26.79
P_4	40	12.50
S_1	80	80.22
S_2	80	79.37
S_3	80	80.75
S_4	80	78.92
R_1	20	19.99
R_2	20	19.99
R_3	20	19.90
R_4	20	19.87
H_1	20	15.51
H_2	20	13.19
H_3	20	5.64
H_4	20	5.00
Objective Function	304.8%	55.28%

Table 5.6 *The initial and optimized design values* ***(imaginary part)***

Comparison of optimized design values in both tables show that the only difference are in S values and in order to optimize the shape for imaginary response, the diameter of the coil should be kept a little bit bigger. As figure 4.7 in previous chapter depicts, the most of field dispersions and phase shifts are taken place at the area close to the conductors. It is reasonable if one say in order to decrease phase shift effects the windings should be pulled slightly far from the sample. If we consider the obtained optimized-dimensions in table 5.6 and run the simulation program for amplitude or real response of H-field, the program returns 4.80% as the objective function. And vise versa if we run the simulation program based on the optimized design values of table 5.5 and obtain the imaginary responses it returns 172.6% for objective function. Since, there is no big difference between 4.8% and 4.18% (the optimized value for real part) we consider the dimension of table 5.6 as the optimized dimensions.

Therefore, by considering these dimensions for manufacturing the microcoil, we expect 50 and 82% improvements in real and imaginary field dispersion respectively.

Figure 5.5 shows the magnetic field distribution in ROI (amplitude) after optimization. In comparison to figure 4.8, which shows the same but before optimization, one can easily recognize that how optimization makes the higher field homogeneity within the coil. These two figures depict the amplitudes of H-field in our region of interest.

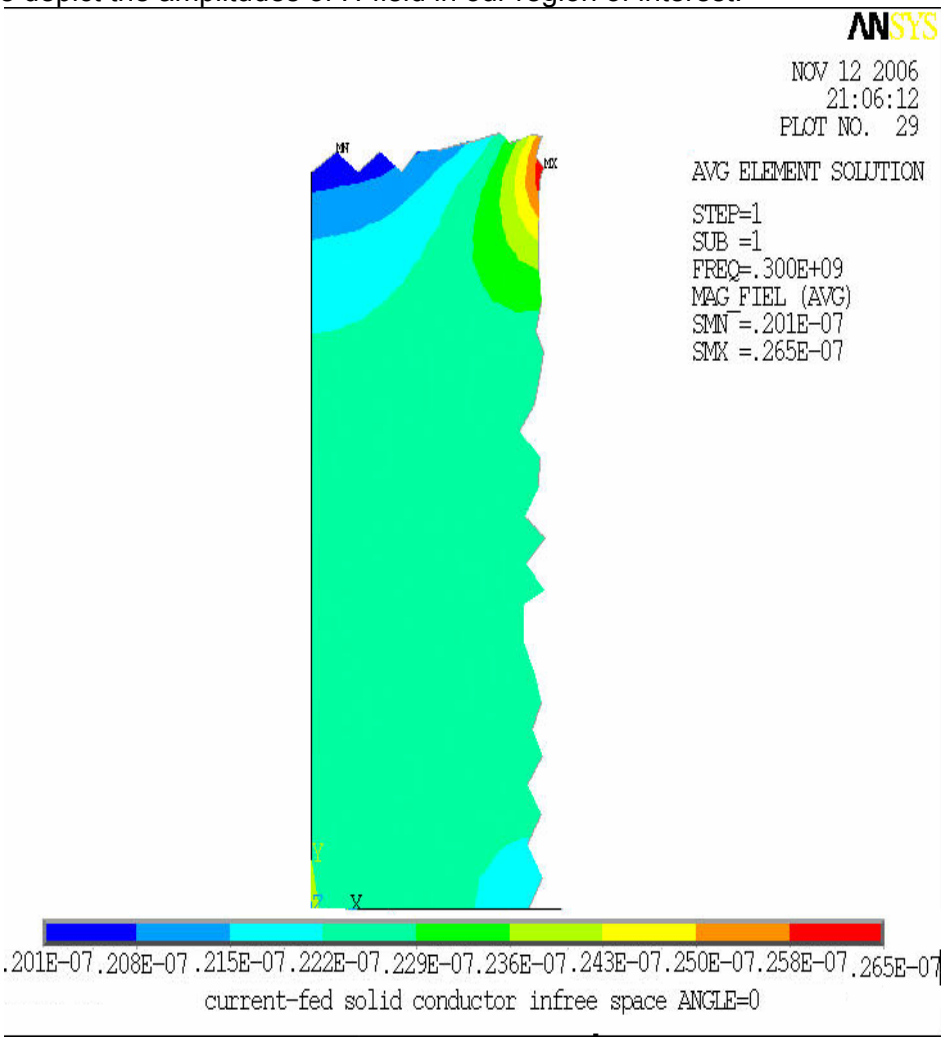

Figure 5.5 *Magnetic field distribution in ROI (Amplitude) after optimization*

Figure 5.6 shows the magnetic field imaginary response distribution of harmonic solution in ROI (imaginary) after optimization. As the figure shows, in most of the area there is no observable big phase shift.

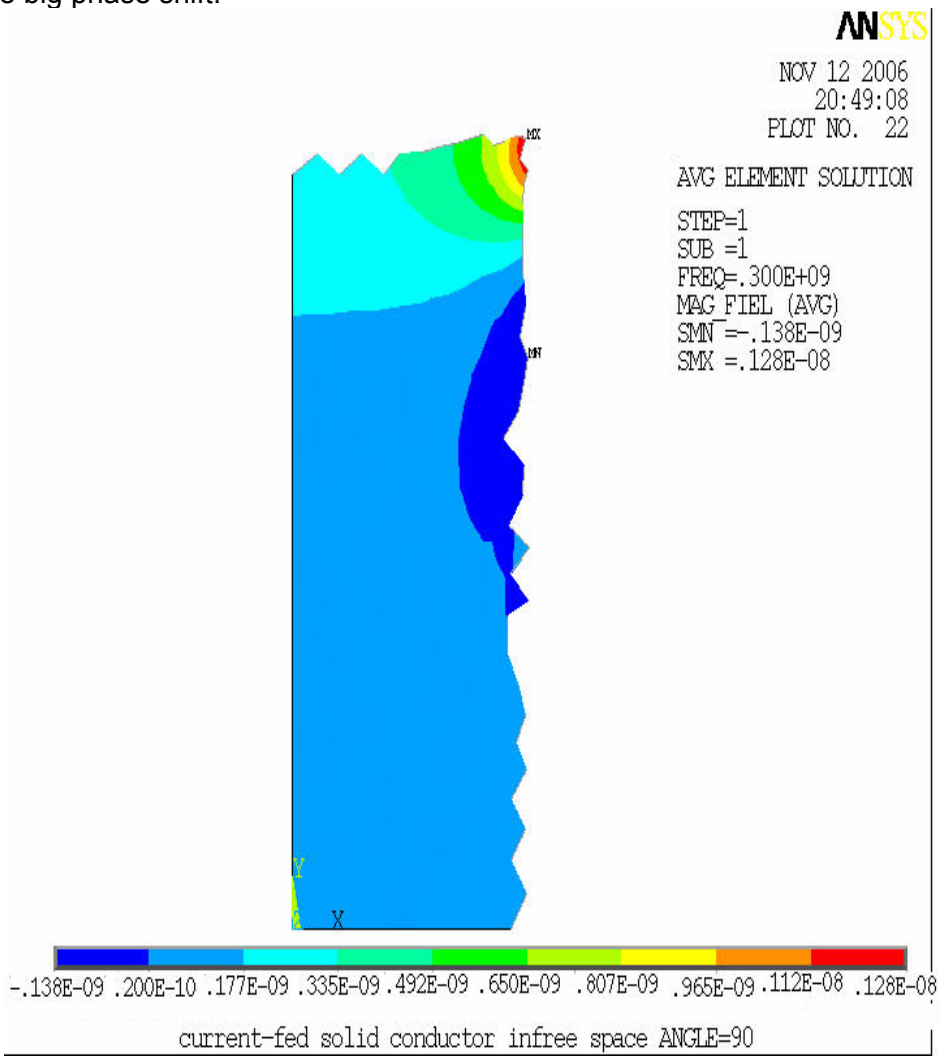

Figure 5.6 *Magnetic field distribution in ROI (imaginary) after optimization*

Figure 5.7 depicts an optimized-shape coil with a sample's tube inside it, schematically. The sizes are exactly the same values which considered as the optimized one in table 5.6.

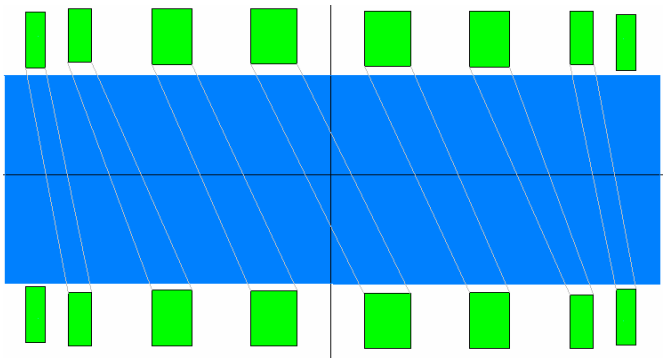

Figure 5.7 *Schematic of an optimized-shape coil with a sample's tube inside the coil (sizes are shown in table 5.6)*

6 Model Order Reduction (MOR)

The purpose of Model Order Reduction (MOR) is to replace a large system of equations by a smaller one, which preserves the essential properties of the original model. This smaller system must be an approximation of the larger system, in a sense that the input-output behavior of this system is comparable to the original, within certain accuracy. Therefore, the methods try to capture the essential features of the model in a small onel and preferable as quick as possible. One could further define extra properties, like stability, that have to be preserved in the reduction step [46]. Model order reduction of linear large-scale dynamic system is already an established area. Engineers can combine this technique with existing commercial finite element software in order to speed up a transient or harmonic analysis. In this chapter, we introduce and present the case of MOR for the ANSYS harmonic analysis of MRI microcoil and compare the results with respect to computational time and accuracy.

6.1 Principle of model order reduction

We start from the stable linear dynamic state-space system of the form [47]:

$$\begin{aligned} \dot{x}(t) &= \vec{A}x(t) + \vec{B}u(t) \\ y(t) &= \vec{E}^{T}x(t) \end{aligned} \tag{6.1}$$

Here t is the time variable, $x(t)$ is a state vector, $u(t)$ the input excitation vector and $y(t)$ the output measurement vector. A is the system matrix, B and E are input and output distribution array, respectively. The aim of MOR is to generate a low-dimensional approximation in the form

$$\begin{aligned} \dot{z}(t) &= \vec{A}_r z(t) + \vec{B}_r u(t) \\ y(t) &= \vec{E}_r^{\,T} z(t) \end{aligned} \tag{6.2}$$

where A_r is the reduced system matrix, B_r and E_r are reduced input and output distribution arrays. Equation 6.2 describes the dependence of the output vector y(t) on the input vector u(t) and the dimension of the reduced state vector z(t) is much less then the dimension of the original state vector $x(t)$. The main problem with equation (6.1) is the high dimensionality of the vector, which is typically equal to the product of the number of unknowns in a system of PDEs to be solved by the number of nodes introduced during the discretization process. This in turn leads to the high dimension of system matrices and finally to the huge computational cost to compute the system's response.

In performing model reduction on equation (6.1), the hope is that, for many systems of ODEs of practical importance, the behavior of vector x in time, t, is effectively described by some low-dimensional subspace as follows

$$x(t) = X\ z(t) + \varepsilon \tag{6.3}$$

Equation 6.3 states that, with the exception of a small error described by vector ε, the possible movement of the n-dimensional vector x belongs, for all times, to a k-dimensional subspace, with k much smaller than n, and is determined by an n x k transformation matrix X. The matrix is composed from k n -dimensional vectors that form a basis for the reduced subspace, and the k -dimensional vector z represents a new low order set of coordinates for the given basis [47].The task of model reduction is to find such a subspace for which the error difference in equation 6.3 is minimal. When the subspace is found, equation 6.1 should be projected onto it, and this projection process produces a system of ODEs of reduced order of equation 6.2.

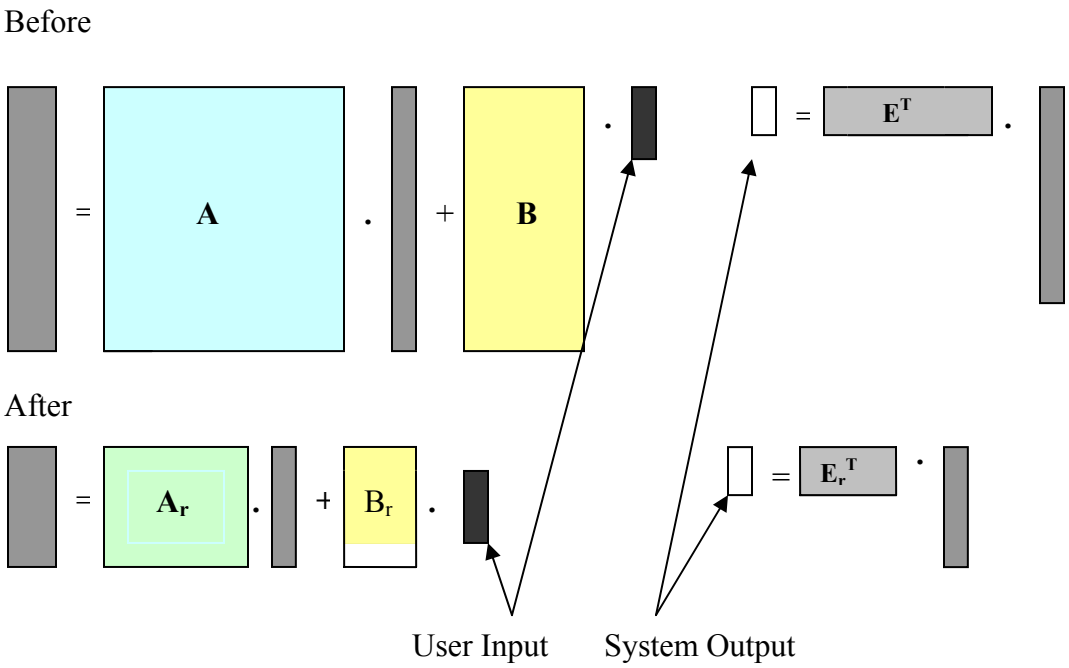

Figure 6.1 *Schematics of the system before and after the model reduction step [49]*

Krylov subspace allows us to obtain a low-dimensional subspace in equation 6.3. The best known Krylov subspace methods are Arnoldi process, Lanczos, GMRES (generalized minimum residual) and BiCGSTAB (stabilized biconjugate gradient). Due to its mathematical simplicity and numerical stability, Arnoldi process is the most suitable tool for model order reduction, in comparison with other methods [48]. More information about Krylov subspace and Arnoldi process can be found in [46, 48].

6.2 Defining our model

In our problem, after discretization, a system of ordinary differential equations is obtained

$$M\ddot{x} + E\dot{x} + Kx = Bu \qquad (6.4)$$
$$y = Cx$$

Remark: Most of the problems in mechanical systems in motion, as well as general, are usually described by systems of ODEs of second order in time. As already discussed in chapter 4, in harmonic analyses DOF responses are assumed to be sinusoidal and governed by equation 4.1. Substitution of the equation 4.1 into the linear equations of motion yields the following second order equation:

$$M\ddot{u} + C\dot{u} + Ku = F$$

where M, C and K are system matrices, u is the degree of freedom and F is load. It is a simple matter to convert it to the form of a first order equation by increasing number of unknowns and equations by a factor of two, e.g., by treating the first derivatives in time as unknown. Thus $M\ddot{u} + C\dot{u} + Ku = F$ together with y=du/dt, becomes

$$\begin{pmatrix} M & 0 \\ 0 & I \end{pmatrix} \cdot \frac{d}{dt}\begin{pmatrix} y \\ u \end{pmatrix} = -\begin{pmatrix} C & K \\ -I & 0 \end{pmatrix} \cdot \begin{pmatrix} y \\ u \end{pmatrix} - \begin{pmatrix} f \\ 0 \end{pmatrix}$$

which is in the form of first order equation.

where x is the vector of unknowns that includes all degrees of freedom, M , E, K are the mass, damping and stiffness matrices, B is the input, C the output matrix, u is the vector of inputs and y is the vector of outputs. After solution the model, our software uses a binary FULL file with the element matrices in order to assemble the global system matrices. The file format is documented and ANSYS supplies a library of Fortran subroutines to work with it.

6.3 mor4ansys

The software more4ansys has been developed in simulation group of university of Freiburg. The developed software comprises the two almost independent modules. The first one reads binary ANSYS files and assembles a dynamic system in the form of equation 6.1 for the first order systems or for the second order systems of equation 6.4. Then the second module applies the model reduction algorithm to equation 6.1 or 6.4, that is, it finds a low-dimensional subspace X in equation 6.3 such that it allows us to reproduce the harmonic behavior of the original state vector with required accuracy. The mor4ansys implement the block Arnoldi algorithm and follows the following steps:

Step 1: Reads system matrices from ANSYS
• First order ODEs
• Second order ODEs

Step 2: Performs model reduction
• Match Coefficients of Taylor Expansion of the transfer function.
• The Arnoldi process finds a projection matrix.
• Projection produces the reduced model
No user intervention is required and in many cases, the dimension of the reduced model up to 30 is already enough.

Step 3: Write the reduced model in matrix-market format
• Currently simulation with the reduced model is done in Mathematica.

6.4 MOR results

The computational time required for model extraction and for 21 frequency steps simulation, both of the full and the reduced order model are reported in table 6.1. The use of MOR allows a considerable speed up of the simulation time and even higher speed up factors are expected if finer frequency discretization is used. The simulation time of a harmonic analysis is a product of solution time for a complex linear system by the number of frequencies needed. Hence model reduction allows us to save the simulation time by a factor equal to a number of frequencies at which the harmonic response is required. For example, if it is necessary to estimate the transfer function at ten frequencies, then the model reduction plus the simulation of the reduced system is roughly ten times faster than the simulation of the original system.

It has been observed that for many ANSYS models the order of the reduced system 30 is enough to accurately represent the original high-dimensional system [48]. Hence, for simplicity we limit the analysis of the computational cost to this case. The simulation time of the reduced system comprising 30 equations is very small and we can neglect it. Thereafter,

in the case when several simulations with different input functions are necessary (the system-level simulation case), the advantage of model reduction is out of question.

Computation	Time (s)
ANSYS Harmonic simulation: for one frequency **(No. of nodes: 48779)** for 21 frequencies	 127 127*21=**2667**
MOR (*mor4ansys*): Reading the file Arnoldi Process (30 vectors) ----------	 2.3 34.0 ----------
TOTAL	**36.3**

Table 6.1 *Computational time comparison (4 Gb RAM in second)*

In order to find the accuracy of model order reduction, we try to calculate the DOF of a node within the coil and a node inside the conductor. The obtained results are shown in figure 6.1 to 6.6.

Figure 6.1 shows comparison between the full model and the reduced model simulation results for magnetic potential of a node within the coil and figure 6.2 illustrate the relative error of reduced model, both as a function of frequency in log scale.

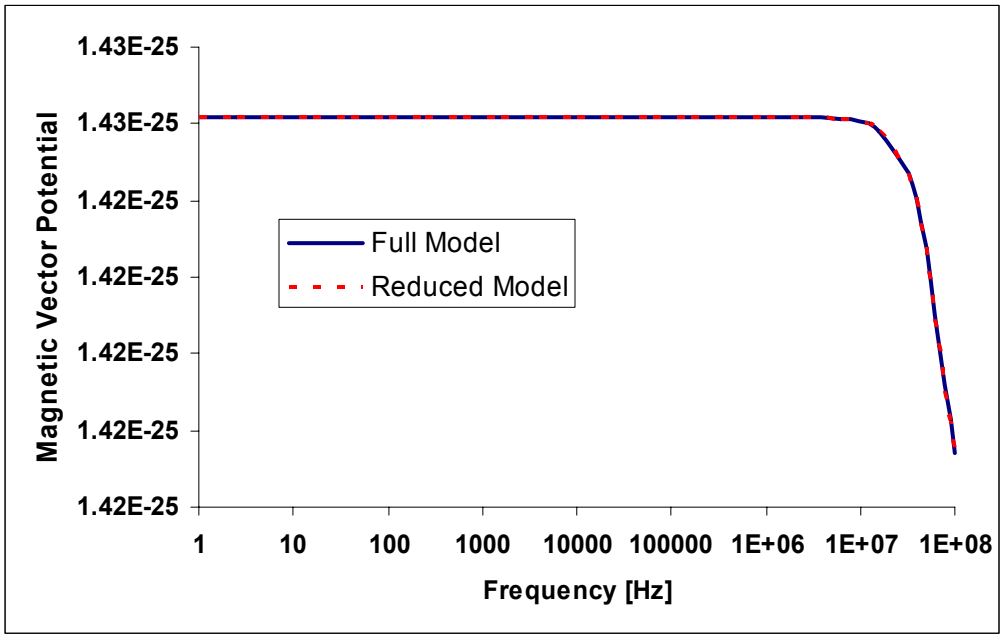

Figure 6.1 *Comparison between the full model and the reduced model simulation results for magnetic potential of a node within the coil*

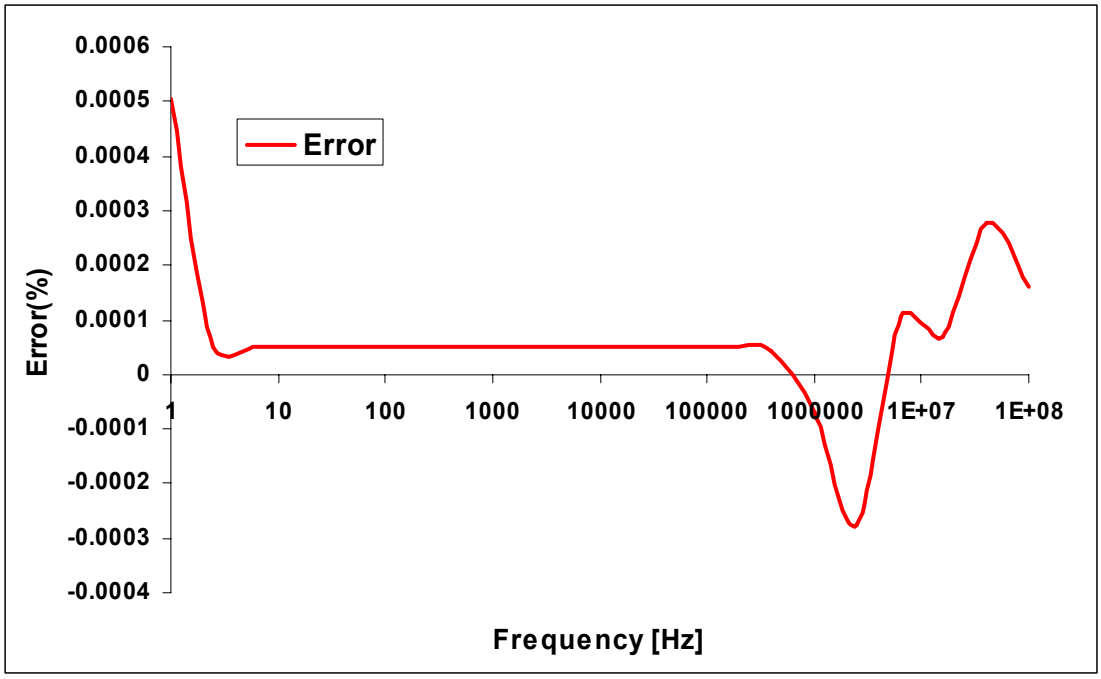

Figure 6.2 *Relative error of the reduced model simulation results for magnetic potential of a node within the coil*

Figure 6.3 depicts comparison between the full model and the reduced model simulation results for voltage of an arbitrary node inside the conductor and figure 6.4 illustrate the reduced model relative error, both as a function of frequency in log scale.

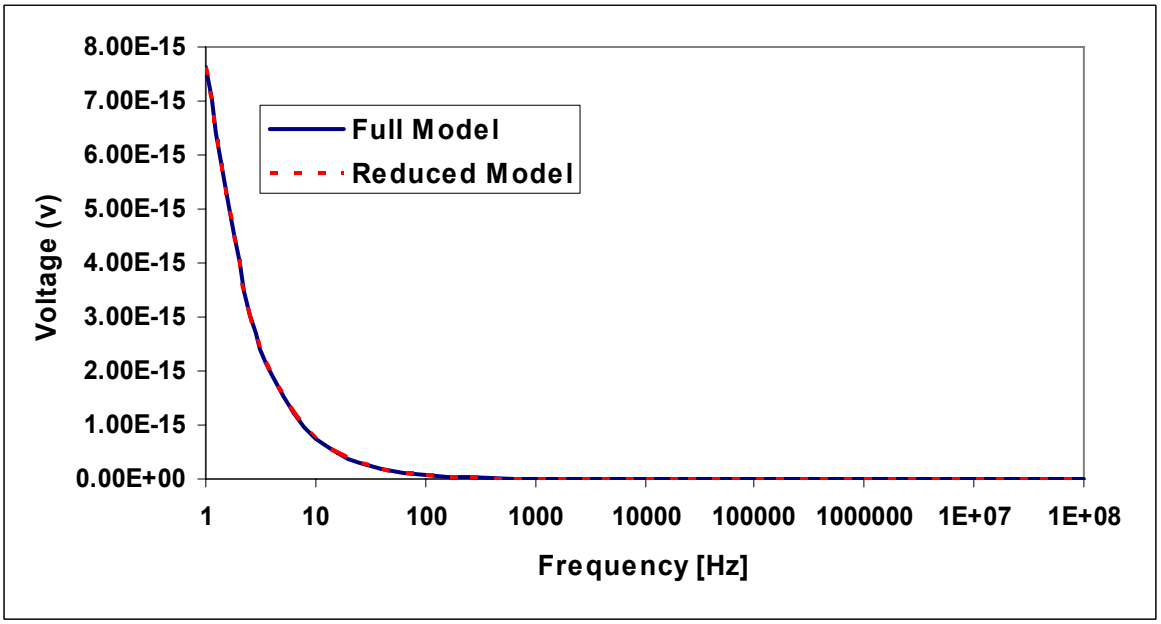

Figure 6.3 *Comparison between the full model and the reduced model simulation results for voltage of a node in conductor*

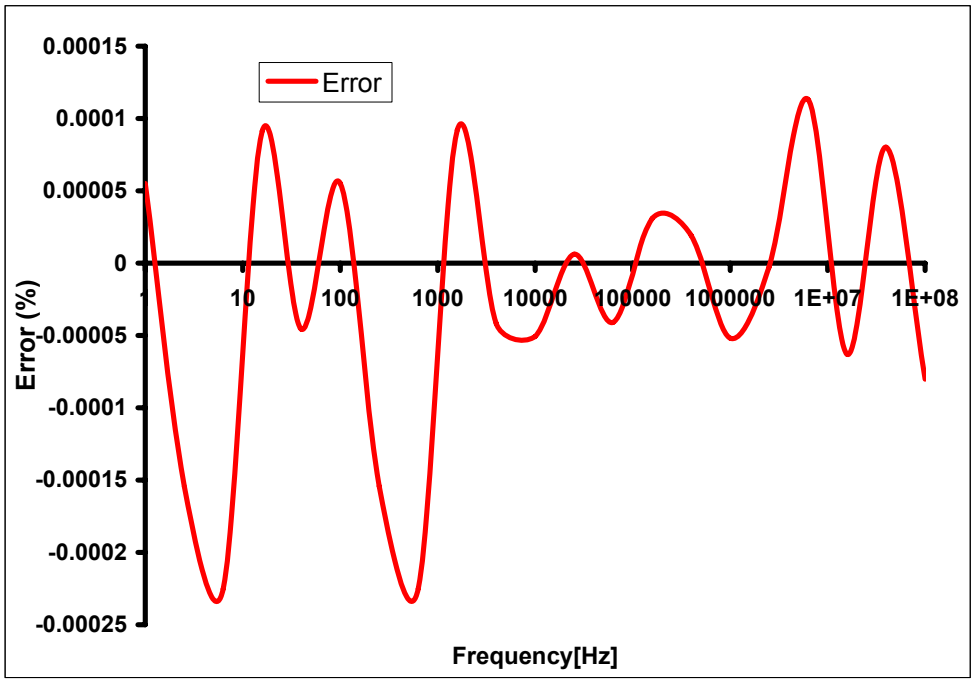

Figure 6.4 *Relative error of the reduced model simulation results for voltage of a node in conductor*

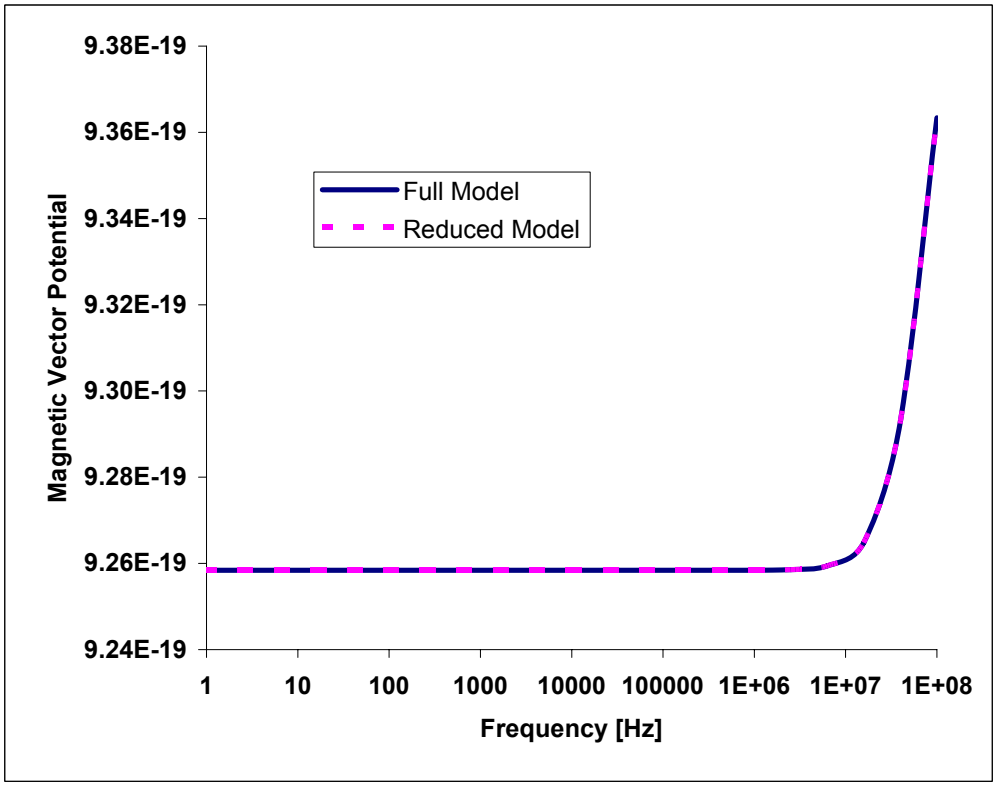

Figure 6.5 *Comparison between the full model and the reduced model simulation results for magnetic potential of a node in conductor*

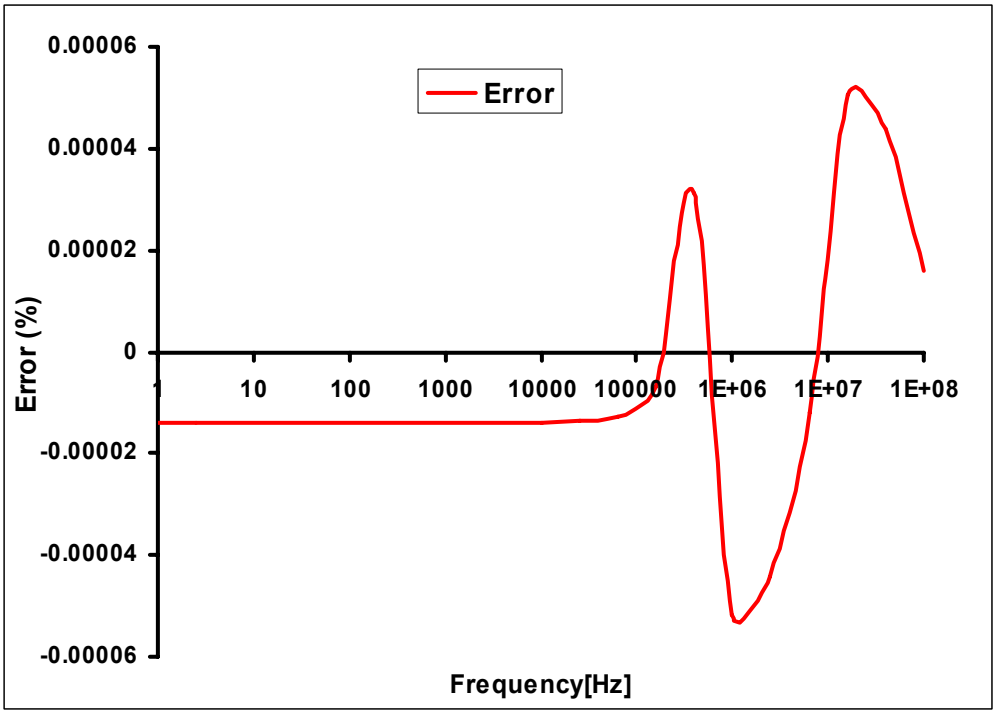

Figure 6.6 *Relative error of the reduced model simulation results for magnetic potential of a node in conductor*

Figure 6.5 illustrates comparison between the full model and the reduced model simulation results for magnetic potential of an arbitrary node inside the conductor and figure 6.6 illustrate the reduced model relative error, both as a function of frequency in log scale, too.

All figures shows that applied model order reduction is a very strong tool with respect to accuracy. The errors are in the range of less than 0.001%.

Furthermore, we have shown that in the case of linear first order system (equation 6.1 and 6.4) modern model reduction techniques can speed up finite element harmonic simulation significantly. As a conclusion, we can say that reduction of simulation time is essential for design optimization and system-level simulation and by model order reduction:

• Models of small dimension can be simulated in very short time. Especially, it is important when the frequency scan of a wide range frequency is necessary or an iterative optimization process is applied to find the best design.

• Moment matching via the Arnoldi process allows us to reduce the dimension of the original system by many orders of magnitude.

• The model reduction process is automatic as it is based on a formal procedure.

• The method can be applied to original model in dimension of up to 500 000 nodes.

• In many cases, the dimension of the reduced model up to 30 is already enough.

And finally the accuracy of MOR is significant.

7 Outlook

Our efforts in this project, mostly concentrated on uniformity of magnetic field within the micro solenoidal coil with non-circular cross section. In order to make a model we consider the following assumptions:

- 2-dimentional axis-symmetric model: The Freiburg University's ANSYS license allowed only the maximum node no. around 125,000. Therefore, we try to capture the essential features of the coil in a simple model.

- Linear material properties: The linear material properties will be an acceptable approach if the temperature considered to be almost constant (in the range of room temperature).

- The medium around the coductor was cosidered as air with μ_r equal to 1. In reality, cells are located in a tube of liquids, e.g., water. For most of the materials, the magnetic susceptibility is in the ppm range. However, for large magnetic fields, the effect of local variations in susceptibility, χ_v, cannot be ignored and results in undesired image artifacts in MRI experiments.

- Low frequency analysis: For low-frequency problems, the displacement current in Maxwell's equations is ignored ($\partial \vec{D} / \partial t$ =0). Therfore, charge accumulation and capacitance effects are excluded. This approach is valid when the working wavelength is much larger than the geometric dimensions of structure.

- Since the capacitive effects were neglected, the obtained DOF results do not show any resonance behavior under frequency scans.

And focus on field homogeneity does not mean that other specifications of coil are not important. The noise analysis and the coil resistance, quality factor as a good indication of coil's potential performance for a NMR experiment, susceptibility matching and signal to noise ratio are very important criteria for coil design.

In the future, one can continue this study in the following ways:

- 3D model and analysis

- Studying the temperature evolution in system under a very high frequency RF and implementation of an iterative method in case of nonlinear material properties (Coupled problem)

- Considering the different media within the coil and studying the effects of different materials with different susceptibility on the magnetic field.

- The FE model can be coupled with circuit components (including capacitive properties)

- Full-wave analysis (considering the displacement current and capacitive effects) and comparing the result with low-frequency analysis.

- When coil's self capacitance is taken into account, one can carry out the quality factor calculations for different coil shapes.

- Optimizing the shape in order to achieve higher Q-factor or higher SNR, too.

- Model order reduction of a LCR equivalent circuit model (considering self capacitance) and studying the resonance behavior of the coil in a given frequency domain.

References

[1] R. Damadian, "*Tumor Detection by Nuclear Magnetic Resonanec"*, *Science* 1971**,** *171* (976), 1151–1153.

[2] C. G. Fry, *"The Nobel Prize in Medicine for Magnetic Resonance Imaging"*, Vol. 81 No. 7 July 2004 • Journal of Chemical Education

[3] M. T. Vlaardingerbroek and J. A. den Boer, *Magnetic Resonance Imaging*, Third Edition, Springer

[4] G. Boero, *Integrated NMR Probe for Magnetometry*, vol. 9. Konstanz: Hartung-Gorre Verlag, 2000.

[5] D.I. Hoult and R.E. Richards, "The signal-to-noise ratio of the nuclear magnetic resonance experiment", Journal of Magnetic Resonance 24, (1976), 71-85.

[6] O. Zerbe., "*Lecture Course: NMR Spectroscop"y*: ETH, Swiss Federal Institute of Technology Zurich, Dept. of Chemical Sensors, Institute of Pharmaceutical Sciences, 2001. http://e-collection.ethbib.ethz.ch/show?type=lehr&nr=57

[7]C. Massin, "*Microfabricated Planar Coils in Nuclear Magnetic Resonance"*, vol. 15. Konstanz: Hartung-Gorre Verlag, 2004.

[8] J. P. Hornak, (1996-2006), *The Basics of MRI*. http://www.cis.rit.edu/htbooks/mri/

[9] M. Thompson (2002), "*Physics of MRI*. http://www.phys.cwru.edu/courses/p431/notes-2003/index.html

[10] K. R. Minard and R. A. Wind*, "Solenoidal microcoil design. Part I: Optimizing RF homogeneity and coil dimensions,"* Concepts in Magnetic Resonance*, vol. 13, pp. 1[6]-142, 2001.*

[11] K. R. Minard and R. A. Wind*, "Solenoidal microcoil design - Part II: Optimizing winding parameters for maximum signal-to-noise performance,"* Concepts in Magnetic Resonance*, vol. 13, pp. 190-210, 2001*

[12] A. Hasse *et al*," NMR Probe-heads for *In Vivo* Applications", Concepts in Magnetic Resonance, Vol. 12(6),pp. 361-388 (2000)

[13] L. Ciobanu, A. G. Webb, C. H. Pennington," Magnetic resonance imaging of biological cells", Progress in Nuclear Magnetic Resonance Spectroscopy 42 (2003) 69–93

[14] Mona Klein, "Diploma Thesis", "Design and Fabrication of Solenoidal Microcoils with Integrated Sample Container for Micro-MRI using RIE", IMTEK, Freiburg university-Germany (2006)

[15] P. Glover, Sir P. Mansfield, "Limits to magnetic resonance microscopy", Rep. Prog. Phys. 65, pp.1489–1511(2002)

[16] S. C. Lee, K. Kim, J. Kim, S. Lee, J. H. Yi, S. W. Kim, K. S. Ha, and C. Cheong, "One micrometer resolution NMR microscopy," *Journal of Magnetic Resonance*, vol. 150, pp. 207-213, 2001.

[17] B. F. Brehm-Stecher and E. A. Johnson, "Single-cell microbiology: Tools, technologies, and applications," *Microbiology and Molecular Biology Reviews*, vol. 68, pp. 538, 2004.

[18]P. J. M. van Bentum, J. W. G. Janssen, and P. M. Kentgens, "Towards nuclear magnetic resonance μ-spectroscopy and μ-imaging," *Analyst*, vol. 129, pp. 793-803, 2004.

[19] L. Ciobanu, "Magnetic resonance imaging of biological cells," *Progress in Nuclear Magnetic Resonance Spectroscopy*, vol. 42, pp. 69-93, 2003.

[20] S. Gravina, D.G. Cory, "*J. Magn. Reson*". Ser. B 104 (1994) 53.

[21] S. Choi, X. W. Tang, D.G. Cory, "*Int. J. Imag. Syst. Technol*.". 8 (1997) 263.

[22] L. Ciobanu, D.A. Seeber, C.H. Pennington," *J. Magn. Reson*". 158 (2002) 178.

[23] T. Dohi, K. Matsumoto, and I. Shimoyama, "*The Flexible Micro Resonator For The Magnetic Resonance Catheter*", *TRANSDUCERS'05*, Seoul, Korea, June 5-9, (2005).

[24] J. B. Aguayo, S. J. Blackband, J. Schoeniger, M. A. Mattingly and M. Hinterman, "*Nuclear magnetic resonance imaging of a single cell*", *Nature* **322** 190–1, (1986)

[25] M. Armenean, A. Briguet, H. Saint-Halmes, "*Conception de microbobines radiofrequence pour la RMN*", C. R. Biologies 325 (2002) 457-463

[26] A. G. Webb, "*Radiofrequency microcoils in magnetic resonance*", Progress in Nuclear Magnetic Resonance Spectroscopy 31 (1997) 1-42

[27] D. Morris, P. G. Gorkov, A. B. Harris, J. Tsao, K. Moser, J. Georgiadis , A. Webb and P. C. Lauterbur, (1999) "*Microsamples, micro-coils, micro-magnets: where will all this smallness end*?" *L16, In Book of Abstracts for 5th International Conf. on Magnetic Resonance Spectroscopy (Heidelberg)*

[28] W. H. Hayt, "*Engineering Electromagnetics Seventh Edition*",(2006), McGraw Hill, New York ISBN 0-07-310463-9

[29] F.E. Terman, "*Radio Engineers' Handbook"*, McGraw-Hill 1943

[30] P. J. M. van Bentum, J. W. G. Janssen and A. P. M. Kentgens, "*Towards nuclear magnetic resonance micro-spectroscopy and micro-imaging*"**,** Analyst, (2004), 129,793-803

[31] P. Froehlich, "*Use of Microcoil Probes to Acquire More Sensitive NMR Spectral Data*", AMERICAN LABORATORY, FEBRUARY 2005, pp. 54-58

[32] G. Boero, M. Bouterfas, C. Massin, F. Vincent, P. A. Besse, and R. S. Popovic,"*Electron-spin resonance probe based on a 100 μm planar microcoil*",Review of Scientific Instruments Vol. 74, No. 11 Nov. 2003

[33] T. L. Peck, R. L. Magin and P. C. Lauterbur," *Design and Analysis of Microcoils for NMR Microscopy*", Journal of Magnetic Resonance, Series B 108, 114-124 (1995)

[34] U. van Rienen, "*Numerical Methods in Computational Electrodynamics - Linear Systems in Practical Applications*", Springer, Lecture Notes in Computational Science and Engineering, Vol. 12 (2001).

[35] T. Weiland, "*Finite Integration Method and Discrete Electromagnetism",* pp. 183-198 in *Computational Electromagnetics*, Springer, Lecture Notes in Computational Science and Engineering, Vol. 28 (2003).

[36] Tipler, Paul, *"Physics for Scientists and Engineers: Electricity, Magnetism, Light, and Elementary Modern Physics (5th ed.)"*, W. H. Freeman (2004)

[37] Purcell, Edward M.,"*Electricity and Magnetism"*, McGraw-Hill (1985)

[38] P. Kohnke, "*ANSYS Inc Theory Manual*", Release 8.0, Chapter 5 (2000)

[39] P. P. Silvester, R. L. Ferrari, "*Finite Element for Electrical Engineers",* Cambridge University Press, Third Edition (1996)

[40] S. S. Rao, "*Finite Element Analysis in Engineering"*, Butterworth-Heinemann; 3 edition (1998)

[41] O. C. Zienkiewicz, '*The Finite Element Method*", 3rd Edition (1977), McGraw-Hill Book Co. (UK)

[42] Sheldon's ANSYS.NET Tips and Tricks, available in http://ansys.net/ansys/?mycat=search&mytype=Tips&mycategory=Sheldon

[43] DOT, design optimization tool, available in www.vrand.com/education

[44] G. N. Vanderplaats, "*Numerical Optimization Techniques for Engineering Design: With Applications*", McGraw Hill, N., Y., 1984

[45] Dot User Manual version 4.20, VR&D, 1995

[46] P. Heres, "*Robost and Efficient Krylov Subspace Methods for Model Order Reduction",*Eindhoven, 2005, ISBN 90-386-0724-5

[47] E. B. Rudnyi and J. G. Korvink, *"Automatic Model Reduction for Transient Simulation of MEMS-based Devices"*, Sensors Update; Wiley-VCH, 2003; Volume 11;pp 1-26

[48] T. Bechtold's Phd. Dissertation, *"Model Order Reduction of Electro-Thermal MEMS"*, University of Freiburg-Germany, 2005

[49] T. Bechtold, E. B. Rudnyi and J. G Korvink,*" Dynamic electro-thermal simulation of microsystems: a review "; J.* Micromech. Microeng. **15** (2005) R17–R31

ACKNOWLEDGMENTS

First of all, I would like to express my gratitude to both Prof. J. G. Korvink and Prof. L. Pagel for enabling me to have this unique research experience.

Particularly, I would like to thank Prof. Korvink for assigning me as his Master student with this special topic, for his constant encouragement throughout my work, and financial support to cover my living expenses partly.

I am especially thankful to Dr. E. Rudnyi for his excellent advice and sharing his invaluable knowledge and experience in all steps of my research, without which this work would not have been possible. Furthermore, I would also like to thank Dr. Zhenyu Liu for his comments on optimization that proved very helpful. Also, I would like to thank Ph.D. students Laura Deltin for her always kind and immediate assistance, especially in modeling, simulation and model order reduction. I would like to thank Mona Klein for clarifying discussions on MRI, and for providing me with a better sense of the objectives.

Every single person in Simulation group of IMTEK, university Freiburg helped me to succeed, especially Dr. A. Greiner, Ph.D. students J. Lienemann and C. Moosmann. Thanks a lot for their helps.

Also on the Rostock side, I owe special thanks to Prof. U. van Rienen to organize the master course in Computational Engineering.

Finally, I would like to thank my family, my wife Azin and my son Shayan, who gave me all the freedom and support I ever wanted during my hard work on the project.

Appendices

1) ANSYS CODE FOR MODELING AND SIMULATION OF A MICROCOIL

```
/filname,geo,0

/prep7

/title, current-fed solid conductor in free space
/com,   Calculate the voltage in the coil from an applied AC current

et,1,53,,,1        ! air
et,2,53,1,,1        ! current force wire
et,3,110,,,1       ! far-field


emunit,mks


!****************** geometry and material properties

mp,murx,1,1
mp,murx,2,1
mp,rsvx,2,17e-9   ! resistivity of coils T Omh*um


m=1
p1=14.57e-6*m
p2=26.11e-6*m
p3=26.79e-6*m
p4=12.50e-6*m
s1=80.22e-6*m
s2=79.37e-6*m
s3=80.75e-6*m
s4=78.92e-6*m
r1=20.00e-6*m
r2=20.00e-6*m
r3=20.00e-6*m
r4=20.00e-6*m
h1=15.51e-6*m
h2=13.18e-6*m
h3=5.64e-6*m
h4=5.00e-6*m
f=3e8



!****************** build and mesh model

rectng,s1,s1+r1,p1,h1+p1
rectng,s2,s2+r2,h1+p1+p2,h1+p1+p2+h2
rectng,s3,s3+r3,h1+p1+h2+p2+p3,h1+p1+h2+p2+p3+h3
rectng,s4,s4+r4,h1+p1+h2+p2+h3+p3+p4,h1+p1+h2+p2+h3+p3+p4+h4
```

```
pcirc,0,5*s1,0,90
pcirc,0,10*s1,0,90
aovlap,all
asel,s,loc,x,s4,s1+r1
aatt,2,,2
cm,coil,area
csys,1
asel,s,loc,x,0,5*s1
asel,u,,,coil
aatt,1,,1
cm,air,area
asel,all
asel,s,loc,x,5*s1,10*s1
aatt,1,,3
cm,far,area
allsel
csys,0
lsel,s,loc,x,0,s1+r1
lsel,r,loc,y,h1+p1+h2+p2+h3+p3+h4+p4
lesize,all,,,100
lsel,all
mshape,0,2d         ! mapped mesh with quads
mshkey,1
esize,,50
amesh,coil          ! mesh far-field and coil
csys,1
lsel,s,loc,x,5*s1
lesize,all,,15
lsel,all
mshape,0,2d         ! mapped mesh with quads

esize,,1
amesh,far
smrtsize,2
esize,s1/12
mshape,1,2d          ! specify triangle elements
mshkey,0            ! free mesh
amesh,air            ! mesh air region


!**************** set boundary conditions

csys,0
n1=node(s1,p1,0)                  ! get a node on the coil
n2=node(s2,h1+p1+p2,0)            ! get a node on the coil
n3=node(s3,h1+p1+h2+p2+p3,0)      ! get a node on the coil
n4=node(s4,h1+p1+h2+p2+h3+p3+p4,0)  ! get a node on the coil
csys,1
nsel,s,loc,x,10*s1
sf,all,inf          ! set infinite surface flag
allsel
csys,0
allsel
nsel,s,loc,x,s1,s1+r1
nsel,r,loc,y,p1,h1+p1
cp,1,volt,all
```

```
allsel
nsel,s,loc,x,s2,s2+r2
nsel,r,loc,y,h1+p1+p2,h1+p1+h2+p2
cp,2,volt,all
allsel
nsel,s,loc,x,s3,s3+r3
nsel,r,loc,y,h1+p1+h2+p2+p3,h1+p1+h2+p2+h3+p3
cp,3,volt,all
allsel
nsel,s,loc,x,s4,s4+r4
nsel,r,loc,y,h1+p1+h2+p2+h3+p3+p4,h1+p1+h2+p2+h3+p3+h4+p4
cp,4,volt,all
allsel
f,n1,amps,1e-12        ! current applied
f,n2,amps,1e-12        ! current applied
f,n3,amps,1e-12        ! current applied
f,n4,amps,1e-12        ! current applied
allsel
nsel,s,loc,x,0
d,all,az,0
allsel
finish

!************************* Solution ****************
ALLSELE
/SHOW,JPEG
JPEG,ORIENT,HORIZ
/GFILE,600,
/RGB,INDEX,100,100,100,0
/RGB,INDEX,0,0,0,15

/solu
!*
antype,harm
eqslv,spar,
harfrq,f,
nsubst,1
kbc,1
!*
hropt,full
hrout,on
!*
solve
finish

!************************* Post processing *****

Pi=acos(-1)
/post1

subset,1,1,,0              !read real solution
*get,dofv1_r,node,n1,volt
*get,dofv2_r,node,n2,volt
*get,dofv3_r,node,n3,volt
*get,dofv4_r,node,n4,volt
```

```
subset,1,1,,1
*get,dofv1_i,node,n1,volt
*get,dofv2_i,node,n2,volt
*get,dofv3_i,node,n3,volt
*get,dofv4_i,node,n4,volt

v1_r=(-2*Pi*f*dofv1_i)
v2_r=(-2*Pi*f*dofv2_i)
v3_r=(-2*Pi*f*dofv3_i)
v4_r=(-2*Pi*f*dofv4_i)
v1_i=(2*Pi*f*dofv1_r)
v2_i=(2*Pi*f*dofv2_r)
v3_i=(2*Pi*f*dofv3_r)
v4_i=(2*Pi*f*dofv4_r)
sum_V_r=2*v1_r+v2_r+v3_r+v4_r
sum_V_i=2*v1_i+v2_i+v3_i+v4_i

*CFOPEN,voltage,coil
*vwrite,v1_r,v2_r,v3_r,v4_r,sum_V_r
(E15.5,' ',E15.5,' ',E15.5,' ',E15.5,' ',E15.5)
*vwrite,v1_i,v2_i,v3_i,v4_i,sum_V_i
(E15.5,' ',E15.5,' ',E15.5,' ',E15.5,' ',E15.5)

*CFCLOS

subset,1,1,,0

asel,s,loc,x,s1,s1+r1
asel,r,loc,y,0,h1/2
curr2d
c1_r=-tcurr

asel,s,loc,x,s2,s2+r2
asel,r,loc,y,h1/2+p1,h1/2+p1+h2
curr2d
c2_r=-tcurr

asel,s,loc,x,s3,s3+r3
asel,r,loc,y,h1/2+p1+h2+p2,h1/2+p1+h2+p2+h3
curr2d
c3_r=-tcurr

asel,s,loc,x,s4,s4+r4
asel,r,loc,y,h1/2+p1+h2+p2+h3+p3,h1/2+p1+h2+p2+h3+p3+h4
curr2d
c4_r=-tcurr

avg_C_r=(c1_r+c2_r+c3_r+c4_r)/4

subset,1,1,,1

asel,s,loc,x,s1,s1+r1
asel,r,loc,y,0,h1/2
curr2d
c1_i=-tcurr
```

```
asel,s,loc,x,s2,s2+r2
asel,r,loc,y,h1/2+p1,h1/2+p1+h2
curr2d
c2_i=-tcurr

asel,s,loc,x,s3,s3+r3
asel,r,loc,y,h1/2+p1+h2+p2,h1/2+p1+h2+p2+h3
curr2d
c3_i=-tcurr

asel,s,loc,x,s4,s4+r4
asel,r,loc,y,h1/2+p1+h2+p2+h3+p3,h1/2+p1+h2+p2+h3+p3+h4
curr2d
c4_i=-tcurr

avg_C_i=(c1_i+c2_i+c3_i+c4_i)/4


mag_Z=avg_C_i**2+avg_C_r**2
imped_r=-(avg_C_r*sum_V_r+avg_C_i*sum_V_i)/mag_Z
imped_i=-(avg_C_r*sum_V_i-avg_C_i*sum_V_r)/mag_Z

*CFOPEN,current,coil
*vwrite,c1_r,c2_r,c3_r,c4_r,avg_C_r,imped_r
(E15.5,' ',E15.5,' ',E15.5,' ',E15.5,' ',E15.5,' ',E15.5)
*vwrite,c1_i,c2_i,c3_i,c4_i,avg_C_i,imped_i
(E15.5,' ',E15.5,' ',E15.5,' ',E15.5,' ',E15.5,' ',E15.5)

*CFCLOS

/post1
!*
APLOT
EPLOT
PLESOL, H,SUM, 0
!*
PLESOL, JT,SUM, 0
!*
/EFACET,1
PLNSOL, H,SUM, 0
/post1

HRCPLX,1,,400                    ! 90 for imaginary, 0 for real and bigger than 360 for amplitude
PLESOL, H,y
csys,0
nsel,s,loc,x,0,0.8*s4
nsel,r,loc,y,0,h1+p1+h2+p2+h3+p3+h4+p4
esln,r,0,all

/post1

ETABLE,Mag_Field,H,y                    !Make a table for H
PLETAB,Mag_Field,AVG
PRETAB,Mag_Field
!*
SSUM                                    ! Sum of H
```

```
*get,sum_H,SSUM,0,ITEM,Mag_Field      ! Get  sum of H
!*
!*
ETABLE,,VOLU                                  ! Make a table for Element Volume(Area)
!PLETAB,VOLU,AVG
PRETAB,VOLU
!*
SSUM                                          ! Sum of area
*get,sum_A,SSUM,0,ITEM,VOLU           ! Get sum of Area
!*
!*
SEXP,H2,MAG_FIELD, ,2,1,                  ! Make a Table for H-Square
!PRETAB,H2
PRETAB,H2
!*
SSUM                                          ! Sum of H-Square
*get,sum_H2,SSUM,0,ITEM,H2            ! Get sum of H-Square
!*
!*
SMULT,A_H,Mag_Field,VOLU,1,1          ! Make a Table for H*A
!PLETAB,A_H
PRETAB,A_H
!*
SSUM                                ! Sum of H*A
*get,sum_A_H,SSUM,0,ITEM,A_H          ! Get sum of H*A
!*
!*
SEXP,A_H2,Mag_Field,VOLU,2,1          ! Make a Table for H-Square*A
!PLETAB,A_H2
PRETAB,A_H2
!*
SSUM                                          ! Sum of H-Square*A
*get,sum_A_H2,SSUM,0,ITEM,A_H2        ! Get sum of H_Square*A
!*
!*
Mean_H=sum_A_H/sum_A                  ! Weighted Mean For H
Sq_Mean_H=Mean_H**2
!*
!*
Dev_H=sqrt((sum_A_H2-Sq_Mean_H*sum_A)/sum_A)     ! Standard Devaition
!*
!*
Obj_fun=Dev_H/Mean_H                  ! Object Function

*CFOPEN,H-Field,sum
*vwrite,sum_H,sum_A,sum_H2,sum_A_H,sum_A_H2,Mean_H,Dev_H,Obj_fun
(E15.5,' ',E15.5,' ',E15.5,' ',E15.5,' ',E15.5,' ',E15.5,' ',E15.5,' ',E15.5)
*CFCLOS
PLESOL, H,y

finish
```

2) MATHEMATICA CODE FOR CALLING THE OPTIMIZATION PROGRAM DOT

```
lnk = Install["/usr/groups/simulation/simstaff/user/rudnyi/mathlink/dot/calldot"]

writeParam[X_] := Module[{of},
        of = OpenWrite["param.ans", FormatType->OutputForm];
        Write[of, "p1 = "<>ToString[X[[1]]*1*^-6, CForm]];
        Write[of, "p2 = "<>ToString[X[[2]]*1*^-6, CForm]];
        Write[of, "p3 = "<>ToString[X[[3]]*1*^-6, CForm]];
        Close[of]
]

eval[X_] := Module[{},
        writeParam[X];
        Print[FullForm[X]];
        Run["./ans81 model"];
        res = Import["B_Field.sum", "List"];
        Print[res];
        {res[[7]]/res[[3]],{}}
]

(*eval[{40.*^-6, 40.*^-6, 40.*^-6}]*)


x = {30., 40., 50.};
xl = x/4;
xu = x*2.5;
prpm = Table[0., {20}];
iprm = Table[0, {20}];
method = 1;
iprint = 3;
minmax = -1;
ncon = 0;
nrwk = 8000;
nriwk = 8000;

runDOT["eval", "outfile", "postfile", method, iprint, x, xl, xu, minmax, ncon, prpm, iprm,
nrwk, nriwk]

Uninstall[lnk]
```

3) COMMENTS ON STEPS OF RUNNING MOR4ANSYS

1) building model

model.ans

produces file.db

2) making matrices

matrices.ans

produces filefreq1.full and outdof.txt

3) model reduction

user/rudnyi/mor/v2.0/mor4fem filefreq1.full -C outdof.txt -s UMFPACK -x 1e5 -t 1e-20

produces mor.* files

4) harmonic simulation in ANSYS

harmonic.ans

produces harmonic.txt

5) comparison

plots.nb in Mathematica

4) MATRICES.ANS CODE (FOR MODEL ORDER REDUCTION)

```
resume
*CFOPEN, outdof, txt,
*vwrite,'azcenter','AZ',n0
%C %C %I
*vwrite,'voltcoil','VOLT',n1
%C %C %I
*vwrite,'azcoil','AZ',n1
%C %C %I
*CFCLOS
/filname,filefreq1
/solu
allsel
antype,harmic
eqslv,sparse
harfrq,1/2/3.141592653589793
nsubst,1
wrfull,1
solve
fini
```

5) HARMONIC.ANS CODE (FOR MODEL ORDER REDUCTION)

```
resume

nstep=21
nvar=4
n=nstep-1
freqmin=1
freqmax=1e8

allsel

*dim,tmparr1,array,1
*dim,tmparr2,array,1
*dim,tmparr3,array,1

/prep7
*cfopen,harmonic.txt,names
*vwrite,'Frequency'
%C
*vwrite,'azcenter','voltcoil','azcoil'
%C %C %C
*cfclos


*CFOPEN, harmonic,txt
*vwrite,'%%Matrix','Market m','atrix ar','ray real',' general'
(5A8)
*VWRITE,nvar,n
%I %I

finish

*do,i,1,nstep
/solu
antype,harm
eqslv,sparse
nsubst,1
outres,NSOL,last
kbc,1
expf=(i-1)/(nstep-1)*(log10(freqmax)-log10(freqmin))+log10(freqmin)
f=10**expf
harfrq,f
solve
finish

/post26
NSOL,2,n0,AZ
abs,3,2
vget,tmparr1(1),3

NSOL,2,n1,VOLT
abs,3,2
vget,tmparr2(1),3

NSOL,2,n1,AZ
```

```
abs,3,2
vget,tmparr3(1),3

*VWRITE,f,tmparr1(1),tmparr2(1),tmparr3(1)
(E25.15,' ',E25.15,' ',E25.15,' ',E25.15,' ')
finish

*ENDDO

*CFCLOS

finish
```

LIST OF PHYSICAL CONSTANTS AND SYMBOLS

Symbol	Description	Units
h	Plank's constant	6.626×10^{-34} Js
k_B	Boltzmann's constant	1.380×10^{-23} VAs/K
μ_0	Magnetic permeability of free space	$4л \times 10^{-7}$ Vs/Am
μ_r	Relative, material magnetic permeability	≥1
ε_0	Dielectric permeability of free space	8.854×10^{-12} As/Vm
ε_r	Relative, material dielectric permeability	≥1
c	Speed of light in free space	2.998×10^{8} m/s
μ_i^m	Magnetic dipole moment with particle index i	Am^2
γ	Gyromagnetic ratio	MHz/T=As/Kg
f, υ	Frequency	1/s
ω	Angular momentum	1/s
ω_0	Spin precession frequency, Larmor frequency	1/s
λ	Wavelength	1/m
N_α, N_β	Low and high energy population spin densities	1
ζ	Induced voltage	$V = kg\ m^2/\ As^3$
χ_v	Magnetic susceptibility	< 0 or ≥0
δ	Skin depth	m
ρ	free electric charge density	C/cm^3
J	Angular momentum	$Kg\ m^2/s$
T	Torque	$Kg\ m^2/s^2$
H	Magnetic field	A/m
B	Magnetic flux density	$T= Vs/m^2=kg/\ As^2$
M	Net magnetization	Am^2
E	Energy	$J=V\ A\ s= kgm^2/s^2$
T	Temperature	K
T_1	Longitudinal relaxation time	s
T_2	Transverse relaxation time	s
R	Resistance	$\Omega = kgm^2/A^2s^3$
L	Inductance	$H=Vs/A=kgm^2/A^2s^2$
C	Capacitnace	$F=As/\ V=A^2s^4/kgm^2$
Q	Quality factor	
t	Time	s
i	Current	A
D	Electric displacement	C/m^2
σ	Standard deviation	

Statement of authorship

I hereby certify that this master thesis has been composed by myself, and describes my own work, unless otherwise acknowledged in the text.

All references and verbatim extracts have been quoted, and all sources of information have been specifically acknowledged. It has not been accepted in any previous application for a degree.

Erklärung

Hiermit erkläre ich, dass ich die vorliegende Arbeit selbstständig und ohne Benutzung anderer als der angegebenen Hilfsmittel angefertigt habe und Stellen, die wörtlich oder sinngemäß aus veröffentlichten Schriften entnommen wurden, als solche kenntlich gemacht habe. Desweiteren erkläre ich, dass diese Arbeit nicht, auch nur auszugsweise, für eine andere Prüfung verwendet wurde.

Rostock, _____

Signature